Universidad Autónoma de Madrid

Facultad de Ciencias

Departamento de Física de la Materia Condensada

Magnetization Dynamics in Magnetic and Superconducting Nanostructures

Juan Francisco Sierra García

Submitted in Partial Fulfillment of the Requirements
for the Degree of Doctor of Physics Science
in the Department of Condensed Matter Physics
in the Autonomous University of Madrid.

Directed by Farkhad Aliev Kazanski

September 2008

Contents

Acknowledgements (Agradecimientos)

Quisiera empezar estas líneas con un agradecimeinto a quien más debo de todos, a mi director de tesis Farkhad Aliev. En primer lugar por confiar en mí, en segundo porque con su exigencia a la hora de hacer física me ha echo madurar enormemente como persona y como profesional. He comprendido con el paso del tiempo que en la física experimental se necesita mucho sacrificio. Farkhad ha sido quien me ha enseñado a manejarme en un laboratorio, pues venía de hacer física teórica. Empecé con soldaduras de cables (mal hechas) y he terminado con conectores de radiofrecuencia. Gracias Farkhad por tu profesionalidad y tu dedicación.

Agradezco profundamente la ayuda de toda la gente del grupo Magnetrans. A Volodya Pryadun, por su ayuda, ingenio y paciencia a la hora de desarrollar el sistema de medida de bajas temperaturas y por haberme enseñado todo lo que conozco sobre programación en LabVIEW. Con él empecé a automatizar todos mis experimentos. A David Herranz, por su ayuda y su sacrificio cuando le pedía que le echara un ojo a alguna medida. A Ahmad Awad por haberme apoyado en todo, en lo personal y lo profesional, yo he intentado enseñarle lo que se sobre radiofrecuencia, él me ha enseñado mucho más que un poco de árabe, han sido muchas las horas juntos en el laboratorio.

A Rubén Guerrero no se ni que decirle, con él he pasado la mayor parte del tiempo en el laboratorio, con él he compartido muchos de mis "bajones" durante la tesis...siempre recibiendo de él una palabra de aliento. Simplemente diría que es el compañero de laboratorio ideal. Ha sido mucho lo que hemos aprendido juntos, pero más lo que él me ha enseñado. Gracias Rubén por todo tu apoyo tanto profesional como humano.

Resalto a los profesores Arkady Levanyuk. En mis once años de mundo universitario, personalemente no he conocido un físico teórico como él. Gracias por sus críticas constructivas durante los seminarios (informales) del grupo y sus multiples ayudas a resolver dudas teóricas. A Raúl Villar, ya no solo por sus críticas sino por haberse leído cuidadosamente la tesis, haberme resuelto muchas cuestiones y por haberse mostrado siempre interesado y preocupado por mí.

Agradezco al Departamento de Física de la Materia Condensada de la Univer-

sidad Autónoma de Madrid su hospitalidad durante estos cinco años. En especial al Laboratorio de Bajas Temperaturas, dirigido por el profesor Sebastian Vieira y a todos los profesores que en él me he encontardo; Jose Gabriel Rodrigo, Herman Suderow, Nicolas Agraït, Marisela Velez, Miguel Angel Ramos y Gabino Rubio. A todos los técnicos del laboratorio, que tanto trabajo les he dado (se han ganado bien el pan), Rosa, Santiago, José, José Luis, y muy especialmente a Andrés Buendía, al cual se deben muchas de las fotografías ilustradas en el texto de la tesis. También a Elsa, nuestra secretaria, con una paciencia a prueba de balas. Incluyo en este punto al SEGAINVEX (Servicios Generales de Apoyo a la Investigación Experimental) y su director Manuel Pazos y a sus diferentes técnicos y responsables**:** Manolo (Helio), Ramón director de la sección de electrónica y sus ténicos Mariano y Jesús y finalmente a Manuel (Mecánica).

Siguiendo por cercanía geográfica a la investigadora Mar García (Centro Superior de Investigaciones Científicas,Madrid) le agradezco las curvas de imanación tomadas con SQUID y su enorme paciencia a la hora de repetir alguna medida.

A Javier Palomares, Manuel Vázques y Oksana Fesenko (Centro Superior de Investigaciones Científicas, Madrid) por sus aclaraciones y sugerencias.

I thank Etienne Snoeck (CEMES-Tulousse, France) the transmission electron microscope images.

I also thank Dr. Dusan Gulobovic and professors Victor Moshchalkov (Katholieke Universiteit Leuven, Belgium) and José Luis Vicent (Universidad Complutense de Madrid, Spain) for the growth of superconducting films, as well as professors Vitali Metlushko (University of Illinois at Chicago, USA) and Jagadeesh Moodera (Massachusetts Institute of Technology,USA) the growth of magnetic thin films.

I am also very thankful to Gleb Kakazei (Universidade do Porto, Portugal) who provided us with Py magnetic dot samples for help with theoretical calculations and experimental measurements that supported our experimental results and for discussions. I would also thank Professor Konstantin Guslienko (Seoul National University, South Korea) for his advices and helpfull suggestions.

I am very grateful to Stephen Russek, who kindly let me to visit his Experimental Group at the National Institute of Standards and Technology, in Boulder, Colorado (USA), during the summers of 2006 and 2007. In Boulder I had the pleasure and the luck of doing research with such a prestigious group, in international research environment and with sympathetic people: Roan Goldfarb (head of the group), Bill Rippard, Matt Pufall, Tom Silva, Thony Koss, Ranko Heindl, Mark Hoeffer, Justin Shaw and Mike Schneider. I am also deeply grateful to Ruth Corwin, the secretary of the group.

Agradezco el apoyo económico brindado por el Ministerio de Educaión y Ciencia con la concesión de la beca de formación de personal investigador FPI- BES-2004-5594 y las ayudas económicas concedidas para realizar las estancias breves en el extranjero.

A todos mis compañeros y buenos amigos del módulo C-III, Eduardo, Óscar (Sisoma), Guillermo (I El Brutal), Juanjo (Califa de Diapasón), Andrés (LaGioconda de Perfil), Carlos, Curro, Bisher, Vanessa, Isabel, Roel y Teresa. Por los buenos vinos y cervezas que hemos compartido, por los múltiples comentarios del amor compartido al arte de la pintura....y por ser siempre los que habéis escuchado mis batallas....gracias.

A mis compañeros de carrera, Abelardo, César, Rocío, Lucas, Javier, Roberto, Martín y Fernándo, por haber compartido no sólo apuntes, sino nuestra vida durante ya más de diez años.

A mis amigos de toda la vida, Mario, Jesús, Emilio y José Antonio.

Y a un nivel más familiar estoy muy agradecido a la Ultreya de Coslada, en especial a Nuria Bofill y Manuel Ortega, por la revisión de la tesis en inglés. A Juanjo (mi futuro cuñado), Hector (Djokovic) y Luis por haber compartido tanto juntos...y compartir lo más importante en nuestra vida (RdG).

A mis buenos amigos Jose Ramón, Ricardo, Carlos, y toda la Zarza Ardiente a quien tanto quiero y debo.

A mis abuelos Pedro y Carmen (cuantas cosas vividas a vuestro lado), a mi abuela Ramona (siempre preocupada por mí) y a mi abuelo Juan, que aunque ya no está presente entre nosotros siempre se ha sentido orgullosos de su nieto. A mis tíos, Angel, Felisa, Jose María y Encarna (esta última casi una mama para mí). A mis primos Angel y Laura que tanto quiero.

A mi familia más cercana, que es a la que más debo. A mis padres Vicente y Maria del Carmen, por vuestra compresión y apoyo en TODO, por haberme soportado mi mal carácter en algunas ocasiones, mis enfados,...papa, mama...aquí no entra todo...GRACIAS. A mis hermanas Almudena y Maria del Carmen: sois las mejores hermanas que uno podría imaginar, gracias por vuestra ayuda siempre que os la he pedido, y por la que sin pedírosola me habéis dado.

Y para terminar a mi esposa Petronela. Sin ella no hubiera sido posible la tesis, ha sido la mayor bendición que he recibido en mi vida. Petri gracias por todo tu apoyo en esta tesis y por haberme soportado. Por las muchas tardes que te quedabas en casa, aburriéndote como una ostra, por estar a mi lado, por haberme mimado y siempre haberme puesto tu hombro para poder llorar....gracias por tu amor.

Introduccion general

Los avances en nanotecnología durante las últimas décadas, entre los cuales se encuentran el crecimiento de películas ultra-delgadas (unas pocas monocapas) y estructuras multicapa así como su nanoestructuración lateral usando técnicas de litografía óptica y electrónica, y más recientemente estructuras auto-organizadas, han llevado a un enorme progreso en el conociemiento de las propiedades estáticas en este tipo de nuevos dispositivos. Entre los ejemplos se incluyen el descubrimiento de la Magnetoresistencia Gigante (GMR, del inglés Giant Magnetoresistance), el cual ha sido considerado como la primera implementación real de la nanotecnología y ha sido galardonada con el premio Nobel de Física en el año 2007, y un efecto relacionado, la Magnetoresistencia Túnel (TMR, del inglés Tunnel Magnetoresistance), recientemente incorporado en la industria de cebezas lectoras de última generación.

Otra de las direcciones en la investigación esta puesta en la creación de medios magnéticos con ciertos patrones o motivos laterales usando técnicas de litografía de alta resolución, lo cual permite explorar nuevos tipos de dispositivos de almacenamiento magnético como son por ejemplo los nanopuntos magnéticos y películas delgadas superconductoras con y sin efectos de anclaje de vórtices superconductores.

Hasta el momento, el principal conocimiento en estas nanoestructuras ha estado relacionado con sus propiedades estáticas, como curvas de imanación, estructura de dominios magnéticos, formación de vórtices, anclaje de vórtices, etc, pero no es mucho lo que se conoce sobre sus propiedades dinámicas.

Esta tesis está dedicada a la investigación de la dinámica de la imanación en dos tipos de nanoestructuras:

- nanoestructuras magnéticas con y sin nanoestructuración lateral y
- peliculas delgadas superconductoras con y sin nanoestructuración lateral.

El principal objetivo de esta tesis es investigar y comprender el comportamiento dinámico de la imanación en nanoestructuras magnéticas y superconductoras, lo cual es importante desde el punto de vista teórico, y muy crucial para posibles aplicaciones tecnológicas.

En el primer tipo de nanoestructuras, entre las que se incluyen uniones túnel magéticas y nanopuntos magnéticos, principalmente usamos un nuevo tipo de magnetómetro basado en la excitacion y detección de la respuesta dinamica magnetica usando un analizador de redes vectorial.

En el segundo tipo de nanoestructuras, se han usado medidas de transporte electrónico con la corrierte alterna para estudiar la dinámica de los vórtices superconductores en películas superconductoras nanoestructuradas y sin una aparente (creada a propósito) nanoestructuración o asimetria.

Una de las ideas principales de esta tesis que une el estudio de properdades dinamicas de las nanoestructuras superconductoras y magnéticas es que, en ambas estamos especialmente interesados en el estudio de la dinámica de la imanación en la presencia de anomalías topológicas de tipo magnético (vórtices).

La tesis esta organizada de la siguiente forma:

El **Capitulo 1** presenta un marco teórico básico sobre las propiedades estáticas y dinámicas de la imanación en sistemas magnéticos y superconductores.

El **Capitulo 2** describe las principales técnicas experimentales de detección de la dinámica de imanación en sistemas magnéticos. Se presenta también el sistema experimantal desarrollado durante la elaboración de esta tesis, el cual nos permite investigar propiedades dinámicas en un amplio rango de frecuencias (de kHz hasta GHz) y de temperaturas (de temperatura ambiente hasta 2 K). Por último, el capitulo presenta el método experimental desarrollado para la detección de la dinámica de vórtices en películas superconductoras.

El **Capitulo 3** muestra los resultados experimatales de la dinámica a alta frecuencia (hasta 147 MHz) de vórtices superconductores en peliculas delgadas superconductoras con una geometría restringida, como son peliculas superconductoras con y sin nanoestructuración. Los estudios consisten en la detección de la señal de voltaje continuo (DC) generado por la dinámica de los vórtices cuando se hace pasar una corriente alterna (AC) a lo largo de la película en presencia de un campo magnético perpendicular a la superfice de la muestra. Hemos observado el efecto de rectificación a alta frecuencia inducido por la barrera de superficie.

El **Capítulo 4** presenta el estudio a temperatura ambiente de la dinámica de la imanación en redes rectangulares de puntos magnéticos de Permalloy ($Fe_{20}Ni_{80}$), donde se varía la distancia entre puntos. Estos puntos magnéticos muestran un estado de vórtice magnético en estado remanente. El estudio incluye la dinámica de la imanación en ambos estados; estado vórtice y estado saturado. Por otro lado, se presenta un estudio de posibles acoplos dipolares, los cuales pueden aparacer cuando la distancia entre puntos se reduce, y la posible anisotropía magnética presente en estos sistemas. Se ha investigado la dependencia de los modos azimutales en el estado vórtice en función de la orientación en el plano del campo magnético de excitación y la respuesta dinámica durante la transición entre el estado vórtice y el estado de vórtice meta-estable.

Finalmente, el **Capitulo 5** describe la dinamica de la imanación en un amplio rango de frecuencias (hasta 20 GHz) en películas delgadas de Permalloy incorporadas como electrodo magnético en uniones tunel magnéticas. El estudio incluye la

dependencia de la dinámica con condiciones de recocido, procesos de oxidación y con la temperatura. Se ha observado una variación anómala de la resonancia ferromagnética in las películas de Permalloy en y fuera de uniones túnel magnéticas. Esta variación en la respuesta dinámica puede estar relacionado con una transición en la orientacion de la imanación en las capas de Permalloy.

General introduction

The advances in nanotechnology during the last decades, which include both, the growth of ultra thin films (few monolayers) and multilayer structures as well as their lateral nanostructuring using optical and electronic lithography techniques, and very recently self-organised structures, have lead in enormous progress in understanding of the static properties of these new devices. The examples include the discovery of the Giant Magnetoresistance (GMR) effect, which is being considered as the first real implementation of the nanotechnology in the industry and has been awarded with the Physic Nobel Prize in 2007, and a related novel effect, the tunneling magnetoresistance (TMR), recently incorporated into read-heads technology of the last generation of hard disk drives.

Creation of laterally patterned magnetic media using high resolution lithography techniques and study of its dynamic response is another research direction pushed forward recently. It permits to explore dynamics not only in novel types of magnetic storage devices such as magnetic nanodots but also in superconducting thin films without or with nanostructuring leading to superconducting vortex matching effects.

Up to now, the main knowledge about these new nanostructures has been related to their static properties, such as magnetization curves, domain wall structure, vortex formation, vortex matching, etc., and little is known on their dynamic properties.

This thesis is devoted to investigate the magnetization dynamics in two types of nanostructures:

- magnetic nanostructures with and without lateral nanostructuring and
- superconducting thin films with and without lateral nanostructuring.

The main objective of this thesis is to investigate and to understand further magnetization dynamics in superconducting and magnetic nanostructures, which is important from the fundamental point of view and is crucial for their technological applications.

To get inside the magnetization dynamics in the first type of nanostructures, which include magnetic tunnel junctions and arrays of magnetic dots, we mainly used a newly created broadband magnetometer based on vector network analyzer detection.

In the second type of nanostructures, we mainly used electron transport mea-

surements to investigate the superconducting vortex dynamics in plain and nanostructured thin films.

One of the main ideas which unites investigation of superconducting and magnetic nanostructures is that in both systems we are interested in magnetization dynamics in the presence of topological magnetic anomalies (vortices).

The thesis is organized as follows:

Chapter 1 presents a theoretical background of the static and dynamics properties of magnetic and superconducting nanostructures .

Chapter 2 describes the main experimental methods used to investigate the magnetization dynamics in magnetic nanostructures. We also describe the new experimental set-up developed during this thesis which permits to investigate magnetization dynamics in a high frequency (from kHz to GHz) and temperature (from room temperature to 2 K) range. Finally, the chapter presents the experimental method developed for investigate superconducting vortex dynamics through current rectification in superconducting thin films.

Chapter 3 presents the high frequency dynamics (up to 147 MHz) of the superconducting vortices in restricted geometries, such as plain and nanostructured superconducting films studied via DC response voltage generated by an in-plane AC current in presence of a magnetic field perpendicular to the film plane. We have observed novel surface barrier induced high frequency rectification effect.

Chapter 4 presents room temperature studies of the magnetization dynamics in arrays of Permalloy ($Fe_{20}Ni_{80}$) magnetic dots, with varying center-to-center distance. These magnetic dots present a magnetic vortex state in the remanent state. The investigation includes both, the magnetically saturated state and the non-uniform state, where a magnetic vortex structure is formed in the dots. We have investigated the magnetic field dependence of azimuthal modes in the vortex state as a function of the orientation of the in-plane pumping field and the dynamic response during the transition between stable and metastable vortex states.

Finally, **Chapter 5** presents the magnetization dynamics in a wide range of frequencies (up to 20 GHz) in Permalloy films incorporated such as free magnetic layer in magnetic tunnel junctions, and its dependence on annealing conditions, preoxidation process and sample temperature. We have observed anomalous variation of the ferromagnetic resonance in Permalloy films in and out of magnetic tunnel junction stacks which could be related with a magnetization reorientation transition in Permalloy layers

Chapter 1

Theoretical background

1.1 Introduction

Understanding of magnetization dynamics in magnetic and superconducting nanostructures such as spin valves, magnetic tunnel junctions, superconducting and magnetic thin films and arrays of magnetic dots including those covered by superconducting films have been of special importance during last decades.

As to the magnetic nanostructures, the field got strong momentum in late 1980s when a new research direction in fundamental and applied science -spintronics- appeared. Spintronics exploits the intrinsic spin of electrons and associated magnetic moment in addition to its fundamental electronic charge. The study of the magnetization dynamics in different types of magnetic nanostructures is not only an effective tool to determine their quality but also to answer important question such as how the magnetization responds to an abrupt change of the external magnetic field or applied electric (spin) currents. In this sense, measurements of spin waves in magnetic nanostructures may provide information both on the quality of magnetic devices and on fundamental physical phenomena.

As to the superconducting devices, currently they have important applications as transformers, power storage devices, electric power transmission, electric motors, magnetic levitation devices and Superconducting Quantum Interference Devices (SQUIDs)- magnetometer capable of measure extremely small magnetic fields. However, superconductivity is sensitive to the presence of magnetic fields and currents. Understanding and controlling the vortex motion is of fundamental importance and has important applied aspects because of need to improve applications of superconducting devices in the industry. This chapter introduces reader to magnetization dynamics in magnetic and superconducting nanostructures in the presence of permanent (DC) and time dependent (AC) magnetic fields and electric currents.

1.2 Magnetization dynamics in ferromagnetic systems

If one considers the simple experience of applying an external magnetic field $\mathbf{H}$ in a region where there are present isolated magnetic moments $\mathbf{m}$, one may observe an alignment of $\mathbf{m}$ with $\mathbf{H}$. When one treats a magnetic structure, it is convenient to define the magnetization vector as the total magnetic moment per unit of volume ($\mathbf{M} = \sum(\mathbf{m}_i)/\text{Unit Vol}$). Magnetization dynamics describes the time evolution of the magnetization $\mathbf{M}$ out of equilibrium. The application of the magnetic field $\mathbf{H}$ out of the direction of $\mathbf{M}$ will produce a torque on this $\mathbf{T} = \mu_0(\mathbf{M} \times \mathbf{H})$. This torque is equal to the change of the angular momentum, i.e. $\mathbf{T} = d\mathbf{L}/dt$. Relationship $\mathbf{M} = \gamma\mathbf{L}$ describes the evolution of the magnetization

$$\frac{d\mathbf{M}}{dt} = -\mu_0\gamma\mathbf{M} \times \mathbf{H} \quad , \tag{1.1}$$

where $\gamma = g(e/2m_e)$ is the gyromagnetic ratio which is proportional to the ratio between the charge e ($1,602 \times 10^{-19}\,\text{C}$) and the mass $m_e(9.109 \times 10^{-31}\,\text{kg})$ of the electron. The constant g represents the spectroscopic splitting factor that for a free electron its value is $g = 2 \times 1.001159657$.

Equation 1.1 defines the Larmor precession, with the frequency $\omega_L = \gamma H$ the called Larmor precession frequency. This equation does not take into account any possible damping term in the system. However, in a real ferromagnetic (FM) system the magnetization dynamics may be expected to have a damping term.

1.3 Bulk ferromagnetic systems

1.3.1 Magnetization dynamics equations

Equation 1.1 does not describe a real FM system correctly, it is necessary to define a new term that adds the damping to the system. The first approach in this direction was given by Landau and Lifshitz (LL) [1] with the following expression

$$\frac{d\mathbf{M}}{dt} = -\mu_0\gamma\mathbf{M} \times \mathbf{H}_e - \frac{\mu_0\lambda}{M_s^2}\mathbf{M} \times (\mathbf{M} \times \mathbf{H}_e) \quad , \tag{1.2}$$

where M_s is the saturation magnetization and the constant λ is the LL damping parameter, whose value will give information about the dissipation mechanisms. The LL equation describes the magnetization dynamics in bulk ferromagnets with two terms; the first one describes the precession of the magnetization around the field $\mathbf{H}_e$, the effective magnetic field inside the material that in general will be different from the external magnetic field applied. One can obtain this effective magnetic field such as the negative gradient of the free energy of the system with respect to

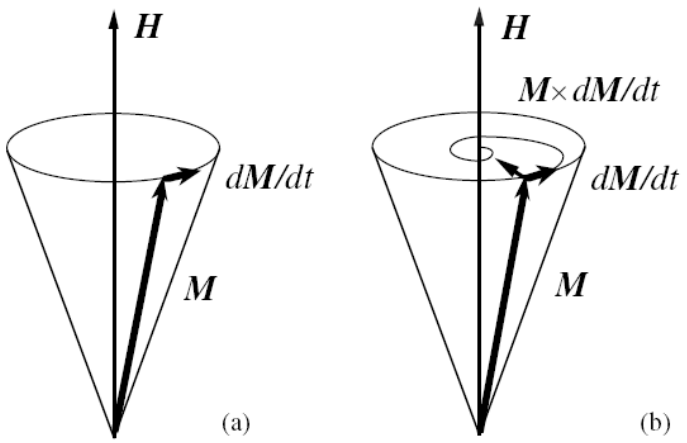

Figure 1.1: Sketch showing the magnetization dynamics in a ferromagnet with (a) and without (b) damping term.

the magnetization $\mathbf{H}_e = -\boldsymbol{\nabla}_M U$. This first term conserves the energy of the system. On the other hand, the second term introduces the energy dissipation or damping and describes the motion of $\mathbf{M}$ towards $\mathbf{H}_e$.

Several alternatives dynamic equations have been proposed by changing the form of the damping term. In this thesis the Landau-Lifshitz-Gilbert (LLG) equation [2] will be used:

$$\frac{d\mathbf{M}}{dt} = -\mu_0\gamma\mathbf{M}\times\mathbf{H}_e + \frac{\alpha}{M_S}\left(\mathbf{M}\times\frac{d\mathbf{M}}{dt}\right) \quad , \tag{1.3}$$

where α is the dimensionless Gilbert damping parameter. This term describes viscous damping in which damping is proportional to the magnetization velocity. Figure 1.1 shows how the magnetization moves without taking into account the Gilbert damping parameter and consider it.

In the limit of $\alpha \ll 1$ both equations, LL and LLG, are identical defining α such as $\alpha = \lambda/\gamma M_S$. In the other extreme, when $\alpha \gg 1$,LL equation predicts the magnetic moments will loose energy quickly and rapidly reach its low energy state, whereas the LLG equation predicts that dissipation of the energy and the approach to the low energy state will become increasingly slow. The observed damping constant in magnetic materials is typically small, in the range between 0.01 and 0.1, therefore one does not need to distinguish between LL and LLG equations.

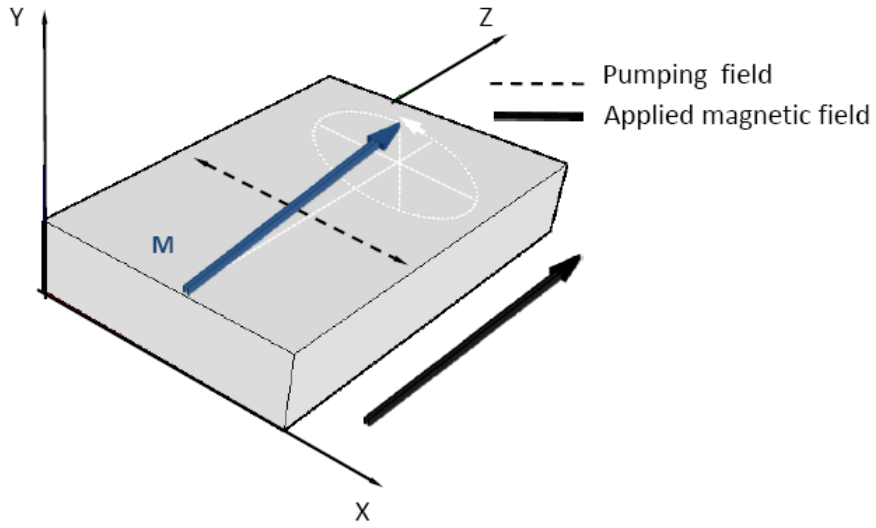

Figure 1.2: Scheme of a typical FMR experiment. An external magnetic field is applied along the magnetization direction of the sample. Simultaneously, the pumping field transverse to the external field produces the precession of the magnetization **M** around its equilibrium position.

1.3.2 Ferromagnetic resonance

Ferromagnetic resonance (FMR) experiment is a typical and easy technique to observe the resonance condition in the magnetization and evaluate the damping parameter. In a typical FMR experiment a sample is placed in an uniform external magnetic field large enough to magnetize it parallel to the field direction. If the magnetization is slightly disturbed from its equilibrium position, for example using a transverse oscillating magnetic field called pumping field, magnetization will precess about the field direction. The scheme of magnetic fields configuration in a FMR experiment is sketched in Fig. 1.2.

The magnetization motion will cause the precession to be damped, or undergo relaxation. Unless the frequency $\omega = 2\pi f$ of the pumping field is nearly equal to the precessional frequency ω_0 of the magnetization, the energy coupled into the precessing magnetization will be small. When $\omega \sim \omega_0$, the coupling is large and the amplitude of precession is limited only by the damping of the system. One needs to obtain the resonance frequency and the linewidth [1] of this resonance. This last parameter is of special interest to obtain the damping value α. Solving the LLG

[1] Defined as the full width at half maximum of the response.

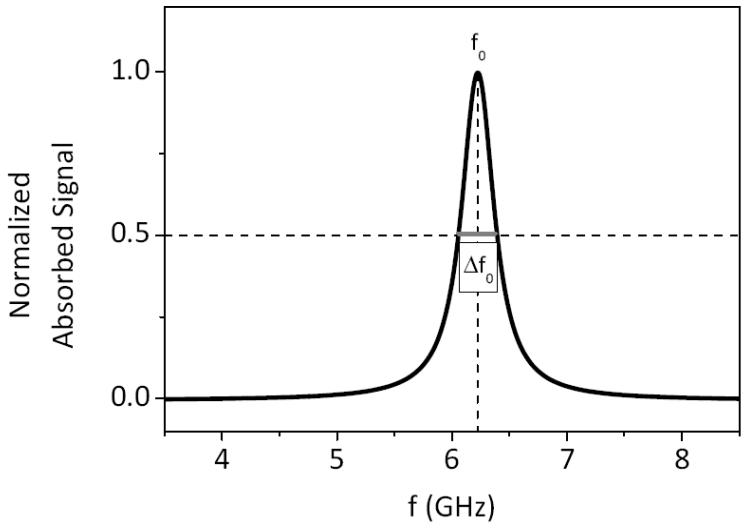

Figure 1.3: Representative ferromagnetic resonance curve and the corresponding resonance frequency (f_0) and linewidth value (Δf_0).

equation (Eq. 1.3) in spherical coordinates [3], the two parameters of the FMR are given by [4] [5];

$$f_0 = \frac{\gamma}{2\pi M s \sin\theta}\sqrt{\left(\frac{\partial^2 U}{\partial\theta^2}\frac{\partial^2 U}{\partial\phi^2} - \frac{\partial^2 U}{\partial\theta\partial\phi}\right)} \tag{1.4}$$

$$\Delta f_0 = \frac{\alpha\gamma}{2\pi M_s}\left(\frac{\partial^2 U}{\partial\theta^2} + \frac{\partial^2 U}{\partial\phi^2}\frac{1}{\sin^2\theta}\right) \tag{1.5}$$

where the two angles θ and ϕ are the polar and the azimuthal angle in spherical coordinates and U is the free energy of the system. Figure 1.3 shows an example of a typical FMR curve and the corresponding f_0 and Δf_0 values.

1.3.3 Magnetic damping

Due to the technological relevance in spintronics, in the past several years there has been a revival of interest in the theory of magnetization damping [6] [7] [8]. The knowledge of the typical magnetization relaxation times is one of the most important parameters of interest for FM systems. Measurements of the resonance linewidth is one of the main techniques used to investigate these phenomena. In a FMR experiment, the linewidth of the resonance ΔH, measured in units of magnetic field, consists of intrinsic and extrinsic contributions. The intrinsic contribution is always present in a particular material and cannot be suppressed. It is present even

in a perfect crystal and originates from interactions of free electrons with phonons and magnons. The extrinsic contributions can vary from one sample to another, depending on preparation. They arise from microstructural imperfections or from finite geometry. They could, in principle, be suppressed.

Intrinsic damping mechanism

The mobile electrons, combined with spin-orbit coupling, are the agents which first transfer energy out of the spin system. Formal treatments [9] [10] agree that spin-orbit coupling enables relaxation in ordinary spin conserved scattering (confined to electronic states within either spin-up ($\uparrow$) and spin-down ($\downarrow$) sub-bands) and in spin-flip scattering (when crossing from one sub-band to the other). Since the 1970s the intrinsic magnetic relaxation in metals has been shown that is caused by incoherent scattering of electron-hole pair excitations [9] by phonons and magnons. The electron-hole interactions involve three particle scattering. The excitations are either accompanied by electron spin-flip or the spin remains unchanged. Spin-flip excitations can be caused by the exchange interaction between magnons and itinerant electrons (s-d exchange interaction), during which the total angular momentum is conserved. The spin conserving scattering is caused by spin-orbit interaction which leads to a dynamic redistribution of electrons in the electron k-momentum space.

Other possible contributions to the intrinsic damping may be caused by eddy currents [11] and by direct magnon-phonon scattering [6]. In a metallic ferromagnetic system any change in the magnetization induces eddy currents which tend to compensate this change, and thus provides a damping mechanism. On the other hand in the magnon-phonon scattering, *Suhl* [6] analyzed the case for samples smaller than a domain wall thickness, in which the coupling to the lattice is by direct relaxation via magnetostriction into a lattice of known elastic constant.

Extrinsic damping mechanism

Surface defects, surface roughness, grain boundaries and atomic disorder are potentially important sources of the two-magnon scattering [12], that is one of the most important sources of relaxation in materials with inhomogeneities. The basic idea is that such inhomogeneties result in a coupling between the otherwise orthogonal uniform precession and degenerate SW modes and that the energy transfer out of the uniform precession to the degenerate modes is important in the initial stages of relaxation. The total number of magnons remains unchanged since one magnon is annihilated and another is created. The interaction is sensitive to the nature of the inhomogenity. As a general rule, the coupling is large for SW wavelengths greater than the dimensions of the inhomogenity. In the idealized FMR experiment, an uniform precession mode is excited whose wave vector $k_{\|}$ parallel to the surface is zero. Arias and Mills reported [13] a detailed theory of the two-magnon processes

in the FMR response of ultra thin films when the magnetization and the applied magnetic field were in-plane. In the presence of dipolar couplings between spins, there will be short wavelength spin waves degenerate with the FMR mode. The SW frequency is given by [13]

$$\omega^2(k_\parallel) = \omega_0^2 - 2\pi\gamma^2 M_S k_\parallel d\left(H - 4\pi M_S \sin 2\phi_{k_\parallel}\right) + \gamma^2(4\pi M_S + H)\mathcal{A}k_\parallel^2 \quad , \qquad (1.6)$$

where ω_0 is the resonance of the uniform mode, d is the film thickness, $\phi_{k_\parallel}$ is the in-plane angle of the magnon wave vector $k_\parallel$, $\mathcal{A}$ is the exchange stiffness and M_S and H are the magnetization of the sample and the applied in-plane magnetic field respectively.

1.4 Ferromagnetic thin films

Magnetization dynamics in magnetic thin films has been intensively studied since the late 1950s when magnetic thin film memories were proposed as a replacement for ferrite core memory. Magnetoelectronic devices which are subject of this thesis are composed of films with thickness below 1 μm. Understanding and controlling the magnetization dynamics in the GHz range has been the target during the last few decades. The importance of these devices is related to the very fast switching time, i.e. the time required for magnetization reversal. Nowadays, the application of thin films such as MRAM and the need to improve and develop faster devices is one of the most important motivation for engineers and physicists of this field. Switching time in these systems is very close to 1 ns as long as the available magnetic field is at most a few Oe [14]. Magnetization reversal by a sequential process of domain wall motion is time consuming, which can be avoided in thin films. The key for the fast switching time requirement is obtained by introducing an internal uniaxial anisotropy by magnetic annealing, i.e. a preference direction for the magnetization inside the film. Under these conditions the film becomes a single domain oriented in the annealing field direction.

1.4.1 Ferromagnetic resonance in thin films

The first observation of FMR in magnetic films was reported by *Griffiths* in 1946 [15]. He noticed that the resonance conditions took place for values of the static external field much lower than the one expected for the usual resonance relation for electrons. This discrepancy was explained assigning large values to the spectroscopic splitting factor g. However, depending on the sample shape and relative orientation between **H** and **M**, the resonant magnetic field changed its values. It was in 1948 when *Kittel* developed the theory of the FMR [16]. He pointed out the importance of

the demagnetizing field to define the resonant condition. Due to the demagnetizing field, the internal magnetic field inside the sample is quite different from the applied external magnetic field.

$$\begin{aligned} H_x^i &= H_x - N_x M_x \ , \\ H_y^i &= H_y - N_y M_y \ , \\ H_z^i &= H_z - N_z M_z \ , \end{aligned} \tag{1.7}$$

here $\mathbf{H}^i$ denotes the internal magnetic field, $\mathbf{H}$ the applied magnetic field and $N = (N_x, N_y, N_z)$ the demagnetizing factor of the sample. In order to obtain the resonance frequency one supposes the applied magnetic field to be along the **z** axis. To first order approximation one has $\frac{dM}{dt} = 0$ and $M_z = M$. Solving the LLG equation (Eq. 1.3), one obtains

$$\begin{aligned} \frac{dM_x}{dt} &= -\gamma\mu_0(M_y H_z^i - M_z H_y^i) = -\gamma\mu_0 M_y \left[H + (N_y - N_z)\, M\right] \ , \\ \frac{dM_y}{dt} &= -\gamma\mu_0(M_z H_x^i - M_x H_z^i) = -\gamma\mu_0 M_x \left[H + (N_x - N_z)\, M\right] \ . \end{aligned} \tag{1.8}$$

The time dependence of the magnetization can be supposed to be proportional to $\exp(-i\omega t)$ with $\omega = 2\pi f$. By introducing this dependence and by solving the system of coupled equations 1.8, one obtains the resonance condition

$$f_0 = \frac{\mu_0\gamma}{2\pi}\sqrt{\left[H + (N_y - N_z)\, M\right]\left[H + (N_x - N_z)\, M\right]} \ . \tag{1.9}$$

In the special case of the applied magnetic field H is in the xz-plane of a thin film (see Fig. 1.2), with $N_x = N_z = 0$ and $N_y = 1$, the resonance frequency of the uniform mode will be

$$f_0 = \frac{\mu_0\gamma}{2\pi}\sqrt{H^2 + HM} \ . \tag{1.10}$$

As we have explained previously, usually an uniaxial anisotropy field H_K is created during the sample growth. By taking into account this anisotropy the resonance frequency in thin films with an uniaxial anisotropy is given by the following expression [16]

$$f_0 = \frac{\mu_0\gamma}{2\pi}\sqrt{(H + H_K)(M_S + H_K + H)} \ . \tag{1.11}$$

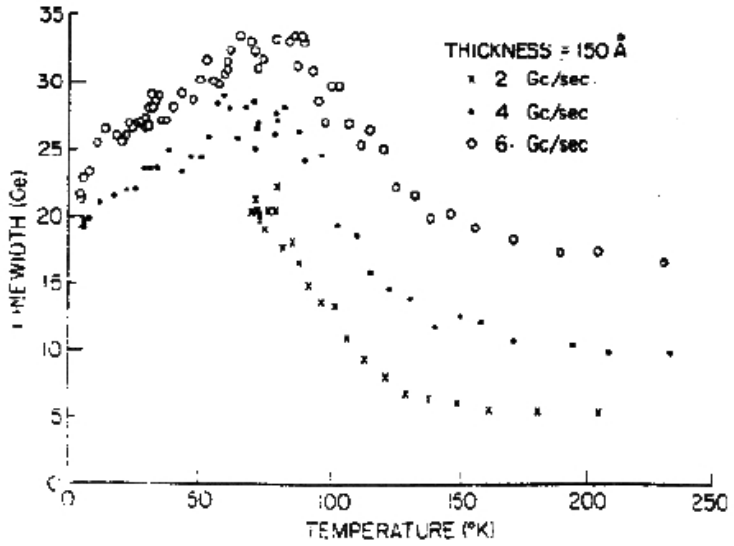

Figure 1.4: Dependence of the FMR linewidth on temperature in 150 Å thick Permalloy film at measured with 2, 4 and 6 Gc/s [GHz]. Picture taken from [19].

1.4.2 Magnetic damping in thin films

Since the 1960s the magnetic losses mechanism in thin films have been intensively studied. In ultra thin magnetic films the FMR linewidth in the microwave range shows the following linear dependence on the excitation frequency [17]

$$\Delta H = \Delta H(0) + 1.16\frac{\omega G}{\gamma^2 M_S} \quad . \tag{1.12}$$

$\Delta H(0)$ is the frequency independent linewidth which comes from the film inhomogeneties and is called the extrinsic damping contribution. The second term, through the intrinsic Gilbert damping parameter $G = \alpha\gamma M_S$ depends on α, is the intrinsic damping contribution. It is seen that the second term varies linearly with frequency of the RF drive. The linewidth dependence on film thickness was studied in [18] demonstrating a linear dependence with thickness.

It is interesting remark the strong dependence of the linewidth on temperature reported by *Patton* et al. [19]. Figure 1.4 shows the experimental data. The linewidth exhibits a clear maximum at low temperatures (<100K). This observation is relevant for effects will be focusing in more details in the Chapter 5 where the FMR dependence on temperature in different MTJs containing Permalloy ($Fe_{20}Ni_{80}$) layers as well as free Permalloy magnetic layer will be investigated.

1.5 Magnetic nanostructures

Magnetic nanostructures that are being used in the market are rather complex multilayer pillars composed of different thin films. These devices should posses some important characteristics such as sensitivity to magnetic fields, ability to fast and precise control the magnetic state of the nanostructure and low noise response

The first magnetic nanostructures were developed in the 1970s. They included bubble memory and bubble logic based on perpendicular domains in yttrium iron garnet films [20][21]. However, these structures were unable to compete with other memories, such as semiconductor and hard disk memories. It was in the 1980s when magnetic devices based on the anisotropic magnetoresistance effect were proposed for read head sensors and MRAM. With the discovery of the giant magnetoresistance effect (GMR) in magnetic multilayers (MMLs) and the tunnel magnetoresistance (TMR) in magnetic tunnel junctions (MTJs) the sophistication and usefulness of these magnetic devices have advanced very rapidly.

The magnetic nanostructures that are being developed by the industry consist of structures with two or three magnetic layers such as MMLs, spin valves (SVs) and MTJs.

MMLs consist of magnetic layers antiferromagnetically exchange coupled across the non-magnetic layers. on the other hand, SVs and MTJs, shown in Fig. 1.5, include two ferromagnetic (FM) layers sandwiching a thin non-magnetic metal (SVs) or an insulating barrier (MTJs). Normally in these structures one of the FM layers is free to rotate in the presence of an applied magnetic field while the other one is pinned, i.e. the magnetization in that layer is relatively insensitive to moderate magnetic fields.

1.5.1 GMR and TMR

MMLs, SVs and MTJs are devices which share the same basic principles of operation: the resistance of the structure is a function of the relative orientation between the magnetization of the adjacent layers. The different resistance state can be used as data storage bits, which may be written by using an applied magnetic field produced by an adjacent current carrying line.

The GMR effect was discovered in 1988 by *Fert* [22] and *Grünberg* [23] independently in antiferromagnetically coupled Fe/Cr/Fe trilayers. This discover can be considered the birth of spintronics and have been awarded with the Nobel Prize in Physics in 2007.

The GMR effect is generally attributed to spin dependent scattering in successive FM layers. In classical experiments, the antiferromagnetic (AF) alignment of the FM layers is provided by exchange coupling of AF interlayers placed between the FM layers. The magnetic state is changed into a FM alignment by applying an magnetic field. The resistance R of the device will be reduced dramatically when

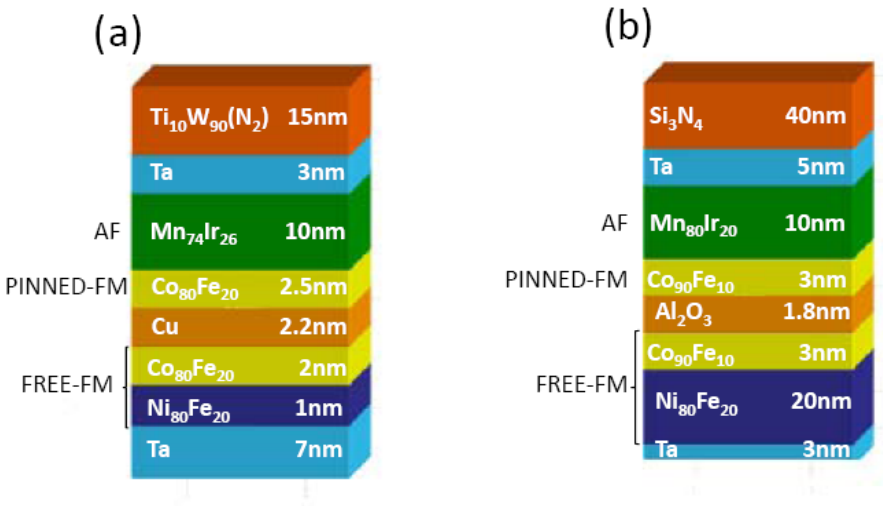

Figure 1.5: (a) Sketch showing the scheme of a spin valve with CoFe ferromagnetic (FM) layers sandwiching a Cu metallic layer. (b) Magnetic tunnel junction with a Al_2O_3 insulating barrier. In both nanostructures the PINNED-FM layer is exchange biased by an antiferromagnetic (AF) layer.

the applied magnetic field aligns the magnetization of the different layers in the same direction. The definition of the GMR is given by the expression

$$GMR = \frac{R_{\uparrow\downarrow} - R_{\uparrow\uparrow}}{R_{\uparrow\uparrow}} \quad , \tag{1.13}$$

where $R_{\uparrow\uparrow}$ and $R_{\uparrow\downarrow}$ denotes the resistance for FM and AF alignment respectively.

The TMR effect at room temperature was first discovered independently by two groups [24] [25]. In the spin-dependent tunneling effect, electrons tunnel across an insulating barrier between two FM electrodes and the resistance depends on the relative orientation of the two magnetic layers. The tunnelling can be either incoherent (across amorphous barriers) or coherent (across crystalline barriers). For incoherent scattering, first explained by the Jullière model [26], the TMR of such a junction is proportional to the product of both electrodes polarization $\mathcal{P}_1$ and $\mathcal{P}_2$

$$TMR = \frac{2\mathcal{P}_1\mathcal{P}_2}{1 - \mathcal{P}_1\mathcal{P}_2} \quad , \tag{1.14}$$

with

$$\mathcal{P}_i = \frac{\mathcal{D}_{i\uparrow}(\varepsilon_F) - \mathcal{D}_{i\downarrow}(\varepsilon_F)}{\mathcal{D}_{i\uparrow}(\varepsilon_F) + \mathcal{D}_{i\downarrow}(\varepsilon_F)} \quad , \tag{1.15}$$

being $\mathcal{D}_i(\varepsilon_F)$ the interfacial density of states at the Fermi level for spin-up ($\uparrow$) and spin-down ($\downarrow$) bands respectively. Both equations lead to a low-resistance state when the two FM layers have their magnetizations aligned parallel to each other, and a high-resistance state when the magnetizations are antiparallel. The effective spin polarization of the FM layers involved in the tunnelling process depends both on the type of ferromagnetic layers and on the type and quality of the insulating barrier.

Figure 1.6 shows the original curves reported for the GMR effect (a) and for the TMR effect (b).

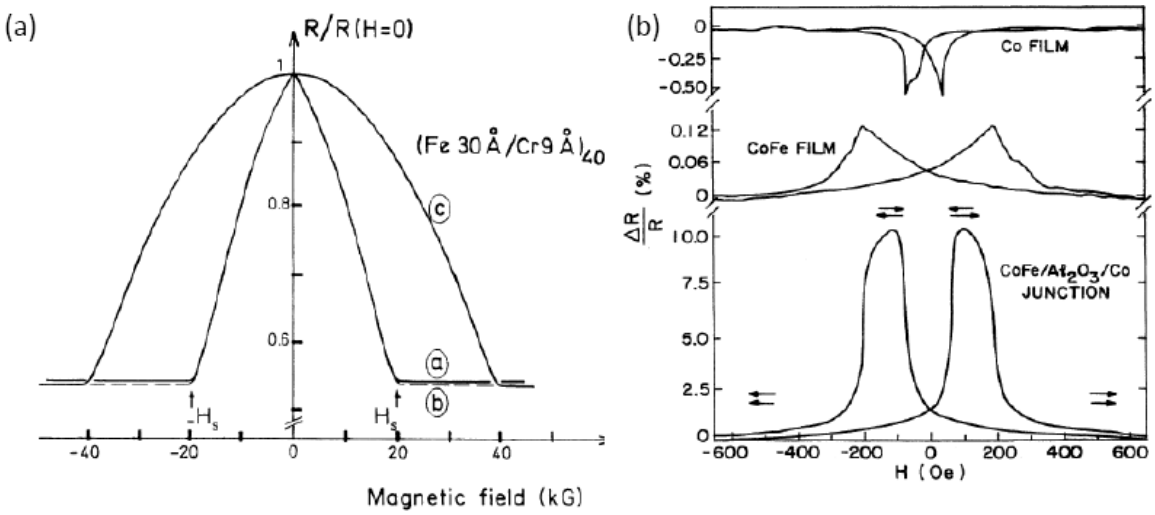

Figure 1.6: (a) The GMR curve measured in $[Fe(30\,\text{Å})/Cr(9\,\text{Å})]_{40}$ at $T = 4.2\,\text{K}$ (taken from [22]). The current is applied along the [100] direction. The curve-a is obtained when the current and the magnetic field are parallel. The curve-b when the magnetic field is in the layer plane perpendicular to the current and the curve-c when the magnetic field is applied perpendicular to the layer plane. (b) Room temperature resistance of a Co film, CeFe film and a magnetic tunnel junction with CoFe and Co magnetic layers sandwiching by an amorphous insulating barrier (Al_2O_3) (taken from [24]). The magnetic field is applied along the layer plane. The arrows indicate the orientation of magnetization in both magnetic layers.

1.5.2 Magnetization dynamics in magnetic nanostructures

One of the goals of this thesis is the investigation of the magnetization dynamics in coupled thin FM structures, such as MTJs with one of the FM layers free to move in presence of moderate magnetic fields. The dynamic response of the free FM layer will responds to the LLG equation (Eq. 1.3) with different contributions

to the effective magnetic field $\mathbf{H}_e$. The following paragraphs discuss different types of magnetic interactions that can be present in these systems.

Direct coupling between magnetic layers

The simplest case of magnetic double layer is the surface itself of a bulk ferromagnet. At the surface, magnetic constants like magnetization M and crystalline anisotropy K could be different from those inside the bulk of the FM material. The change of magnetic interaction and magnetic anisotropy at the surface may lead to rather dramatic phenomena. If K favors a different direction of the magnetization than in the bulk material, special magnetic structures may be induced at the surface even when the bulk of the specimen is in a single magnetic domain state.

In the case of two FM layers in close contact, the magnetostatic interactions between these layers may be approximated by two contributions as Fig. 1.7 shows. The first contribution (dot lines) is the magnetostatic field, generated by the divergence of the magnetization at the edge of the layers. Its presence leads to an interaction term which favors antiparallel alignment of the FM layers. The second contribution (dashed lines) describes the magnetostatic coupling due to effective charges generated by the roughness of each magnetic layer and is usually referred to as “Néel" or "orange peel" coupling. This coupling can be approximated as

$$E_{co;12} = -E_{co}\mathbf{M}_1 \cdot \mathbf{M}_2 \quad , \tag{1.16}$$

where $\mathbf{M}_1$ and $\mathbf{M}_2$ are the magnetization of the first and second FM layer respectively. E_{co} is the phenomenological coupling energy and $\mu_0 H_{co} = E_{co}/M_S$ is the phenomenological coupling field that, in general, is positive an favors parallel alignment of the FM layers. This term. Capability to reduce this kind of coupling is very important in order to grow high quality stacks reducing the extrinsic contribution to the damping.

A detailed investigation of the magnetization dynamics and static magnetization in MTJs, such as using the FMR and its linewidth may be a powerful tool to determine the possible influence of "orange peel" coupling and will be considered in the Chapter 5 of this thesis.

Exchange bias

Exchange bias (EB) may arise if a thin film of ferromagnet has a common interface with a natural or synthetic antiferromagnet. This phenomenon was discovered by *Meiklejohn and Bean* in 1956 [27] who studied hysteresis loops in a sample of Co in contact with CoO and observed that the center of the magnetization loops was shifted from zero field. They attributed the shift to a bias field originating from the antiferromagnetic CoO film. The shift in the hysteresis loop can be very useful to control the magnetization of the devices used in applications. The magnetic disk

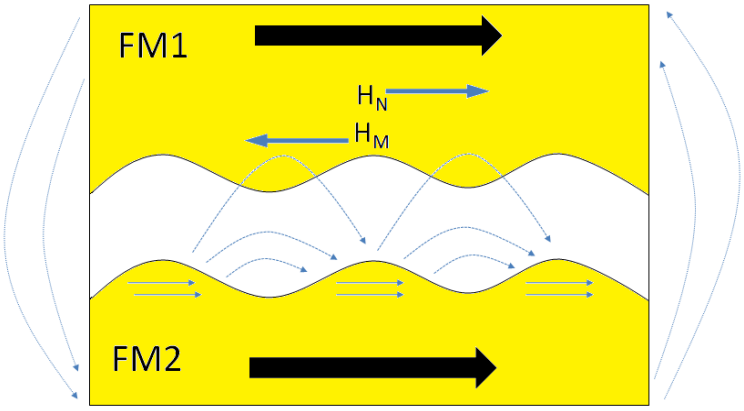

Figure 1.7: Sketch showing two interlayer coupling mechanisms. Dot lines represent the magnetostatic field H_M that favors an antiparallel alignment of the two ferromagnetic layers. Dashed lines shows the Néel or orange peel coupling that favors a parallel alignment.

storage industry has already implemented exchange bias phenomena in the read head technology. During the last decade the magnetization dynamics of EB systems such as NiO/FeNi has been deeply investigated [28] [29] [30] [31] [32] [33]. The FMR studies are currently a very powerful tool to investigate reversible and irreversible behavior of the AF layer. Determining the exchange bias field and the linewidth of the resonance is a direct measure of the relaxation rate of the uniform precession and an indirect measure of the structure of the EB films. Studies of FM layer linewidth with temperature usually show a pronounced maximum at temperatures well bellow the Néel temperature of the AF layer [34]. The strong temperature dependence of the isotropic shift and FMR linewidth observed reflects the presence of different spin pinning subsystems and of different time scales of the FMR in these systems.

Exchange coupling

The exchange coupling is a quantum-mechanical interaction which may appear when one considers magnetic interactions between two closely situated magnetic layers separated by a non-magnetic metallic (NM) layer [35]. Depending on the interlayer thickness, the exchange coupling can result in parallel or antiparallel alignment in magnetic layers [36]. This kind of coupling may be associated with indirect exchange interaction mediated by the conduction electrons of the metallic spacer layer. It is directly related with the Ruderman, Kittel, Kasuya, Yoshida interaction (RKKY). A phenomenological description of the exchange coupling proposed to explain the observed experimental results gives the interlayer exchange coupling energy E per

unit of area as

$$E = -J_1 \cos\phi - J_2 \cos^2\phi \quad , \tag{1.17}$$

where ϕ is the angle between the magnetizations of the two FM layers. The first term in the equation is called the bilinear coupling and the second the biquadratic coupling. Coefficients J_1 and J_2 describe the type and the strength of the coupling. When the bilinear term dominates, the energy minimum corresponds to FM coupling for $J_1 > 0$ and AF coupling for $J_1 < 0$. On the other hand, when biquadratic coupling is the main term and is negative, one gets a 90^o coupling. As it has been mentioned above, the microscopic mechanism which explains the bilinear exchange coupling J_1 has the same physical origin as the RKKY interaction. As to the biquadratic coupling, J_2 could in principle be also intrinsic, but the experimental results could be also understood in terms of an extrinsic effect due to the roughness of the interlayer [37].

1.6 Magnetic nanodots

Another research line in this thesis is related to investigation of the magnetization dynamics in magnetic dots arrays in form of disks with and without magnetic vortex structures inside of them.

The magnetism at small scale length provided a wealth of scientific interest and potential technological approach. Recent developments in nanotechnology and electron beam lithography techniques with ability to create magnetic dots of well defined forms, have strongly enhanced interest to these systems both from fundamental points of view and because of potential applications such as in magnetic recording media and spintronics. It is therefore very important to control the formation of the so-called magnetic vortices and their dynamics in such circular magnetic nanostructures. When arrays of nanodots are formed, a spatial regularity in dots geometry and interdot distance permits observation of well defined modes of both individual and collective excitations. In this section vortex state formation in the insulated magnetic disks will be first described. Secondly, we shall discuss possible high frequency magnetic excitations in these magnetic nanostructures.

1.6.1 Magnetic vortex formation

The FM materials generally form domain structures to reduce their magnetostatic energy. However, if the dimensions of the FM material are reduced to micrometer or nanometer length scale, the formation of domains is not energetically favored anymore. depending of shape of the device, exotic magnetic topological anomalies, such as a curling spin configuration with internal magnetization vortex structure

may appear [38]. When the dot thickness is much smaller than the dot radius all the spins tend to align in the dot plane. The spin configuration curls around the center of the dot with the orientation in the surface plane while in the center of the vortex core the magnetization is perpendicular to the plane. Figure 1.8 shows the corresponding spin configuration.

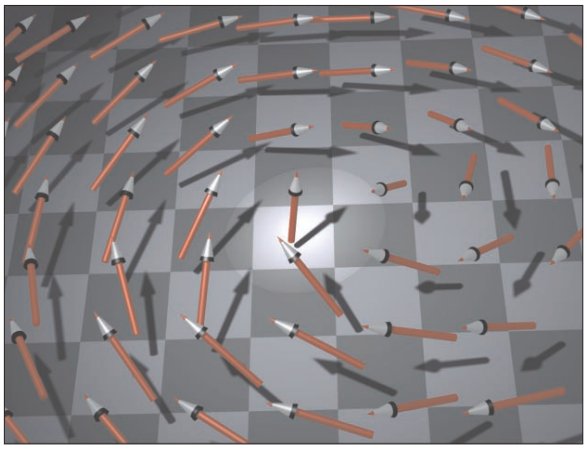

Figure 1.8: The spin configuration in a circular nanodot. Far away from the vortex core the magnetization continuously curls around the center with the orientation in the surface plane. In the center of the vortex core the magnetization is perpendicular to the plane (picture taken from [39])

In the absence of external magnetic field, three parameters define the magnetic structure of a dot: the dot radius R, the dot thickness L and the exchange length, defined as $L_{ex} = \sqrt{2\mathcal{A}/M_S^2}$, where $\mathcal{A}$ is the exchange stiffness and M_S the saturation magnetization. A magnetically soft particle with lateral dimensions smaller than L_{ex} ($\sim 10\,\text{nm} - 20\,\text{nm}$) is expected to remain in a single domain state. Within such cylinders of circular shape in a certain range of sizes the magnetic vortices are formed in the ground state [38]. For applications, such as MRAM cells, which usually try to avoid the vortex formation is important to know the typical sizes of the disks for which vortices do not form. Alternatively, however, one could make use of the vortex formation to write magnetic information on nanoscale. The phase diagram of the different phases of the magnetization as a function of the aspect ratio β, defined as $\beta = L/R$, is shown in Fig. 1.9. One may distinguish four different regions on the diagram. The vortex ground state corresponds to the region I. In region II a single domain structure with in-plane magnetization is formed, while region III corresponds to out-of-plane magnetization. There is also a region IV (dark zone), where the vortex is in a metastable state.

These magnetic nanostructures were observed by using magnetic force microscopy imaging in circular dots of Permalloy with 50 nm in thickness and 0.3 to 1 μm in

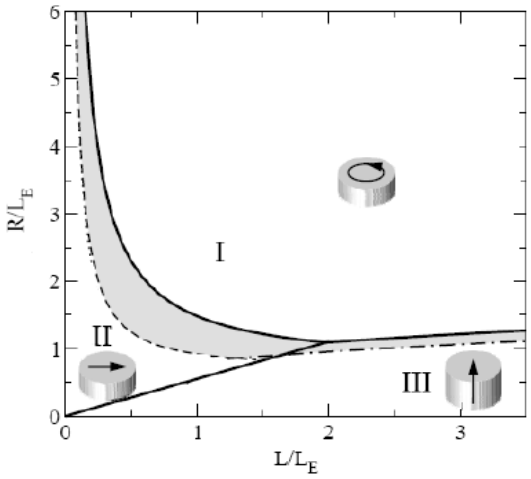

Figure 1.9: The magnetic phase diagram for magnetic disk structures as a function of the radius and the thickness. Both lengths are normalized by the exchange length L_{ex}.

diameter [40]. More recently, the image of the vortex core in nanoislands of iron by using spin-polarized scanning tunneling microscopy, capable of resolving structures down to the atomic scale [39] has been reported. Fig. 1.10 shows the images of the vortex in circular dots reported in [40] and [39].

1.6.2 Spin dynamics in magnetic dots in vortex state and in-plane magnetization state

Although it was back in 1999 when *Cowburn* et al. [38] observed indirectly the vortex state, recently the vortex formation in different magnetic nanostructures has attracted great attention. Currently most of the fundamental studies of the vortex state are mainly devoted to understand the magnetization dynamics in these systems. Short magnetic field pulses are usually applied perpendicular or parallel to the dots plane to achieve the magnetization reversal and to excite vortex related spin wave modes [41] [42]. Characteristic reversal times are in the range of the nanosecond (for non-uniform modes) and sub-nanoseconds (for coherent magnetization rotation).

In the magnetic dots systems one can find a rich variety of spin excitations related to the magnetic vortex: low frequency modes in the range of hundreds of MHz, where the vortex core moves as a whole: the so-called translational mode [43], and high frequency modes, in the range of GHz frequencies named radial and azimuthal modes [44]. The experimental techniques usually used to detect spin

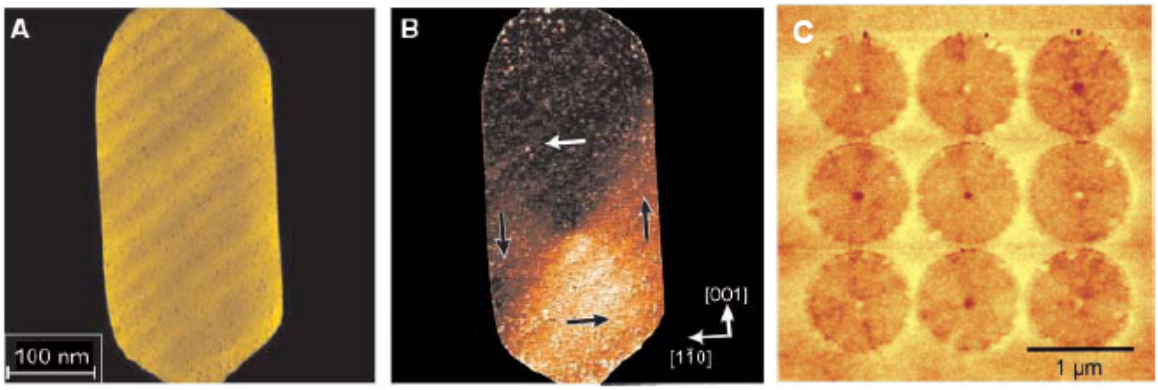

Figure 1.10: (A) Topography and (B) domain image obtained with spin-polarized scanning tunneling microscopy of a single nanoisland of Fe. The arrows indicate the orientation of the domains. (C) Magnetic force microscopy image of an array of Permalloy dots with 1 μm of diameter and 50 nm thick. The central dot in each disk shows the evidence of the vortex formation. Figure adapted from [40] and [39].

dynamics in these nanodevices include photoemission (Brillouin light scattering) and magneto-optical Kerr effect (MOKE). In the last years, however, interest has been also growing to use alternative techniques, such as the vector network analyzer based broadband magnetometer technique. In some cases, however, to increase the sensitivity of this technique the magnetic dot was patterned directly on the microwave circuit, normally presenting a coplanar wave guide (CWG).

Magnetization dynamics in the magnetic dots arrays obeys the LLG equation (Eq. 1.3) with an effective magnetic field $\mathbf{H}_e$ with contributions due to the exchange field ($\mathcal{A}(\nabla m_\alpha)^2$), the dipolar field ($-\mathbf{H}_m \cdot \mathbf{H}/2$), where $\mathbf{H}_m$ is the magnetostatic field, and the external magnetic field ($\mathbf{H} \cdot \mathbf{M}$).

Vortex state dynamics

Low frequency modes: Gyrotropic mode

The vortex core motion at low frequency has been detected by direct imaging with time resolved magneto-optical effect [45] and by the photoemission electron microscopy technique [46].

The first theoretical studies in sub-micron size disks [47] described the translational vortex mode and predicted a spiral-like vortex motion. Based on the Thiele equation [43], *Guslienko* et. al [47] assume that the magnetization is independent of the z component (along the thickness of the dot): $m(\rho, t) = M(\rho, t)/M_S$, where t is the time and ρ is the radial coordinate (in cylindrical coordinates). Ignoring damping, the total force acting on the vortex is

$$\mathbf{F} = \mathbf{G} \times \frac{d\mathbf{R}(\mathbf{x},\mathbf{y})}{dt} - \frac{\partial W(\mathbf{R}(\mathbf{x},\mathbf{y}))}{\partial \mathbf{R}(\mathbf{x},\mathbf{y})} \quad . \tag{1.18}$$

The terms in the equation are the gyrovector $\mathbf{G}$, with a direction into ($P = -1$) or out of plane ($P = 1$) corresponding to the sign of the vortex polarity P, $\mathbf{R}(\mathbf{x},\mathbf{y})$ is the vortex core position in the plane and $W(\mathbf{R})$ is the magnetic energy of the system.

The first term in 1.18 is the gyroforce determined by the non-uniform magnetization distribution or topological charge. The second term describes the restoring force of the vortex shifted from the dot center. This restoring force appears due to the finite in-plane dot size and is directed towards the dot center. For small oscillation amplitude of the vortex around the center $W(\mathbf{R}) = \mathbf{W}(0)+1/2\kappa\mathbf{R^2}$, where κ is the stiffness coefficient. The solution has the form of a spiral motion of the vortex core around the dot center.

The above theoretical prediction was confirmed experimentally by *Park* et al. [45] by using a time-resolved Kerr technique which demonstrated that for circular dots the gyrotropic mode indeed appears in the sub-GHz range ($f < 1\,\mathrm{GHz}$). The dependence of this frequency on the dot aspect ratio β was also reported [48]. The eigenfrequency of the vortex translational mode is described by the following expression

$$\omega_0 = 2\gamma M_S \left[4\pi F_\nu(\beta) - \frac{1}{2}\left(\frac{L_{ex}}{R}\right)^2 \right] \quad , \tag{1.19}$$

where R is the dot radius, L_{ex} is the exchange length and $F_\nu(\beta) = \int_0^\infty t^{-1} f(\beta t) I^2(t)\, dt$. The expression of $F_\nu(\beta)$ contains the functions $f(\beta t)$ defined as $f(\beta t) = 1 - [1 - \exp(-\beta t)]/\beta t$ and $I(t) = \int_0^1 x\ J_1(tx)\ dx$, with $J_1(tx)\ dx$ being the first order Bessel function.

As Eq. 1.19 shows, the translational vortex mode depends on the β value and is independent of the external magnetic field. The influence of the magnetic field can be observed on the amplitude of the signal: the greater the field; the weaker is the translational vortex mode amplitude [48].

High frequency modes: radial and azimuthal modes

There are also other spin waves which can also be generated in the circular dots, the so-called radial and azimuthal modes. The first evidence for these mode was reported in 2004 [49] and one year later an analytical theory was able to explain the experimental results [44].

To resolve the problem one must assume a magnetization inside the circular dot spatially and time dependent: $\mathbf{m}(\rho, t) = m_0(\rho) + \mu(\rho, t)$.

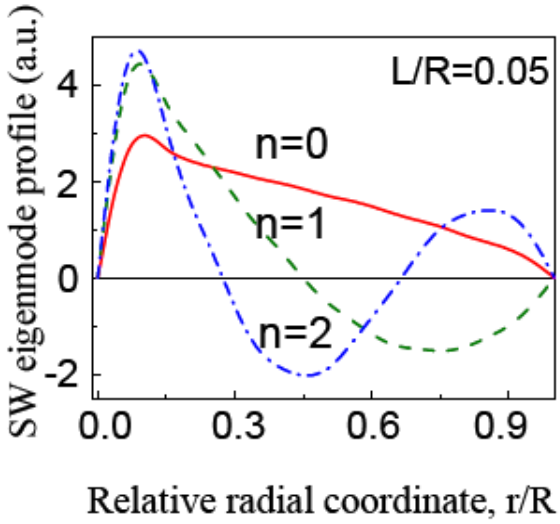

Figure 1.11: Spin wave (SW) profiles for the first azimuthal mode $m = \pm 1$ with three different radial numbers: $n = 0$ (solid line), $n = 1$ (dashed line) and $n = 2$ (dot-dashed line). Picture is taken from [51]

The spin wave modes can be labelled by the number of nodes n and m along the radial ρ and the azimuthal ϕ directions respectively

$$(n, m) \equiv \mathbf{m}_{n,m}(\rho, t) \exp i(m\phi + \omega_{n,m} t) \quad , \tag{1.20}$$

where $\omega_{n,m} = 2\pi \cdot f_{n,m}$, being $f_{n,m}$ the eigenfrequency. For a fixed n a splitting of the eigenfrecuencies occurs for values of m with the same absolute value and different sign. This effect has been studied theoretically [50] [51] and experimentally [52] [53] and confirmed by using micromagnetic simulations [54]. As an example Fig. 1.11 shows the first azimuthal modes ($m = \pm 1$) profiles with radial indices $n = 0, n = 1$ and $n = 2$. Of special interest is the case $n = 0, m = \pm 1$ mode detected and investigated in this thesis (see Chapter 4).

Figure 1.12 reproduces results reported in [49] by using a Fourier transform imaging technique where axially symmetric radial modes up to third order ($m = 0; n = 1, 2, 3$) and non-axially azimuthal modes were observed using time resolve scanning Kerr microscopy.

Spin excitations in the magnetically saturated state in circular nanodots

When an in-plane external magnetic field exceeds the vortex annihilation field of the dot, defined as the magnetic field in which vortex is removed from the dot, the

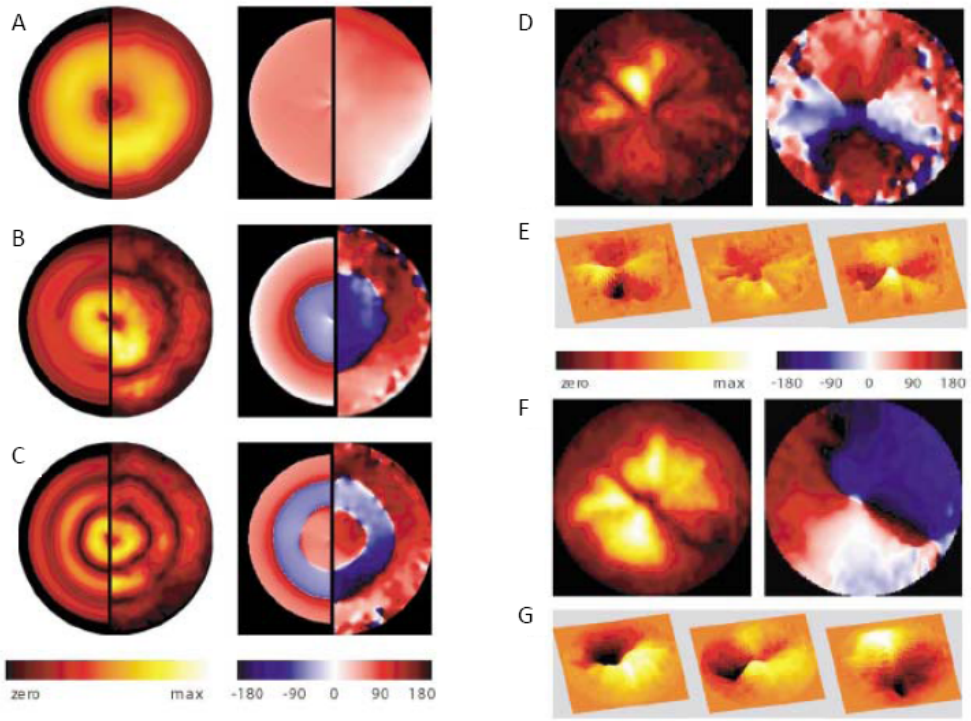

Figure 1.12: From A to C: the Fourier transform images of the axially symmetric modes ($n = 1, 2, 3$ and $m = 0$) at frequencies 2.8 GHz (A), 3.9 GHz (B) and 4.5 GHz (C). Each picture contains two half images. The left from the micromagnetic simulation, the right from the experiment. The dark zones indicate different nodes in the dot. (D) The Fourier magnitude (left) and Fourier phase (right) of the lowest lying non-axially symmetric modes at 1.5 GHz. This mode has two orthogonal radial nodal lines. (D) Temporal sequence of this mode with a time interval of 150 ps. (E) A second observed mode at 1.9 GHz has one in-plane node dividing a dot of roughly equal amplitude but opposite phase. (F) The corresponding temporal sequence of this mode with a time interval of 120 ps. All pictures are adapted from [49].

magnetization will be uniformly aligned in the disk plane. In the case of saturated in-plane magnetization a variety of spin waves can be excited [55] [56]. In addition to the uniform Kittel resonance, the lateral confinement of spins within each dot may cause the discretization of the spin wave spectrum. A huge variety of interesting spin dynamics has been reported, for example magnetostatic surface spin waves (Damon-Eshbach) [57] and magnetostatic backward volume spin waves have been also observed [58] by using the BLS technique. More recently, *Neudecker* et al. [59], by using the vector network analyzer technique combined with Kerr microscopy reported quantized modes in both longitudinal and transverse direction . Moreover, these authors measured the dynamics of the so-called edge mode, the spin dynamics that appears in the dot edges.

1.7 Vortex dynamics in nanostructured superconductors

In the previous sections we have considered the magnetization dynamics in homogeneous (thin films and multilayers) and inhomogeneous (magnetic dots) FM nanostructures. Another example of inhomogeneous magnetic structure is magnetic flux quanta, i.e. vortex forming in type-II superconductors. The magnetic dynamics of this object in plain and nanostructured superconducting films will be investigated via AC transport measurements in this thesis.

In this contest, the next paragraph is dedicated to a brief introduction into superconductivity phenomena and to help the readers to understand high frequency vortex dynamics in restricted geometries described in this thesis. We shall explain necessary conditions for the formation of the superconducting vortices in the presence of an external magnetic field, and how vortices may move under the combined action of current and perpendicular magnetic field. The resulting net movement in restricted geometry is detected via DC electron transport measurements. The periodic vortex movement in asymmetric potentials will be briefly reviewed and the resulting rectification effects introduced. This knowledge will present an important background to explain further how the electric current involving movement of superconducting vortices is rectified by the interfaces of superconductor.

1.7.1 Introduction

One of the most awarded branches in physics is superconductivity. *K. Onnes* in 1913. *J. Bardeen*, *L. Cooper* and *J. Schrieffer* in 1972. *I. Giaever* and *B. Josephson* in 1973. *G. Bednorz* and *A. Müller* in 1987, and finally *A. Abrikosov* with *V. Ginzburg* in 2003 were awarded the Nobel Prize in physics for advances in the superconductivity. These facts underline the importance of this phenomenon from

the point of view of both theoretical and experimental physics.

The discovery of superconductivity took place in 1911 when *Kamerlingh Onnes* observed that the electrical resistivity in *Hg* and of some other elements fell sharply to zero below at a critical temperature T_C, characteristic of the material [60]. During twenty two years it was not clear if there was any essential difference between ideal conductors and superconductors. In 1933 *Meissner and Ochsenfeld* discovered the ideal diamagnetism of the superconducting state [61]. This means that a magnetic field cannot penetrate a bulk superconductor as it is cooled below the critical temperature T_C. The main point is that the magnetic field is expelled from the superconducting sample. This phenomenon was described theoretically by the brothers *F.* and *H. London* in 1935 [62]. Later, in 1950, *Ginzburg and Landau* developed a phenomenological theory capable of describing the superconducting state in the presence of a magnetic field by using the Ginzburg-Landau (GL) formalism, [63]. They introduced the famous complex wave function Ψ as an order parameter for superconducting electrons. The local density of the superconducting quasiparticles is given by the square of this function, i.e. $|\Psi|^2 = n_{sc}$ (in normal state $n_{sc} = 0$). The theory was used by *Abrikosov* to predict a new quantum mechanical state named type-II superconductivity [64]. The history of superconductivity keeps on when in 1957 *Bardeen, Cooper and Schrieffer* explained the microscopic mechanism (BCS theory) responsible for the formation of electron pairs (Cooper pair) [65]. Later, *Gor'kov* [66] has shown that the GL theory is a limiting case of the BCS theory. Finally, in 1986 a new impulse was given to this field with the discovery of high temperature superconductivity in layered copper oxide ceramic compounds by *Bednorz and Müller* [67].

One of the main characteristics of the superconducting state are two important scales introduced in the GL formalism; the penetration depth $\lambda(T)$ and the coherence length $\xi(T)$. The first one determines the distance at which magnetic fields are screened from the interior of the superconductor. The second one determines the distance along which the modulus of the order parameter $\Psi(r)$ can be changed. Both characteristic lengths depend on the temperature in the following way [68]:

$$\lambda(T) = \frac{\lambda(0)}{\sqrt{1 - \frac{T}{T_{C0}}}} \quad , \qquad \xi(T) = \frac{\xi(0)}{\sqrt{1 - \frac{T}{T_{C0}}}} \quad . \tag{1.21}$$

Close to the critical temperature, T_{C0} , $\lambda(T)$ and $\xi(T)$ diverge, while at low temperatures these parameters saturate. The constants $\lambda(0)$ and $\xi(0)$ are determined by the ratio between the electron mean free path l_{el} and the BCS coherence length ξ_0, which is roughly the average distance between electrons forming a Cooper pair.

The ratio between the two characteristic length scales $\lambda(T)$ and $\xi(T)$ define the Ginzburg-Landau parameter κ

$$\kappa = \frac{\lambda(T)}{\xi(T)} \quad . \tag{1.22}$$

In bulk superconductors, the κ parameter is a dimensionless, temperature independent number, whose value determines the distinction between type-I and type-II superconductors.

If we consider superconducting thin films with a thickness d much smaller than $\xi(T)$, one needs to define an effective penetration depth $\Lambda(T) = \lambda^2(T)/d$. For this case, when one defines κ from the Eq. 1.22 the effective value κ_{eff} depends on the temperature. For the thin film geometry κ_{eff} is the relevant parameter determining the distinction between type-I and type-II superconductors.

1.7.2 Type-I versus type-II superconductivity

Type-I and type-II superconductors distinguish from each other due to their different behavior in a magnetic field. The reason for this is the surface energy at a normal/superconducting boundary, σ_{ns}, which is positive for type-I superconductors but becomes negative for the type-II superconductors. The value of κ determines this distinction: if $\kappa < 1/\sqrt{2} \Longrightarrow \sigma_{ns} > 0$ one speaks of a type-I superconductor. However for $\kappa > 1/\sqrt{2} \Longrightarrow \sigma_{ns} < 0$ the superconductor is called type-II. The difference between both superconducting states results in their different $H - T$ phase diagrams, both shown in Fig. 1.13.

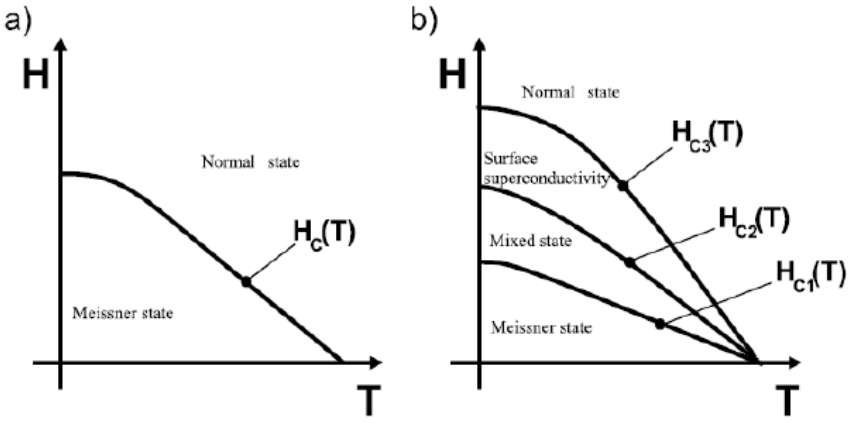

Figure 1.13: Schematic phase diagram drawn for type-I (a) and type-II (b) superconductors.

The properties of type-I superconductor (see Fig. 1.13a) are related to the value of the critical field, H_c. If the magnetic field is below H_c -the sample is in the Meissner state, i.e. the magnetic field is expelled. Superconducting screening currents will create an equal but opposite magnetic field and as a result the total flux inside will be zero. In this region of the phase diagram the superconductor corresponds to a perfect diamagnet. Above H_c the material returns into the normal state. Type-II superconductors (see Fig. 1.13b) show a much richer phase diagram. One can distinguish between four different phases. Below the first critical field, H_{C1}, the superconductor is in the Meissner state. Between H_{C1} and the second critical field, H_{C2}, the superconductor is in the mixed state or Schubnikov phase. The mixed state is characterized by magnetic flux quanta, named vortices, penetrating in the superconductor. If the applied magnetic field is between H_{C2} and the third critical field, H_{C3}, the superconductivity remains only in a small sheet (thickness $\sim \xi$), parallel to the magnetic field at the surface of the sample. Finally, above H_{C3} superconductivity is completely destroyed.

1.7.3 Vortices in type-II superconductors

As we have already seen, the mixed state appears between the magnetic fields H_{C1} and H_{C2}. *Abrikosov* predicted theoretically this part of the phase diagram and noticed that the flux should penetrate not as laminar domains but in a regular arrays of flux "tubes". Each "tube" is carrying a quantum of magnetic flux with the following constant value

$$\phi_0 = \frac{hc}{2e} = 2.07 \times 10^{-7}\,\mathrm{Wb} \quad .$$

Within each unit cell of these flux lines there is a vortex of supercurrent concentrating the flux towards the center. Firstly, *Abrikosov* predicted a square vortex array to be formed. Later, however, it was shown that he had a numerical error in his predictions and the real geometry minimizing the free energy of the system corresponds to a triangular array of vortices (see Fig. 1.14).

A schematic drawing of a vortex consisting of a normal core encircled by superconducting screening currents is given in Fig. 1.15. The three graphs show the radial distribution of the local magnetic field, B, the current density, J and the local density of superconducting electrons, n_{sc}.

In the triangular lattice the distance a between vortices is given by the expression

$$a = \frac{\sqrt{3}}{2}\sqrt{\left(\frac{\phi_0}{B}\right)} \quad . \tag{1.23}$$

The mixed state persists until the external magnetic field reaches the second critical magnetic field value H_{C2}, which is dependent on the coherence length $\xi(T)$.

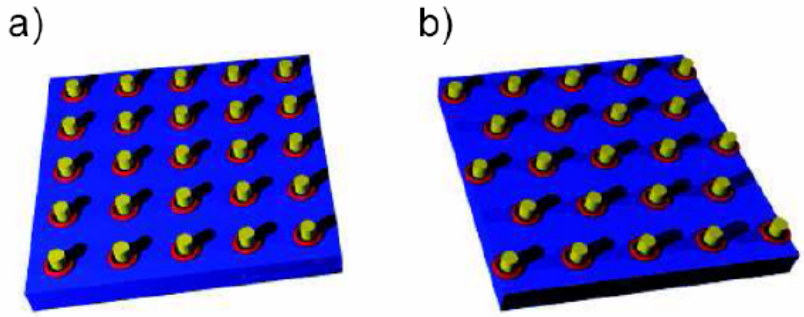

Figure 1.14: The Abrikosov vortex lattice. In (a) the square vortex lattice predicted by *A. Abrikosov* is sketched. In (b) the real triangular vortex lattice with a slightly lower energy is shown.

$$H_{C2} = \frac{\phi_0}{2\pi\xi^2(T)} \quad . \tag{1.24}$$

1.7.4 Vortex dynamics and vortex pinning

One of the main characteristics of the superconducting state is the possibility of electric current transport without energy dissipation. However, in type-II superconductors in the mixed state where vortices are present, the electric current transport may be dissipative. This is due to the interaction between the applied density of current J and the magnetic flux quanta ϕ_0 trapped in the vortex. The vortex is subject to a Lorentz force

$$\mathbf{F}_L = \mathbf{J} \times \phi_0 \mathbf{n} \quad , \tag{1.25}$$

where $\mathbf{n}$ is a unit vector in the magnetic field direction. This force could move the vortex providing the vortex velocity $\mathbf{v}$ and therefore creating an electric field $\mathbf{E} = \mathbf{B} \times \mathbf{v}$. The superconductor will therefore show a finite longitudinal resistivity $\rho = E/J$ because a finite voltage appears along the current direction. This effect will make current transport in the superconductor to be dissipative. In general, the dissipation is an undesirable effect because it may destroy the superconducting state or at least cause noise in some superconducting devices as Superconducting Quantum Interferometer Devices (SQUIDs). The ability to counteract the Lorentz force over the vortex structure may minimize the dissipation problem. The so-called pinning forces are responsible for this counteracting which impedes the movement. When

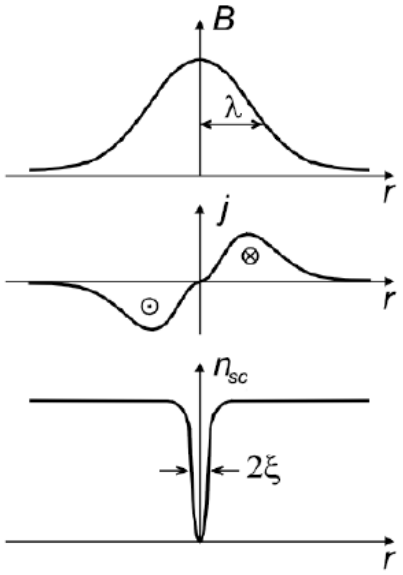

Figure 1.15: Magnetic induction B, current distribution J, and the local density of the superconducting order parameter n_{sc} close to the superconducting vortex.

being pinned, the vortices interact with a well potential to minimize the free energy of the system. This potential wells could have different origins. In real systems, natural centers of pinning center are defects and impurities in the superconducting sample. Defects can locally suppress the order parameter and create therefore a potential well in the site. In the case of magnetic impurities or magnetic particles interaction with the vortex magnetic field can also create a pinning center. In the first case, the dimension of the impurities and defects must be in the order of magnitude of ξ. In the case of magnetic impurities or particles, their dimension must be comparable with the other characteristic length scale λ.

During the last years, the development and improvement of lithographic techniques has made possible the fabrication of superconducting films with periodic arrays of artificial pinning centers with controlled dimensions and shapes. The nature of this pinning lattice can have different origins. Vortices can be pinned by a hole or "antidot" lattice. This kind of periodic vortex pinning has been intensely studied by different groups [69] [70] [71] [72] [73] [74]. Another possibility of controlled pinning is the creation of a patterned lattice of magnetic nanostructures, such as magnetic points, lines, triangles or other type of geometries covered by a superconducting film.

The presence of the artificial pinning centers not only affects the vortex dynamics,

but also their static properties. As it has been shown, in a perfect superconducting sample the free energy is minimized when vortices form the Abrikosov lattice. Artificial pinning centers may change the configuration of the vortex lattice, making that the vortices occupy mainly sites corresponding to the pinning sites.

1.7.5 Vortex rectification effects

Transport of particles in asymmetric potentials, which often occurs in nature processes such as protein transport, have attracted recently much attention. To produce a net displacement of a particle through the "ratchet effect", could be possible with an asymmetric potential even though mean value of the applied force is zero [75]. In the case of type-II superconductors it could be interesting also to create and investigate ratchet mechanisms acting on the vortices. The possibility to manipulate vortices could help "cleaning" the sample of trapped magnetic flux quanta and obtain in this way considerably less noisy devices. The corresponding idea was introduced by *Lee* et. al. [76]. Breaking the spatial symmetry of the pinning potential results in a so-called ratchet potential which is expected to create a net vortex motion and capable of rectifying current. Figure 1.16 shows an example of the vortex dynamics in superconducting films and the asymmetric potential landscape to remove vortices.

To observe vortex rectification two conditions will be required. The first one is to have an asymmetric potential in the system and the second is to apply an external force with zero mean value, for example an AC current. In respect to the first condition, as we have seen in the previous section, periodic pinning centers can be designed on the sample to create an asymmetric and periodic potential. To break the symmetry one can pattern asymmetric pinning centers, such as triangles, boomerang shapes, etc. [77] [78] [79] [80]. In respect to the second possibility, one can inject an AC current along the sample which will create an alternating Lorentz force whose mean value is equal to zero; $\langle F_L \rangle = 0$. The equation of motion on a vortex in a type-II superconductor under the influence of the Lorentz force is given by

$$F_{total} = F_L - \frac{\partial V_P}{\partial x} - F_{drag} + F_{v-v} \quad . \tag{1.26}$$

When the Lorentz force F_L exceeds the pinning force, vortices start to move. The net force on a vortex has different contributions. The first term on the right hand of the equation (1.26) is the Lorentz force. The second term is the asymmetric pinning force due to the inserted asymmetric potential. The third term is the viscous drag force, which is proportional to the velocity of the vortex, and the fourth term F_{v-v}, represents the vortex-vortex repulsive interaction.

So far, vortex rectification effects have been studied using alternative procedures for creation of the asymmetric background potential. Experimentally [81] [82] [83] and theoretically [84] a guided vortex motion into high symmetry directions in a

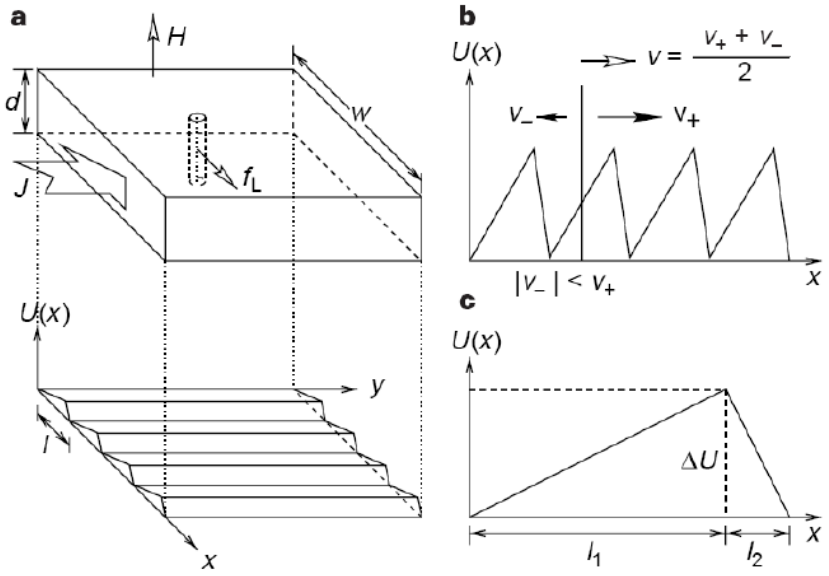

Figure 1.16: (a-top) Picture showing vortex moving in a type-II superconductor in presence of an applied magnetic field H perpendicular to the film plane. A DC current flowing in the film plane (y direction) induces a Lorentz force that moves the vortex in the x direction.(a-bottom). The patterned pinning potential on the superconducting structure. (b) The asymmetric potential used for remove vortices from superconductor.(c) The parameters characterizing a single tooth of the asymmetric potential. (Picture taken from [76]).

periodic pinning potential has been investigated. *Villegas* et al. [74] have studied the ratchet effect in superconducting films with a periodic array of asymmetric pinning centers. The creation of a vortex ratchet using in-plane magnetized dots has been treated by *Carneiro* [85]. More recently *Morelle* et al. [86] have introduced rectification by an asymmetric shape such as mesoscopic triangles and asymmetric superconducting loops. Moreover, the case of asymmetric configurations of symmetrical pinning sites has also been measured [83] [87]. Although several theoretical studies have aimed to clarify the ratchet mechanism of the vortices [79] [80] [78] [76] [77] these systems are still quite far from being completely understood. It is interesting to emphasize that none of the above mentioned reports presented experimental measurements of rectification effects on "control" samples, i.e. reference plain superconducting films without artificially created asymmetric pinning centers.

Chapter 2

Experimental techniques

Over the past sixty years, the experimental techniques for detecting magnetization dynamics are being continuously developed and improved, thanks largely to new experimental devices of signal detection and their greater sensitivity. Keeping on this line, we have developed a new experimental technique for studies of magnetization dynamics between room and low (2 K) temperatures based in network analyzer detection. This is a promising experimental technique, due to its great sensitivity and its relatively simple scheme of measure. This chapter introduces the reader into the various experimental techniques used to investigate magnetization dynamics, with special interest in the vector network analyzer technique and the new set-up developed by our group at the Autonomous University of Madrid during the development of this thesis.

The last part of the chapter explains the second experimental technique used for transport measurements in superconducting nanostructures. The experimental set-up permits to explore rectification effects in type-II superconducting films.

2.1 Experimental techniques on magnetization dynamics

2.1.1 The inductive methods

Historically, the first investigations of the magnetization dynamics of thin films consisted in magnetization reversal studies. Since the 1950s, the reversal time had been measured directly by the induction method [88] [89] [90]. The thin films are first magnetized in a certain direction and then a step pulse magnetic field is applied in the opposite direction. When these magnetic pulses are greater than a critical value (i.e. greater than the coercive field) the direction of magnetization in the thin film reverses and a voltage pulse generated by this reversal is induced in a pick-up coil which is amplified and observed on an oscilloscope. In these measurements the

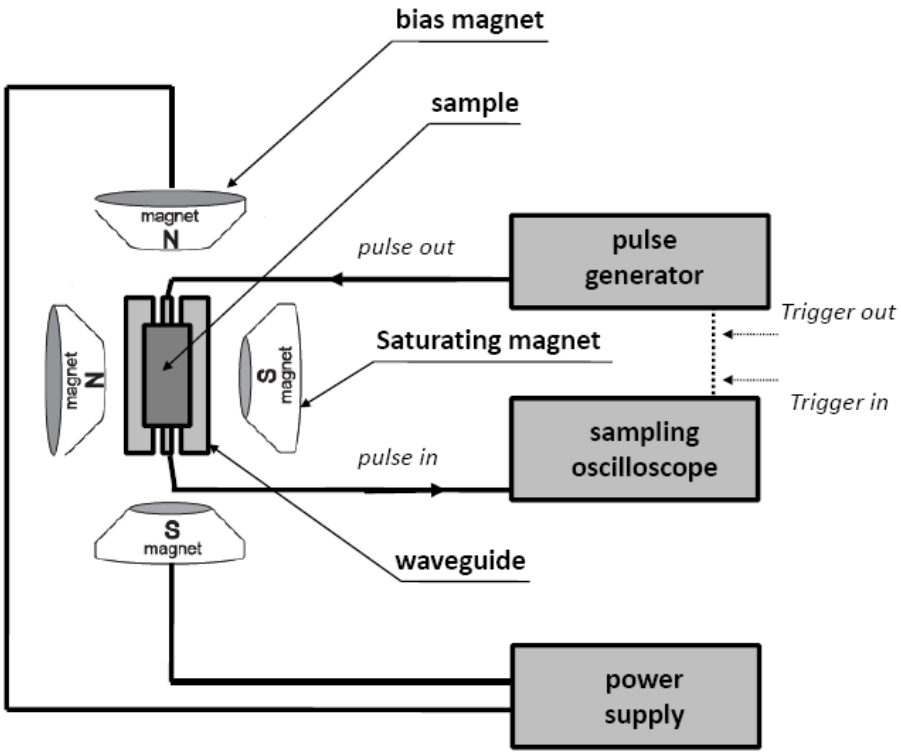

Figure 2.1: A schematic diagram describing Pulse Inductive Microwave Magnetometry (PIMM) technique.

pulse rise time is in the nanoseconds range. In the 1960's, *Dietrich, Proebster, and Wolf* first measured switching speeds of about 1 ns by using the above mentioned inductive technique [91] [92]. Field pulses with a pulse width less than 350 ps were applied transverse to the easy axis of the film magnetization.

With implementation of the magnetic nanostructures such as MMLs, SVs and MTJs in high density storage industry, MRAMs and in spintronic devices, the interest in the magnetization reversal process with magnetic field pulses and in injection of magnetization by a DC current has renewed. The new generation of experimental devices allows to study much shorter pulse rise times and to investigate in more detail the magnetization dynamic process. *Silva* et al. [93] have developed the so-called pulse inductive microwave magnetometry (PIMM) technique to study ultra-high speed magnetic phenomena. Their work include modern high-speed sampling technology, lithographic wave guide fabrication, and digital signal processing [93] [94]. The basic scheme of this method is shown in Fig. 2.1.

The PIMM method is a relatively simple and intuitive technique. A commer-

cial solid-state pulse generator produces the magnetic field step with a rise time of 50 ps. These pulses are sent to a coplanar wave guide where the magnetic film is deposited and subsequently lithographically patterned in its center. When pulses travel trough the wave guide a pumping field that can excite the magnetization of the sample is generated. The transmitted pulse is detected by a high-speed sampling oscilloscope. Perpendicular to the pumping field, an applied magnetic field is supported by an electromagnet, named bias magnet in Fig. 2.1. With the magnetic sample saturated by a large transverse field generated by a second magnet (saturating magnet), a reference wave form in which no magnetic dynamics has occurred is acquired and subsequently subtracted from the previously acquired wave forms allowing the observation of magnetization precessional effects.

2.1.2 The magnetoresistance method

Ultrafast magnetoresistance detection provides a powerful tool to study magnetization dynamics and switching of small individual SVs [95] [96] and MTJs [97] cells of nanometer lateral dimensions. As was described in Chapter 1, these structures have two FM layers, one of which is free to rotate in the presence of an applied field and the other one is pinned. The GMR or the TMR of such devices provide easy access to the dynamics of the FM free layer. When a magnetic field pulse (pumping field) is applied transverse to the magnetization direction of the thin film, the time to switch the magnetization varies between 10 ns to less than 500 ps as the magnetic pulse amplitude exceeds the coercive magnetic field. By measuring the magnetoresistance of the magnetic device one may observe whether the magnetization reversal has happened. More recently, the technique has been applied to the study of ultrafast magnetization dynamics in magnetic nanodots by using time resolved measurements of the anisotropic magnetoresistance [98].

2.1.3 The magneto-optical method

Another technique used to study magnetization dynamics employs time-resolved magneto-optical Kerr effect (MOKE) microscopy, in which the combined picosecond temporal and submicrometer spatial resolutions allow to study directly the time dependence of magnetic excitations and acquire magnetic maps of the sample surface [99]. The observed non-uniform spatial profiles cannot be directly obtained from magnetoresistance measurements. The optical measurements with this technique have been performed by using picosecond pulses delivered by a synchronously pumped laser. The polar [3] or transverse [100] Kerr rotation is monitored by a polarizing beam-splitter and by using a differential diode detection scheme, which measures the linear MOKE signal. Another technique, known as SHMOKE [101] [102] that complements linear magneto-optic techniques and shows an extreme sensitivity to magnetization at surfaces and interfaces [103], uses second-harmonic (SH)

magneto-optics, whereby a sample is illuminated with light of frequency f and generates light at 2f. The light reflecting off the sample is passed through two filters to block the fundamental beam and therefore the second-harmonic light is detected. The nonlinear magneto-optical effects are limited to sites without inversion symmetry and SHMOKE is therefore surface or interface sensitive.

2.1.4 The Brillouin light scattering method

The Brillouin light scattering (BLS) technique has been used in order to study patterned structures such as arrays of ferromagnetic wires [104] [105] and arrays of magnetic dots with vortex structure [106] [107]. This technique is a spectroscopic method to investigate inelastic excitations with frequencies in the GHz range. Basically, a light beam is sent from a frequency-stabilized laser to focus it onto the sample by using an objective lens (see Fig. 2.2). The light scattered from the sample (elastic and inelastic contributions) is then collected and sent through a spatial filter to suppress background noise before it enters the Fabry-Perot interferometer. The photons with energy $E = \hbar\omega_I$ and momentum $p = \hbar q_I$ interact with the elementary quanta of spin waves with energy $E = \hbar\omega$ and momentum $p = \hbar q$, which are magnons. The scattered photons gain energy and momentum $\hbar\omega_S = \hbar(\omega_I + \omega)$ and $\hbar q_S = \hbar(q_I + q)$ respectively if magnons are annihilated. The wave vector $(q_S - q_I)$ transferred in the scattering process is equal to the wave vector q of the spin wave. A magnon can also be created by energy and momentum transfer from the photon, which in the scattered state has energy $\hbar(\omega_I - \omega)$ and momentum $\hbar(q_I - q)$.

2.1.5 The conventional ferromagnetic resonance method

Another powerful method to study magnetization dynamics is the ferromagnetic resonance (FMR) technique. In a FMR experiment an oscillating magnetic field h_{rf} (pumping field) is usually applied transverse to the magnetization direction in presence of an applied magnetic field directed along the easy axis of the magnetization. This configuration creates a coherent precession of the magnetization around a constant effective magnetic field vector composed by external and internal field contributions. When the frequency of excitation h_{rf} coincides with the precessional frequency, the energy of the pumping field h_{rf} is absorbed by the magnetic system, resulting in magnetization precession in an uniform mode, i.e. with all the spin precessing in-phase. A basic diagram of FMR spectrometer is shown in Fig. 2.3, where the thin film sample is placed in a microwave resonant cavity. The FMR signal is measured by monitoring the microwave losses in the studied film as a function of the applied magnetic field. Microwaves with certain frequency travel down in a wave guide to the cavity. The microwave power is coupled to the cavity through a small hole in its upper end wall and some part of the energy is absorbed by the specimen studied and other by the cavity walls. The reflected microwave power is directed by

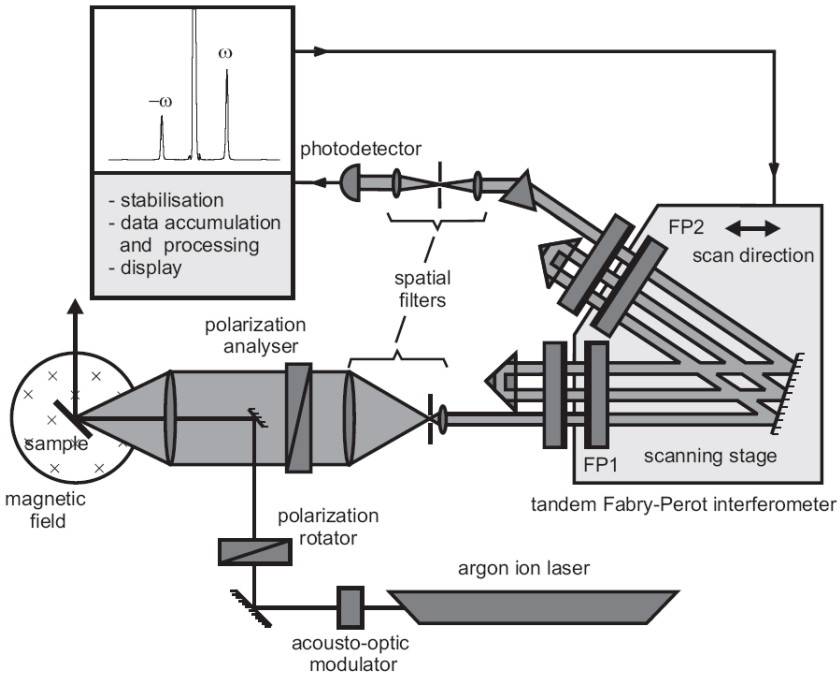

Figure 2.2: Schematic diagram describing the BLS set-up (picture taken from [108])

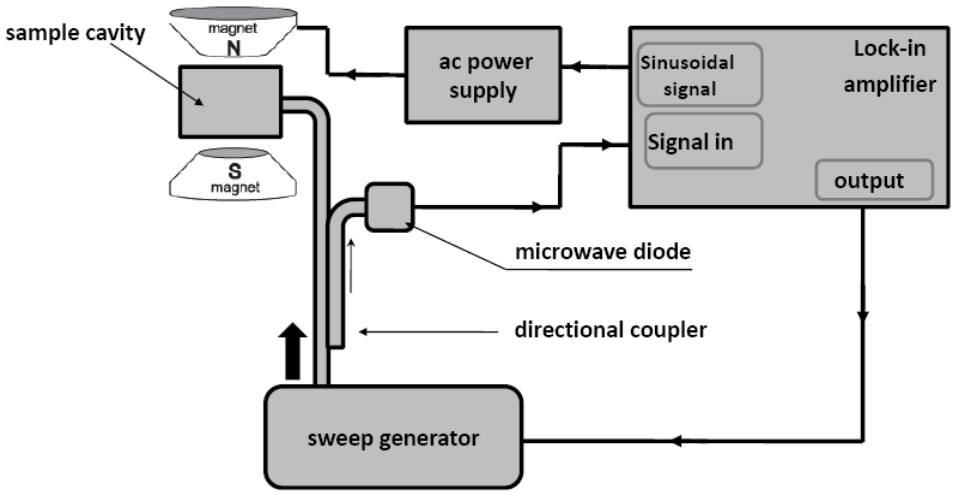

Figure 2.3: A block diagram of an FMR spectrometer. Microwaves of certain frequency travel down a wave guide to the cavity, inside which the thin film sample is located. Reflected power is directed by a microwave coupler and detected by a diode. A low frequency modulation and a lock-in amplifier are used to monitor the field derivative of the reflected power.

a microwave directional coupler to a diode used to detect the FMR signal (power). The applied magnetic field is weakly modulated at low frequencies (in the range of $100 - 200\,\mathrm{Hz}$) and a lock-in amplifier is usually used to detect and amplify the corresponding AC component of the diode voltage. The measured signal is then proportional to the derivative of the reflected microwave electric field amplitude with respect to the sweeping magnetic field.

2.1.6 Comparison between different methods

The experimental techniques described above have some advantages and disadvantages. For example, comparison of two broadband techniques such as PIMM and FMR, with the PIMM method using a pumping field step instead of a microwave excitation in FMR reveals the clear disadvantage of PIMM because of an extremely complicated data analysis with a need to subtract the background pulse. In the case of the FMR and the BLS techniques the magnetization dynamics is studied sweeping the applied magnetic field at a fixed excitation frequency. The FMR method is one of the most powerful techniques in the study of magnetic thin films because of its high sensitivity. Some drawback of conventional FMR is that only fixed frequency values are usually used. FMR allows not only to study the relaxation mechanism of the magnetization, but also to measure other magnetic properties of the films such

as magnetic anisotropy and Curie temperature. With this method ground state properties are studied because only the lowest spin waves with $q \approx 0$ are excited. Moreover, as we mentioned above, FMR has a very high sensitivity and accuracy in determining the position of the resonance peaks. Instead, BLS has the advantage of obtaining a high spatial resolution and of investigating spin waves with different orientation of their wave vectors. This method is normally used in the case of patterned structures because it allows to investigate spin waves with different absolute values and orientation of their wave vectors. On the other hand, BLS allows the detection of thermally excited spin waves, i.e. in this case there is no need to excite spin waves with suitably high wave vectors. Moreover, BLS has high spatial resolution defined by the size of the laser beam focus ($30 - 50\,\mu$m in diameter). This important capability allows to investigate magnetization dynamics in small patterned structures.

2.2 Vector network analyzer technique

During the last years, the vector network analyzer (VNA) technique has proven to be a powerful and relatively simple set-up to study FMR and magnetization dynamics in magnetic nanostructures. In contrast to the conventional FMR technique where one measures the FMR peak and its linewidth by sweeping the external bias field at a fixed frequency, with the VNA technique one sweeps the frequency at a fixed external bias field, performing broadband (several tens of gigahertz) measurements. Although the measured resonance linewidth is still a subject of discussion [109] [110], it is relatively easy to detect the magnetization dynamics.

Studies of the FMR with VNA instrumentation usually employs two ports network analyzers. The VNA provides the real and imaginary parts of the scattering matrix parameters S_{21} and S_{11} that are described in the Appendix A. One of the ports is used to send the microwave signal that travels through the cables and to a coplanar wave guide (CWG) with sample. This travelling microwave produces the oscillating magnetic field h_{rf} (pumping field) in the plane of the CWG which is responsible for the excitation of the magnetization dynamics in the sample. The second port is used for the signal detection. In this way, with the CWG between the poles of an electromagnet that creates the external bias field and by mounting the magnetic sample on top the CWG in a geometrical configuration where the pumping field will be transverse to the sample magnetization, one measures the scattering parameters S_{21} and S_{11}. For a fixed external bias field applied in the plane of the sample to be investigated, the frequency of the pumping field is continuously swept. When the frequency becomes equal to the precessional frequency of the magnetization, the energy is absorbed and observed indirectly in the real and imaginary parts of the scattering matrix parameters.

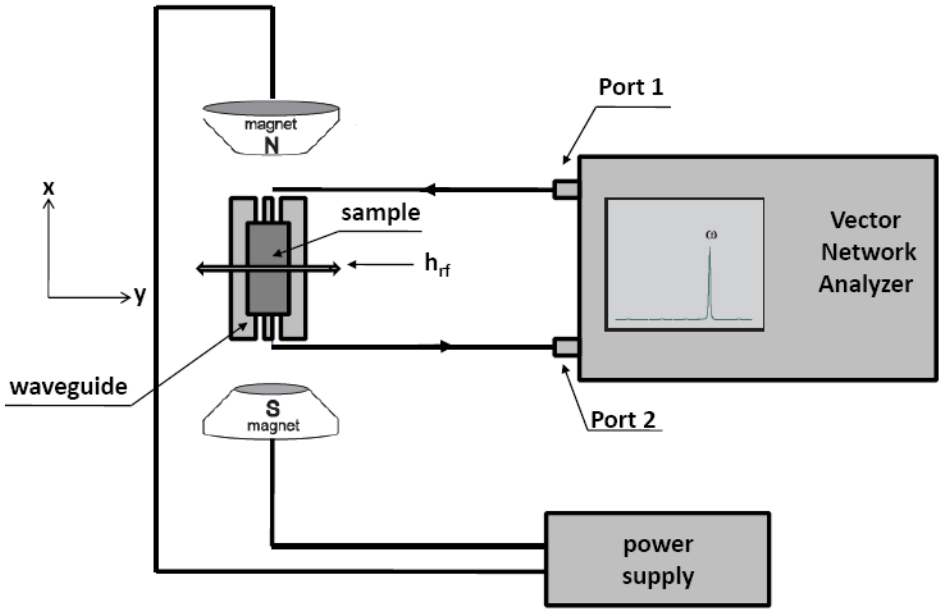

Figure 2.4: Schematic layout of VNA-FMR technique for high frequency magnetization dynamics investigation. The applied magnetic field is directed along **x** direction. The pumping magnetic field created by the wave guide is applied in **y** direction.

2.2.1 Room temperature experimental set-up

Figure 2.4 draws schematically the VNA experimental set-up. The external bias field was applied in the **x** direction while the pumping field (h_{rf}) was generated by the CWG in the **y** direction.

In order to study GHz magnetization dynamics, during the development of this thesis two different network analyzers have been used. Fig. 2.5 shows the two room temperature set-ups used in the experiments. For frequencies from 300 kHz to 8.5 GHz a commercial Agilent E-5071B (ENA series) network analyzer located in the Magnetrans group at the Autonomous University of Madrid, Madrid, Spain was used. This set-up was developed and employed for studying the magnetization dynamics of the arrays of magnetic dots at room temperatures and FMR experiments at low temperatures in MTJs. The external bias field was created by a DC current supplied by a Keithley 2800 multimeter in a home made calibrated electromagnet. On the other hand, for room temperature FMR measurements in MTJs above 8.5 GHz another commercial Agilent E-8363B (PNA series) network analyzer with a frequency range up to 40 GHz was employed. The external bias field was created by

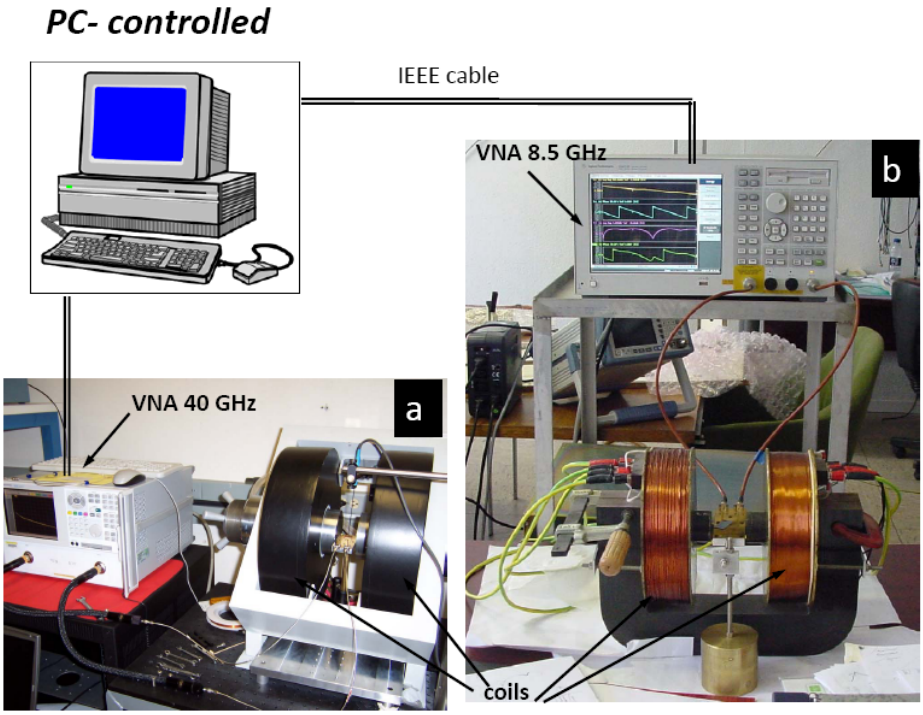

Figure 2.5: Room temperature set up used in VNA-FMR experiments (a) VNA working to 40 GHz located at NIST, Boulder, United States. (b) VNA working to 8.5 GHz located at Magnetrans group at the Autonomous University of Madrid. Both setups are PC controlled. For data flow between PC and devices IEEE cables are used.

a DC current supplied by a LakeShore electromagnet system and measured *in-situ* by using a LakeShore Hall probe. This VNA broadband magnetometer set-up is located in the National Institute of Standards and Technology in Boulder, Colorado, USA, and was used during two 3-month visits to the group of Dr. Stephen Russek. A home made LabVIEW computer program controls the complete measuring sequence: setting external bias field, controlling and measuring the VNA parameters and writing data to data sheets.

2.2.2 Microwave wiring

Investigation in physics of high frequencies (GHz) requires employment of specific microwave electronic components such as coaxial lines and wave guides, where the electromagnetic wave can travel without being reflected by impedance mismatch and only minimally attenuated. The basic microwave lines used in the VNA set-up require coaxial lines and CWG. The coaxial line consists of two round conductors in

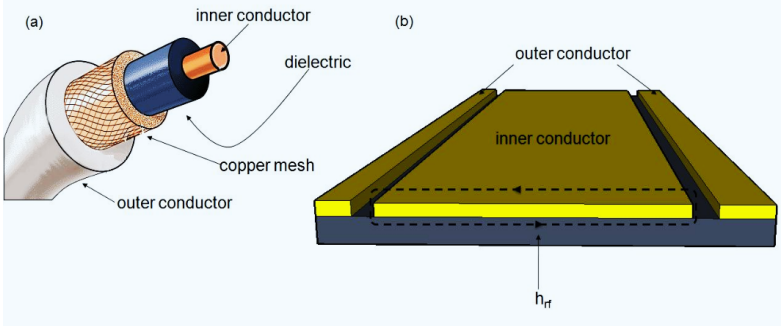

Figure 2.6: (a) Sketch of a coaxial line and (b) a coplanar wave guide. The dashed line indicates the microwave magnetic field generated in the waveguide. This component is crucial to excite the magnetization dynamics in magnetic nanostructures which are put on top of the wave guide.

which one completely surrounds the other, with the two separated by a continuous solid dielectric. A classic CWG is formed from a conductor separated from a pair of ground planes mounted on top of a dielectric medium. A variant of CWG circuit is the so called grounded CWG. In this case, a ground plane is provided in the opposite side of the dielectric plane. The advantage of CWGs is that active devices under study can be mounted on top of the circuit. Figure 2.6 shows a scheme of the two transmission lines described above.

In this thesis we have developed different microwave transmission lines in order to investigate room and low temperature properties related to magnetization dynamics. In the case of the room temperature set-up, connections between VNA ports and the CWG are made with a SMA (SubMiniature version A) coaxial line. SMA connectors are coaxial RF-connectors with a minimal connector interface for coaxial cable with a screw type coupling mechanism and 50Ω impedance, offering excellent electrical performance from DC to 18 GHz. A controllable torque in the different SMA screw coupling, is necessary a calibrated dynamometric wrench to apply 0.90 N· m. The connectors coupled to the CWG are Super-SMA launch connectors that can work up to 27 GHz and ensure a 50Ω matching line. The grounded CWG was fabricated on a gold conductor with an inner conductor thickness of 375 μm and a gap distance between inner and outer conductor of 140 μm. The insulator material is a glass reinforced hydrocarbon/ceramic laminate with dielectric constant of $\varepsilon_r = 3.66$. Additional to this, in order to have a good ground connection, an array of microholes was designed surrounding the ground planes on the CWG. A detailed image of this CWG is shown in Fig. 2.7.

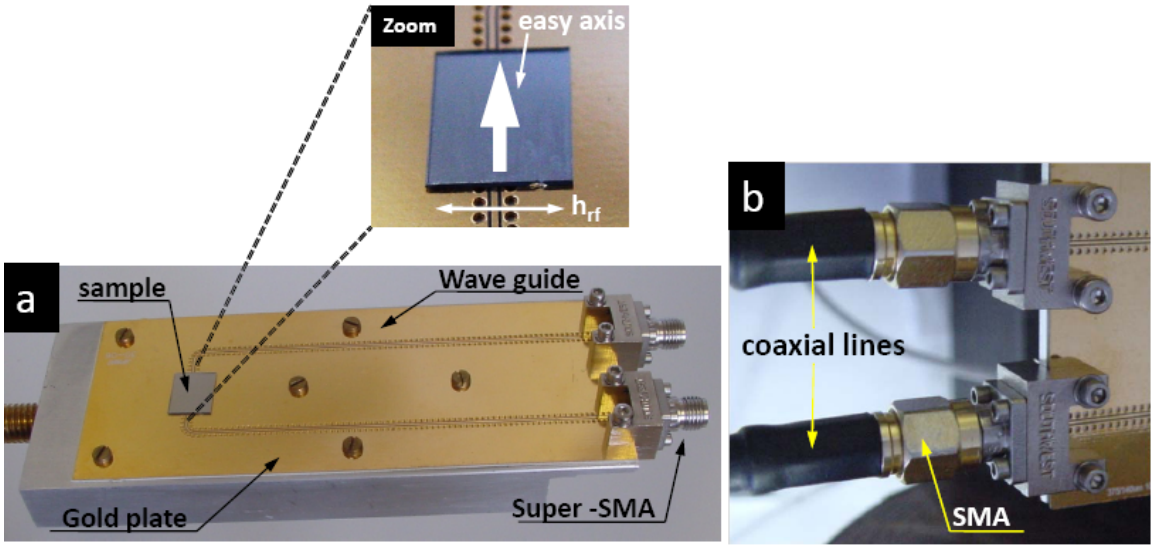

Figure 2.7: (a) The wave guide used to measure room temperature magnetization dynamics in magnetic nanostructures. (Zoom). A detailed of the sample position and how the pumping field h_{rf} is applied transverse to the easy axis of the sample magnetization. (b) A detail of connections between the coaxial lines and the wave guide, in our case a SMA/Super-SMA connections were used.

2.2.3 Data analysis

In order to determine the physical parameters describing the dynamic response of the system, different evaluation methods have been proposed in the literature. *Kuanr* et al. [111] evaluate the resonance frequency and its linewidth from the magnitude of the transmitted signal S_{21} directly. By measuring the spectra for a fixed bias field they subtract the spectrum where there is no magnetic signal from the sample. The magnetic response of the sample is evaluated by using the following expression:

$$U(f)_{Ku} = \frac{|S_{21-H}(f)|}{|S_{21-ref}(f)|} \quad , \tag{2.1}$$

where $|S_{21-H}(f)|$ denotes the magnitude of S_{21} measured for a bias field H and $|S_{21-ref}(f)|$ the magnitude of S_{21} measured at the reference field. Then they fit the magnetic response $U(f)_{Ku}$ to a lorentzian curve to evaluate the resonance peak and its linewidth.

On the other hand, *Kalarickal* et al. [112] adopt another evaluation method based on the transmission line model developed by *Barry* [113]. In this case, they measure the real and imaginary parts of S_{21} for a fixed bias field and subtract a reference spectrum measured without magnetic signal from the sample. If reflections in the line are neglected, assumption that we adopt in all the analyses shown in this thesis, the magnetic response is related to the microwave permeability of the sample in the following way [112]:

$$U(f)_{Ka} = \pm i \frac{\ln\left[S_{21-H}(f)/S_{21-ref}(f)\right]}{\ln\left[S_{21-ref}(f)\right]} \quad , \tag{2.2}$$

the real part of the evaluated signal, $Re[U_{Ka}(f)]$, shows the dispersion of the signal and the imaginary part, $Im[U_{Ka}(f)]$, corresponds to the FMR loss profile. The sign of $U(f)$ is chosen such that $Im[U(f)]$ becomes negative in the vicinity of the FMR peak. Finally, the resonance and linewidth of the FMR peak are evaluated by fitting simultaneously both real and imaginary parts to a lorentzian model (see Appendix B).

More recently, *Bilzer* et al. [114] have developed an evaluation method taking into account the reflections on the system. While the difference between the evaluated resonance frequencies with different methods show close agreement, with variations of less than 1%, the resonance linewidth shows variation of less than 10%.

Due to some differences between the magnetic systems studied in this thesis, the evaluation method used will depend on the system under investigation. In the case of arrays of magnetic dots we have very weak magnetic signals. In order to obtain a best fit to the lorentzian curve, is more convenient to evaluate the magnetic response using the *Kuanr* et al. method [111]. On the other hand, MTJs present very high magnetic signals so that we adopt the evaluation method developed by *Kalarickal*

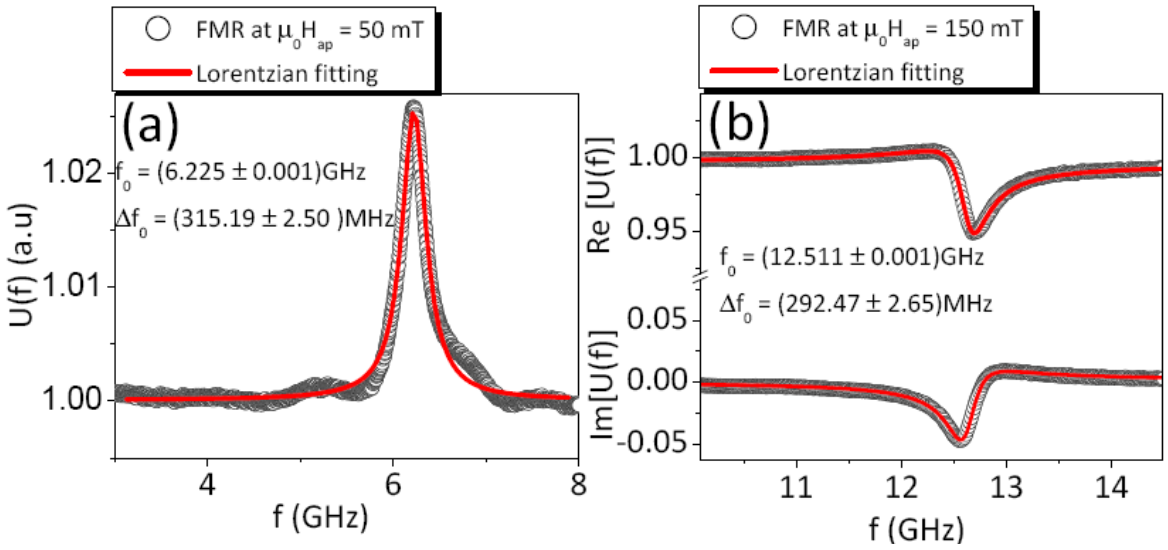

Figure 2.8: (a) FMR spectrum (open circles) evaluated by Kuanr method measured in arrays of Permalloy magnetic dots with in-plane saturated magnetization. The red line shows the fit of the spectrum to a lorentzian curve. (b) In the case of magnetic tunnel junctions the FMR spectrum (open circles) is evaluated by using Karalickal method, fitting simultaneously the real and imaginary part to a lorentzian curve (red lines).

et al. [112]. Figure 2.8 illustrates both evaluation methods with their respective fittings to a lorentzian model.

2.3 The cryogenic system

The cryogenic system was used to measure the high frequency magnetization dynamics in MTJs and the high frequency rectification effect in superconducting films. The measurements at low temperatures down to 1.5 K have been carried out in a commercial ultra low loss (<5l/day loss) ^{4}He cryostat from Janis Research Company equipped with a variable temperature insert and with a 9 T superconducting magnet. A detailed scheme of the cryostat is given in Appendix C. The cryostat

has two different ^{4}He systems: the inner ^{4}He flow system with a variable temperature insert with the sample stick inside, and the outer 50 liters ^{4}He reservoir containing a superconducting magnet. Both ^{4}He reservoirs are thermally isolated from their environment by vacuum shielding. Besides vacuum shielding, the outer

reservoir has a liquid N_2 thermal protection shielded. The temperature inside the variable temperature insert is controlled by changing the pressure in the He-flow system with a high vacuum pump and by a LakeShore-340 temperature controller using two calibrated Ge temperature sensors. In addition, a second separate loop of LakeShore-340 controls the temperature in the gas-flow system through a mechanically manipulated capilar. A proportional–integral–derivative controller (PID) between temperature reading (Lake Shore) and temperature controlling (butterfly valve) results in a temperature stability better than 1m K for the temperature range between 1.5 K and 50 K and about 10m K from 50 K to room temperature. The PID is a generic control loop feedback mechanism. PID controller corrects the error between a measured process variable and a desired setpoint by calculating and then outputting a corrective action tuning the proportional (P), integral (I) and derivative (D) values.

A superconducting magnet system is situated at the bottom part of the cryostat. The magnet consists of a twisted multifilamentary NdTi/Cu solenoid. The system has been designed and manufactured for Janis Research Company. The operating current up to 100 A and voltage up to 5 V is supplied by a power source from American Magnet System, which allows to create magnetic fields up to 9 T.

The microwave stick

The low temperature magnetization dynamics measurements in MTJs were performed in a home made microwave stick. We created and developed a microwave stick capable of working in a range of temperature from 1.5 K to 300 K and at frequencies up to 13 GHz.

The microwave stick has three different parts: the top part (head), the middle part (body) and the bottom part. The head is the part of the stick connected to the VNA using SMA connectors. The middle part contains the microwave wiring that connect the stick head to the bottom part, where a sample holder is placed. The sample holder is a Cu piece containing the Ge thermometer and where one fixes the CWG with the sample on top. Once the sample has been properly placed on the CWG the sample holder is closed with a protective cylinder made of teflon.

The microwave wiring was done using special low temperature-high frequency semi-rigid coaxial RF cables UT-85 B-B with a beryllium center conductor and jacket. The connection between this cables and the CWG was done using small SMP (SubMiniature version P) connectors, a high frequency coaxial connectors with 50Ω impedance capable to work up to 40 GHz. Due to the reduced dimension of the cryogenic zone we used a specially designed CWG with the same dimensions of inner conductor thickness and gap distance and dielectric constants as the one used for room-temperature CWG but having reduced size. Figure 2.9 illustrates some details of the microwave stick.

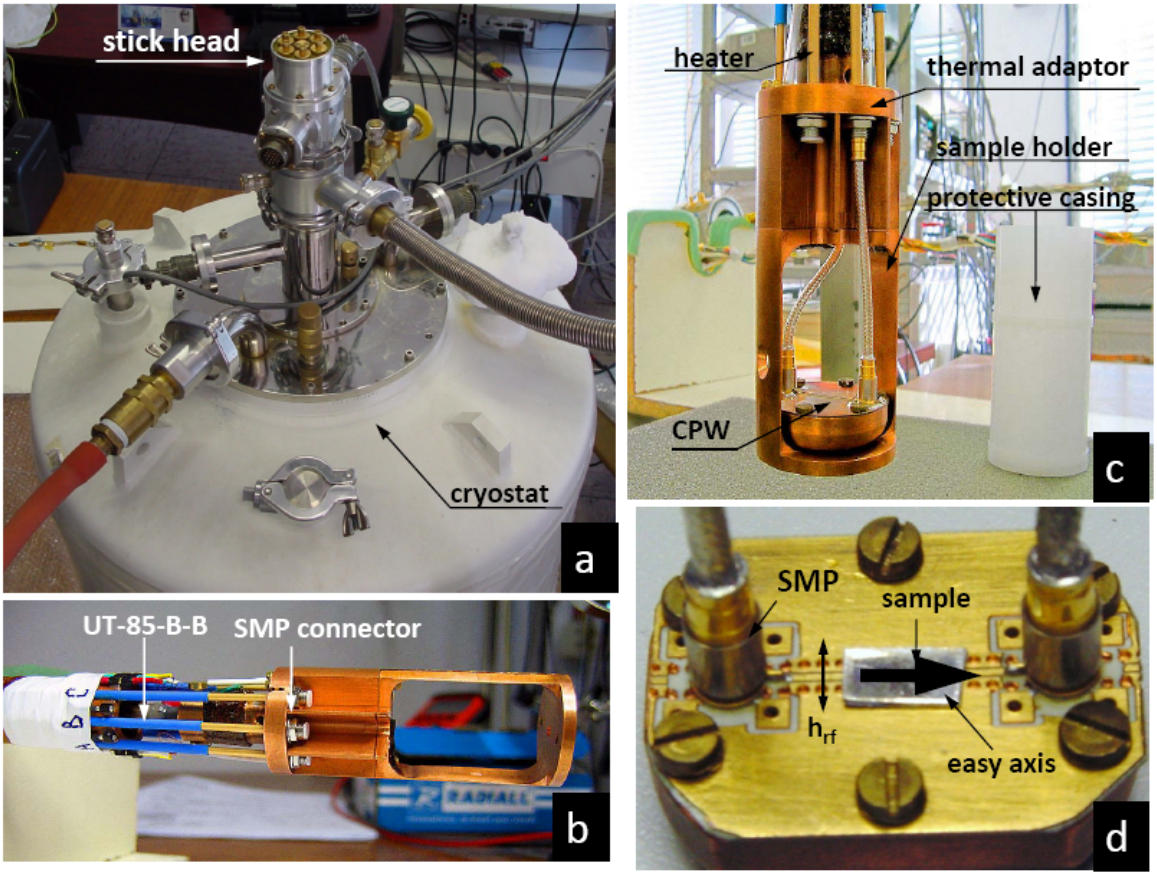

Figure 2.9: (a) The stick head with SMA connectors in the cryostat developed and used in the low temperature measurements. (b) Bottom part of the insert with semirigid UT-85-B-B cables and SMP connectors. (c) The sample holder with microwave rigid cables connecting UT-85-B-B cables with the wave guide, on the right side the protective casing. (d) A detailed of the low temperature waveguide with SMP-connectors, the sample is mounted on top, being the pumping field h_{rf} transverse to the easy axis of the sample magnetization.

The commercial stick

The rectification effect in superconducting this films was performed using a commercial stick from Janis Research Company capable of working in a range of temperature from 1.5 K to 300 K and at frequencies up to 200 MHz by using LakeShore CC-SS-50 coax. cables.

In the case of the superconducting samples is crucial to control, as accurately as possible, the real temperature of the system, because the fluctuations near the critical temperature of superconductors may cause incorrect measurements. By measuring simultaneously transport and noise close to the critical temperature of nanostructured Pb films we verified that the presence of two control loops results in a temperature stability better than 0.2m K during 3 days close to 7 K [115].

2.4 Transport measurements in type-II superconductor

Using a four probe technique two types of transport measurements are carried out to obtain the properties of the superconducting thin films. First, DC measurements were used to obtain the critical parameters of the sample such as critical field H_C, critical temperature T_C and critical current I_C and IV characteristics. On the other hand, the AC measurements have been performed to investigate the rectification effect of the films.

DC measurements

DC measurements techniques were used for investigation of the critical parameters. The resistance was measured using a Keithley 2182 nanovoltmeter while the magnetic field or the applied DC current was injected using a Keithley 2400 Multimeter. A home made LabVIEW computer program, controls the measuring sequence.

AC measurements

AC transport measurements up to MHz range were performed to investigate the rectification effect in superconducting films. Basically, the AC measurements consist of measure the difference of voltage between two points of the sample when an AC current along the film is applied.

While for frequencies below 300 kHz the AC current was measured directly by a Keithley 2400 Multimeter The AC current with a frequency range from 9 kHz to 147 MHz was applied by sending an AC voltage with a Rohde & Schwarz Signal Generator SM300 through two capacitors. These capacitances were tuned for each studied frequency to maximize the impedance matching of the system to 50Ω. The

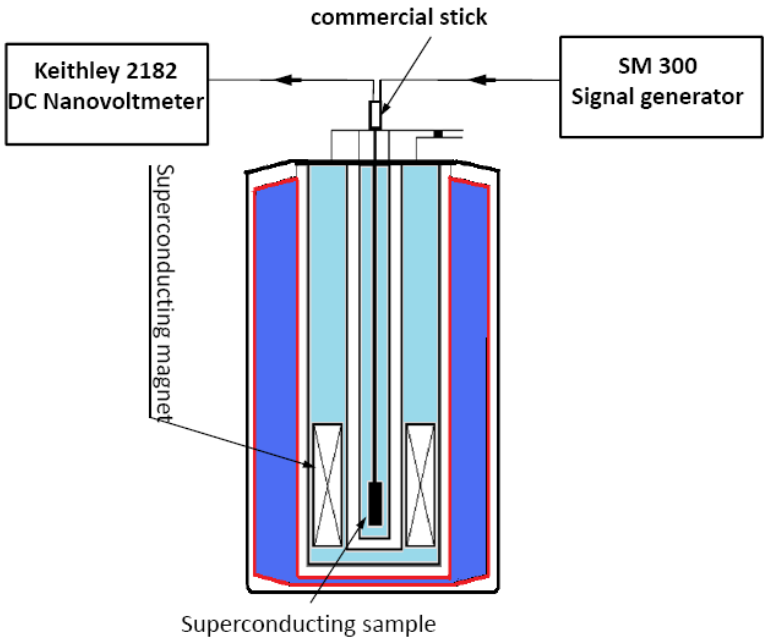

Figure 2.10: Experimental set-up for AC transport measurements in superconducting samples. The AC voltage is generated by the signal generator (SM300), creating the AC current that travel through the cables in commercial stick. The DC voltage between electrical contacts is measured with a Keithley 2182 nanovoltmeter

capacitors were placed on opposite sides of the sample and served also to avoid any possible DC component from the AC current. Voltage readout was done with a Keithley 2182 nanovoltmeter. Moreover, in order to evaluate the AC current values sent to the sample and select the best frequencies for the measurements we performed a calibration of the stick (see Appendix D).

The temperature stability better than $1m$ K for the temperature range between 1.5 K and 50 K and about 10m K from 50 K to room temperature was crucial to investigate the rectification effect near the critical temperature of the samples.

Once the AC current is applied in the film plane and simultaneously the magnetic field, generated by the superconducting magnet system is applied perpendicularly to the film a home made LabVIEW computer program, controls the measuring sequence: setting temperature, magnetic field, AC current. Measuring DC voltage and writing data to data sheets.

Figure 2.10 shows the scheme of the experimental set-up.

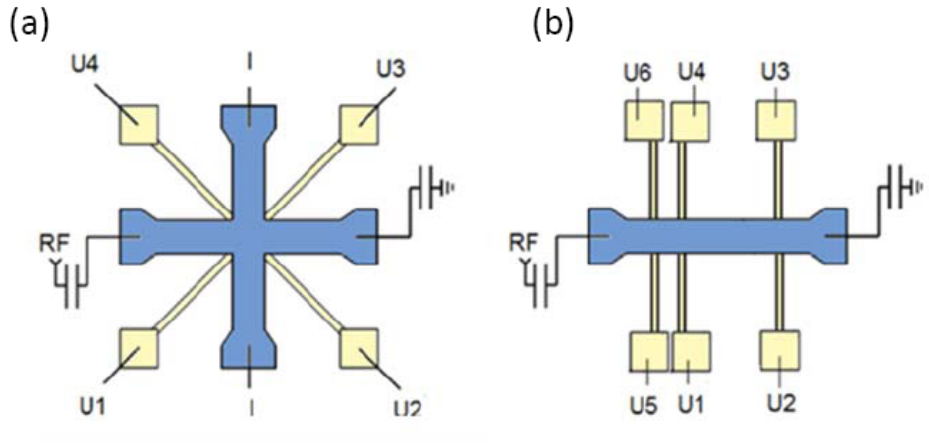

Figure 2.11: Sketch showing typical superconducting samples designs. (a) Cross shaped geometry. (b) Strip geometry. Labelling of the contact will be used in data description presented in Chapter 3.

Sample design

In order to do transport measurements a well sample design is needed, which has the possibility to use a four probe technique. To fulfill this condition the sample needs at least two current contacts and two voltage contacts.

The sample design are shown in Fig. 2.11. The design consist of a cross and strip shape optically lithographed on the samples. The first one (a) has four voltage contacts placed in the corners of the cross, two contacts for the DC current (I) in opposite sides of one arm of the cross, and two contacts for the AC current (RF) on the opposite sides of the perpendicular arm. The second one (b) has six voltage contacts and to AC or alternatively DC current contacts.

Chapter 3

High frequency rectification in superconducting films

3.1 Introduction

According to the induction law, the relaxation of a vortex system in type-II superconductors leads to the appearance of an electric field. In some cases, mainly in superconductors with apparent asymmetry, under periodic change of an external magnetic field, the current, or both, the corresponding time-dependent electric field has a non-zero time average. These phenomena have been called rectification effects and were first reported in the sixties and early seventies. Different manifestations of this effect are the appearance of a DC electric field between the edges of a superconductor due to the existence of different critical currents for opposite current directions [116] [117] [118], by a combined action of a DC current and a DC magnetic field [119] [120], DC and AC currents [121], the presence of anisotropic pinning centers [122], their arrangements [123] and some others [124]

From the point of view of the technological applicability the rectifiers, also known as diodes, represent one of the most important components of modern electronics. Different ratchet systems based on molecular [125], carbon nanotubes [126], ballistic nanojunctions [127], tunneling [128] or superconducting ratchets [122] [129] has been proposed, where the one-dimensional asymmetry on these systems was investigated. A recent renewed interest in nanostructured type-II superconducting films aimed on the control over the vortex motion in superconducting films allowing to remove unwanted vortices [76].

Samples with artificially nanostructured non-symmetric pinning centers have been investigated deeply by injecting current with different directions relative to the anisotropy background potential of the sample [76] [79] [122] [123] [130] . Previous studies explored the rectification effect mainly in the kHz range and in superconducting films without apparent anisotropy (in critical current, DC current or DC

applied field, etc.), however it would be highly desirable to make possible to generate DC electric fields in response to AC current in the kHz and the MHz range in superconducting films without apparent (created by purpose) anisotropy.

With this idea in mind, we have carried out a detailed study of the low (kHz) and high (MHz) frequency vortex dynamics in Pb) and Nb plain films and Pb and Nb nanostructured films where periodic pinning centers were create, which create AC current rectification. The rectification phenomenon is measured by using voltage contacts attached to the edges of the superconducting film either parallel or transverse to the electric current direction. It is shown that the high frequency rectification cannot originate from natural or artificially created vortex pinning anisotropy but most probably due to influence of asymmetric surface (Bean-Livingston-like) barriers for vortex entry and exit into the sample. Alternatively, rectification is explained by a geometric barrier model.

3.2 The superconducting samples

The samples investigated here were grown in the Catholic University of Leuven (V. V. Moshchalkov group) and in the Complutense University of Madrid (J. L. Vicent group).

3.2.1 Nb films

The experiments were performed on plain and nanostructured Nb films with thickness (d) of 100 nm. In both cases, the Nb was deposited on silicon substrates by DC magnetron sputtering. Nb is a type-II superconductor with a T_C of 9.2 K in bulk samples. It is known that the T_C of Nb films with a thickness below 150 nm have a lower T_C than bulk samples [131]. In the films investigated T_C ranged from 8.35 K to 8.75 K. Besides, the effective penetration depth increases with decreasing thickness of the film, so that in our samples has a zero temperature value $\Lambda(0) = \lambda^2(0)/d$ of 160 nm, in comparison with a value around 40 nm in bulk samples [131].

The Nb plain films were optically patterned to cross shape, with a cross area of $40 \times 40\,\mu m^2$, or alternatively to strip shape, of width $40\,\mu$m. In the first sample, the alternating current was injected through opposite arms of the cross, and a direct current (I) could also be injected through the other two perpendicular arms. Four voltage contacts (U_1, U_2, U_3 and U_4) are situated in the corners of the middle square of the cross. In the case of the strip, the alternating current is injected from the ends. On the sides of the strip six contacts allow to measure voltages in longitudinal direction at two different distances ($40\,\mu$m and $320\,\mu$m), and also in the direction transverse to the current (transverse voltage).

The nanostructured sample was prepared by patterning a rectangular array of Ni dots by electron beam lithography and DC magnetron sputtering. On top of

these dots a 100 nm thick Nb film was sputtered. By means of optical lithography the sample was patterned in cross shape geometry with a cross area of $40 \times 40\,\mu m^2$. The dimensions of the Ni dots were 250 nm diameter and 40 nm height. It is known that these dots have in-plane magnetization acting as strong pinning centres for the vortices due to edge stray fields. The size of each rectangle (lattice unit cell) was $0.4 \times 0.5\,\mu m^2$ regular lattice. Further information about films growth and characterization can be found in references [132] and [133].

Figure 3.1 shows the contacts configuration of the cross (a) and strip (b) shapes and some images taken with scanning electron microscopy (SEM) in plain (c) and nanostructured (d) Nb samples.

3.2.2 Pb films

In this case the experiments were performed on plain and nanostructured Pb films. As in the Nb films, the superconducting Pb films with thickness of 50 nm were deposited on silicon substrates. Pb is a type-I superconductor with a $T_C = 7.2$ K, but it has been shown [134] that the Pb films also correspond to a type-II superconductor due to the decrease of electronic mean free path in thin films. In fact, in the case of a Pb film, the critical thickness for this transition is of 250 nm. In addition, to prevent oxidation, the Pb films were covered by 20 nm of Ge protection layer.

The plain film with six voltage contacts was optically patterned to a strip shape of 100 μm width with a distance between longitudinal voltage contacts of 150 μm. On the other hand, a cross shape nanostructured Pb film with a square periodic pinning array of circular holes (antidots), so-called periodic pinning centers (PPCs), with diameter of 0.6 nm and period 1.5 μm and a cross area of 300×300 μm^2 was fabricated using electron beam lithography. The sample has a $T_C = 7.22$ K (for more sample details see Ref. [135]).

Figure 3.2 shows a surface image of the sample using atomic force microscopy (taken in the Catholic University of Leuven).

3.3 Vortex rectification effects in plain Pb and Nb films

The discussion will start with the investigation in plain Pb strip shaped films in a frequency range from 9 kHz (low frequency) up to 43 MHz observing the one-dimensional (1D) character of the vortex dynamics at low frequencies and how its character changes when one applies higher frequency drive currents. In the second part of this section, a detailed investigation of the plain Nb films with different shapes will be shown: cross shape and strip shape samples. It will be shown that the vortex dynamics in the high frequency range has a two-dimensional (2D) character.

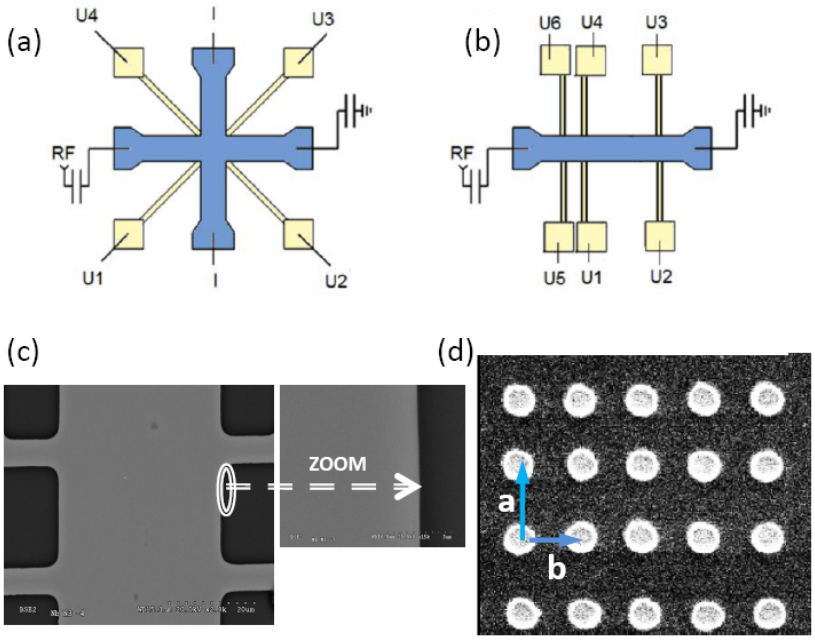

Figure 3.1: Sketches showing contact geometries of the samples . (a) The cross shaped configuration has four voltage contacts (U_1, U_2, U_3, U_4) in the corners of the cross, two contacts for DC current (I) in opposite sides of one arm of the cross, and two contacts for the AC current (RF) on the opposite sides of the perpendicular arm. The figure shows two capacitors to isolate the AC arm from direct currents (b) The strip configuration has two AC current contacts (RF) on opposite sides of the strip, and six voltage contacts (U_1, U_2 ,U_3, U_4, U_5, U_6), which allow to measure voltage at different distances along both sides of the strip, as well as in the transverse direction. (c) Scanning electron microscope (SEM) image of the plain Nb film (strip shape), the zoom image shows the quality of the edge sample. (c) SEM image of the array of Ni dots on nanostructured Nb film ($a = 0.5\,\mu$m, $b = 0.4\,\mu$m)

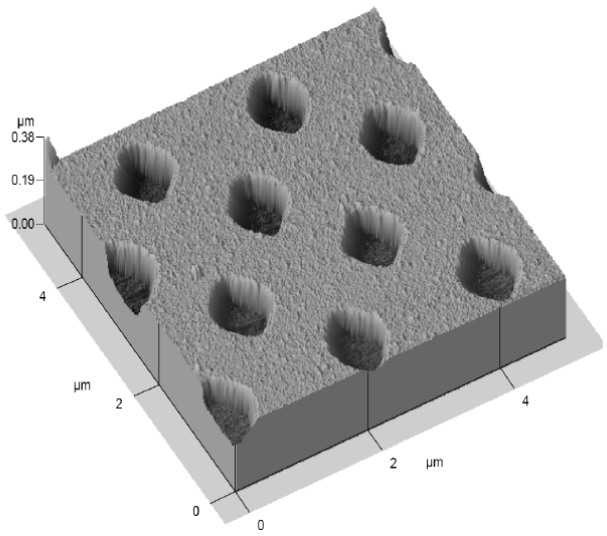

Figure 3.2: Atomic force microscope image on nanostructured Pb film with square periodic pinning array of circular holes (image provided by Lieve van Look, Catholic University of Leuven).

3.3.1 Plain Pb film

First, we discuss the rectification effects investigated in the plain Pb film with strip shape. During the measurements the magnetic field was applied perpendicularly to the film plane. First of all, the low frequency regime and its characteristic vortex dynamics was explored. Figure 3.3 shows the typical longitudinal and transverse DC voltages as a function of the temperature, generated in the Pb film at the low drive frequency of 9 kHz for an applied magnetic field of 2 G.

Moving clockwise around the four pairs of the voltage contacts, independently of the applied magnetic field, one finds nearly opposite DC voltages for the longitudinal contacts at the opposite sides of the strips and relatively small transverse voltage differences. The resulting nearly uniform longitudinal electric field can be explained in terms of the AC driven net 1D vortex flow in the direction transverse to the strip, with the direction indicated by the arrow. When one increases the drive frequency, the transverse DC potential difference becomes comparable to the longitudinal one. Figure 3.4a shows the transverse and longitudinal rectified voltages measured at 99 kHz.

In all the experiments, independently of the drive frequency, the sum of the DC potential difference along all four pairs of the contacts $U_{1-2}-U_{2-3}-U_{3-4}-U_{4-1}$ is very small (crosses in Fig. 3.4a). This proves that the total number of vortices inside

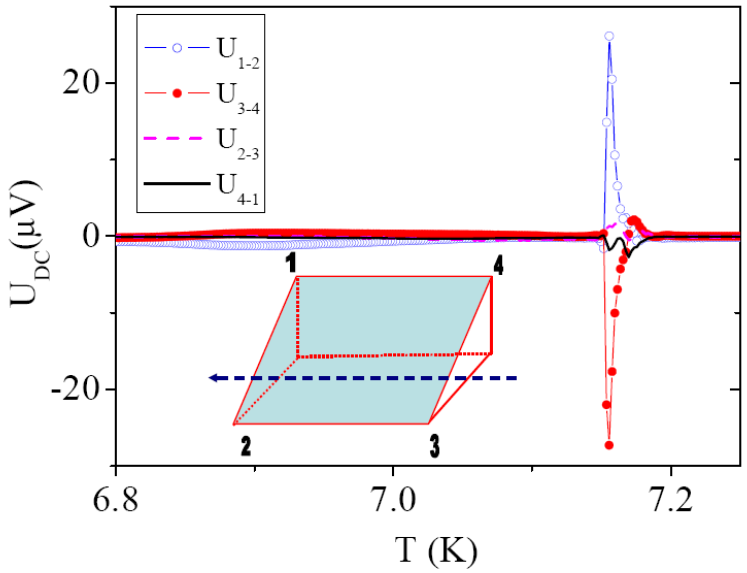

Figure 3.3: Two opposite longitudinal and two transversal rectification voltages as function of temperature measured for Pb strip with $H = 2\,\mathrm{G}$, $f = 9\,\mathrm{kHz}$, and $I_{AC} = 1.7\,\mathrm{mA}$. The lower inset sketches rectification voltage profile generated at low AC drive frequencies. The arrow indicates dominant net vortex flow.

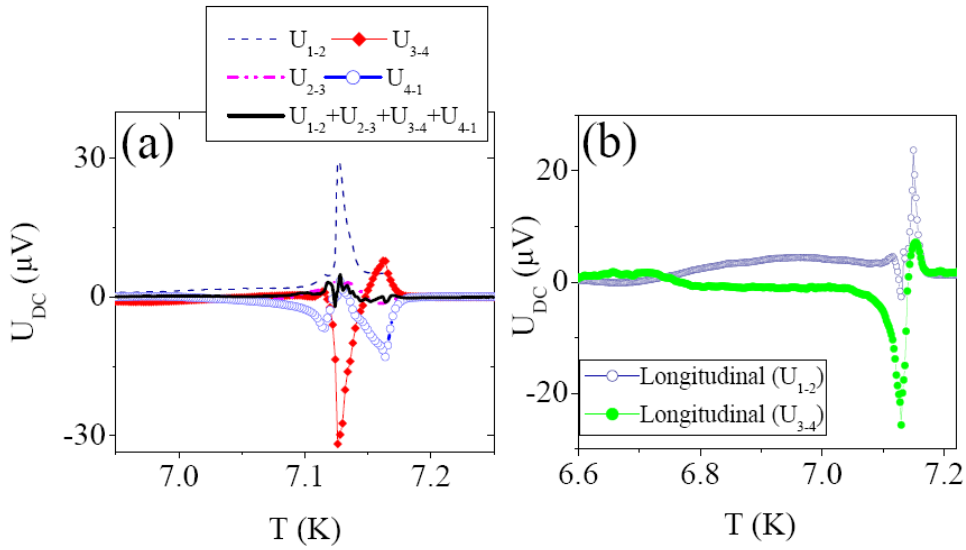

Figure 3.4: (a) Transverse and longitudinal voltages measured for $f = 99\,\mathrm{kHz}$, $H = 8\,\mathrm{G}$ and $I_{AC} = 1.7\,\mathrm{mA}$. (b) Rectification voltage measured in Pb strip from the opposite sides with $f = 43\,\mathrm{MHz}$, $H = 10\,\mathrm{G}$, and $I_{AC} = 1\,\mathrm{mA}$.

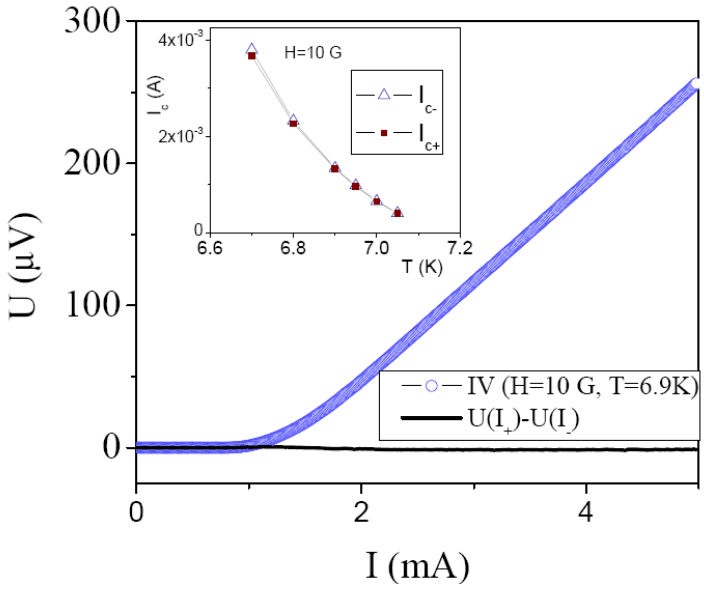

Figure 3.5: Analysis of the asymmetry of typical I-V characteristic on plain Pb sample by summing voltage for the left and right current branches. The inset compares critical currents for the positive and negative branches of the I-V curves close to T_C.

the rectifier is determined by the applied magnetic field and remains nearly constant. For frequencies above a few MHz we found an essential similarity in the DC voltages measured at the opposite sides of the strips when, as for the low frequency data, the measurements were done by moving clockwise (see Fig. 3.4b).

We discard a possible rectification effect due to asymmetries of I-V characteristics. As shown in Fig. 3.5, by summing left and right branches of the I-V curve, does not exceed 3%. The inset in Fig. 3.5 confirms this quantifying of the anisotropy by comparing critical currents determined with a 10 μV criterion for the positive and negative branches of the I-V curves. The origin of this rather small anisotropy could be related to unavoidable bulk pinning anisotropy and/or defect induced [136] [137] difference between surface barriers for the left and right sides of the superconducting strip. This anisotropy, hardly noticeable from the I-V curves, is sufficient to account for the observed low frequency DC voltage and its 1D symmetry.

3.3.2 Plain Nb films

Cross shape

This section shows the results on the Nb plain film with cross configuration. As in the previous experiments, a permanent magnetic field was applied perpendicular to

the film surface, and an AC drive current was applied in the direction parallel to the film plane. With the four voltage contacts which may be seen in the scheme of panel (a) in Fig. 3.1, the permanent voltages could be measured between points on lines both parallel and transverse to the current (longitudinal and transverse voltages).

The rectification at high frequencies proved to be a very intricate phenomenon. In order to have as much information about it as possible, the dependence of the voltages on the drive current intensity I_{AC} was studied by using several currents from 0 to 2 mA, as well as the dependence on the frequency of the AC current. The measurements have been performed in a wide temperature range below the superconducting phase transition. The temperature was varied in steps of 50m K. The effects of reversing the applied magnetic field and of changing its magnitude were also studied. Finally, the voltage drop along a closed contour on the film plane was measured.

The main features of the MHz range rectification are shown in Figs. 3.6 and 3.7. To control that we are studying effects specific for the superconducting phase, the DC resistance of the sample was measured through the normal-superconducting transition with the same set of external parameters as in a measurement of the rectification voltage. This could be done thanks to the cross shape geometry with two perpendicular current probes. A DC current of 1 mA is superimposed in perpendicular direction to the AC current. The voltage between contacts U_2 and U_3 are measured with both polarities of the DC current, with the aim of compensating possible thermoelectric effects.

The difference between these two voltages is used to calculate the DC resistance of the sample in the presence of the AC current and of the applied magnetic field. The DC current resistance is presented on the right axis of Fig. 3.6a. It may be noted that the superconducting resistive transition is located at the same temperature (8.35 K) where the rectified voltages cease to appear. This proves that the rectified voltages are specific of the superconducting phase.

Figure 3.6a represents the voltage measured between contacts U_2 and U_3 (i.e. in the direction perpendicular to the applied AC current) as a function of temperature, and for two applied magnetic fields of the same magnitude (100 G) and opposite directions. Each curve shows several peaks and sign inversions of the voltage in the temperature range from 5 K up to T_C. The measurements show a highly reproducible temperature dependence. The measured rectified voltage (U_{DC}) was independent of the magnetic history of the sample. Only far below T_C a weak history dependence of the strongly reduced DC voltage was found. It may be noted that the change in sign of the applied magnetic field leads, in general, to a change of sign of the rectified voltage, with approximately the same absolute value, especially not far from T_C. When the magnetic field is close to zero (within the precision of about 1 G, determined by the magnetic field trapped in the magnet and the resolution of the magnet current supply), the representative DC signals drop by more than one

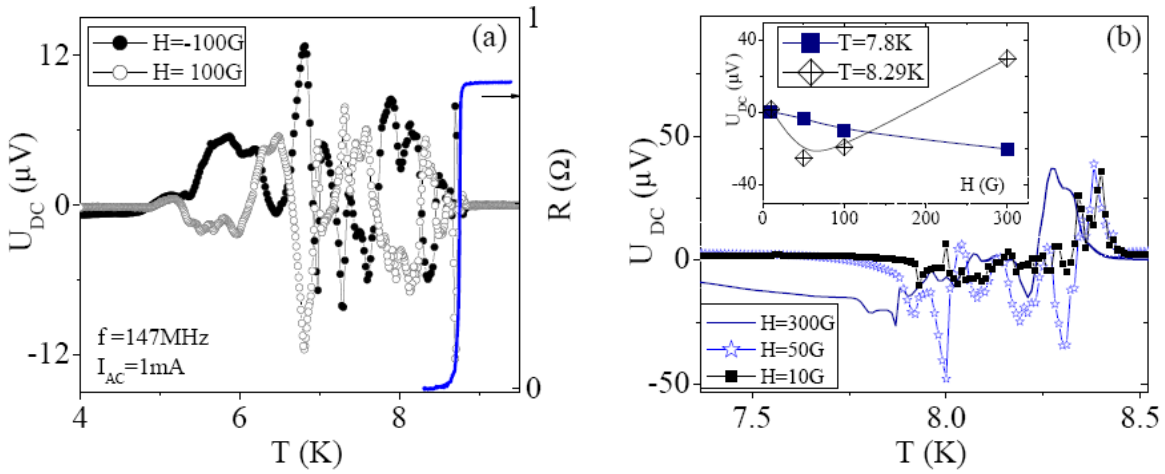

Figure 3.6: (a) Measured DC voltage (left axis) transversal to the applied AC current, as a function of temperature, with two applied magnetic fields of opposite polarity (±100 G). The AC current amplitude was $I_{AC} = 1\,\text{mA}$ and its frequency $f = 147\,\text{MHz}$. To demonstrate that the rectification is a specific feature of the superconducting phase figure shows the temperature dependence of the DC resistance (right axis) through the superconducting transition. The resistance was measured between U_2 and U_3 with a DC current $I = 1\,\text{mA}$ perpendicular to the same applied AC current and in the presence of the same magnetic field of 100 G. (b) Temperature dependences of the rectified longitudinal DC voltage with different applied perpendicular magnetic fields from 10 G to 300 G. The AC current intensity was$I_{AC} = 1.17\,\text{mA}$ and its frequency $f = 43\,\text{MHz}$. The inset shows the field dependence of the rectified voltage (U_{DC}) at two different temperatures.

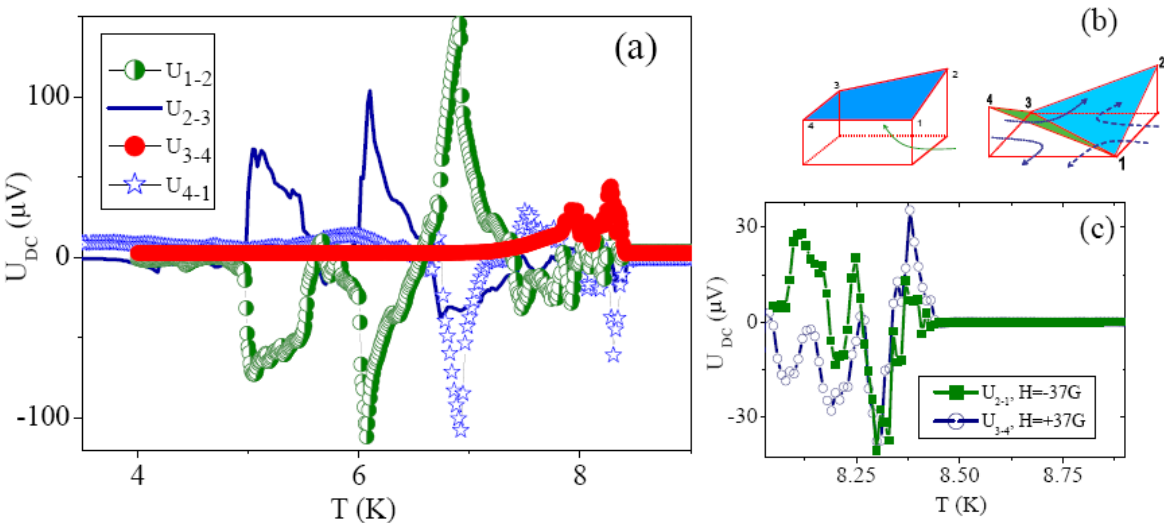

Figure 3.7: Temperature dependence of the rectified voltage (U_{DC}) in four pairs of contacts around the cross area (U_{1-2}, U_{2-3}, U_{3-4} and U_{4-1}). $H = 100\,\mathrm{G}$, $I_{AC} = 1.2\,\mathrm{mA}$, $f = 43\,\mathrm{MHz}$. (b) The electric potential profiles around the cross area are schematically sketched for temperatures close to T_C ($T \approx 8\,\mathrm{K}$, right sketch) and far below T_C (left sketch). The dominant vortex flows in each situation are shown by arrows. (c) The longitudinal rectified voltage measured at opposite sides of the cross area and in magnetic fields of opposite polarity.

order of magnitude in comparison with the data obtained at 100 G.

In Fig. 3.6b the temperature dependences of the voltage measured in the longitudinal direction (i.e. parallel to the AC current) for three different magnetic fields of the same sign are shown. It is seen that the voltage at a given temperature may be a non-monotonous function of the magnetic field. This is illustrated in the inset of the figure, where the rectified voltage at two selected temperatures is plotted as a function of the applied magnetic field. These temperatures correspond to the highest negative peak (7.80 K) and highest positive peak (8.29 K) of rectified voltage under a field of 300 G. At 7.80 K, the signal is very sensitive to the field and its dependence on the field is fairly monotonous, while at 8.29 K, this dependence is non-monotonous and the signal even changes sign when increasing the field.

Figure 3.7 shows the temperature dependence of the rectified voltages measured at the four contacts at the corners of the cross (see Fig. 3.1a). The measurements were performed successively in neighboring pairs of contacts in anti-clockwise sense. It may be noted that close to T_C the DC voltage has nearly the same absolute values but different signs for opposite sides of the cross area. The situation is different at temperatures $T < 0.8T_C$ where rectification is dominant on two neighboring sides of the cross area. Since the voltages between different pairs of contacts were measured

in different experimental runs, we have checked that for a given temperature the sum of the four voltages is zero, which assures that there is a net zero flow of vortices through the entire contour of the cross area.

Figure 3.7c shows another symmetry property of the phenomenon close to T_C: the electric fields at opposite sides of the cross area interchange when inverting the magnetic field direction. It was found that the above data are reproducible for two identical plain samples in the temperature region close to T_C. Further below T_C, the permanent voltage showed some differences between both samples. This seems to indicate that in the latter case the effect is mainly due to uncontrolled asymmetry of the borders or to an inhomogeneous density of pinning centres. These two samples were patterned for the measuring contacts in two different zones of the same film.

In addition, we studied the dependence of the rectified voltage on the intensity and frequency of the AC current and on temperature. These dependences proved to be fairly similar for longitudinal and transverse rectified voltages. For this reason we present some data for transverse voltages and some other for longitudinal ones. In Fig. 3.8, the dependence of the transverse rectified voltage U_{DC} on temperature and AC current intensity is displayed in a three dimensional (3D) contour plot. In this case, the drive frequency is 50 MHz and the applied magnetic field is 100 G.

One may see that the temperature dependence of the voltage is very complex, with several changes of sign. Besides, the rectification effect is not limited to the close proximity of T_C, but is observed down to $T_C/2$, with current intensities above 1 mA. The magnitude of the rectified voltage reaches values which are more than an order of magnitude higher than those reported previously [74] for comparable AC currents and magnetic fields but for frequencies in the low kHz range. The maximum magnitude is also much higher than the rectified voltages measured in the same MHz frequency range in the Nb nanostructured samples which we show below. The magnitude of the voltage maxima scales with the AC current intensity and their positions shift in temperature with the change of current. It may be noted that this shift is not related to any heating effect, because it is at least one order of magnitude larger than the reduction of T_C induced by the AC current. This reduction of T_C may be observed in the figure as a smooth decrease of the highest value of temperature where rectification shows up when increasing the drive current (the upper "island" on the map). With $I_{AC} = 2.1$ mA, the data were obtained both decreasing and increasing the temperature, with no noticeable difference.

Next, I show data on the dependence of the longitudinal rectified voltage on the frequency of AC current and on temperature keeping constant the applied magnetic field (100 G) and the current (1.2 mA) are shown.

Figure 3.9 shows the temperature dependence of the rectified voltage at different drive frequencies in the range between 9.9 kHz and 147 MHz. Note that panels (a) and (b) have different vertical scales in order to highlight the change in magnitude of maximum rectified voltages. For the lowest frequency, i.e. 9.9 kHz, the generated

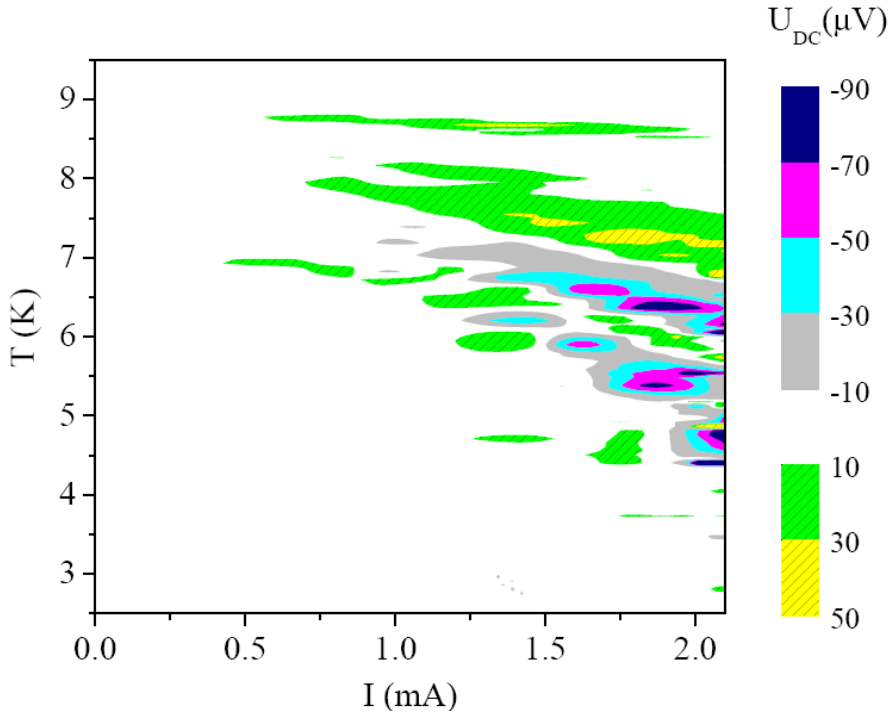

Figure 3.8: 3D contour plot of the dependence of the transverse rectified DC voltage (U_{2-3}) on temperature and AC current intensity, with $f = 50\,\mathrm{MHz}$ and $H = 100\,\mathrm{G}$. The increase of the maximum magnitude of the (positive or negative) rectified voltage with increasing AC current intensity is clearly observed. Some displacement of the maximum to lower temperatures with increasing AC current is also visible.

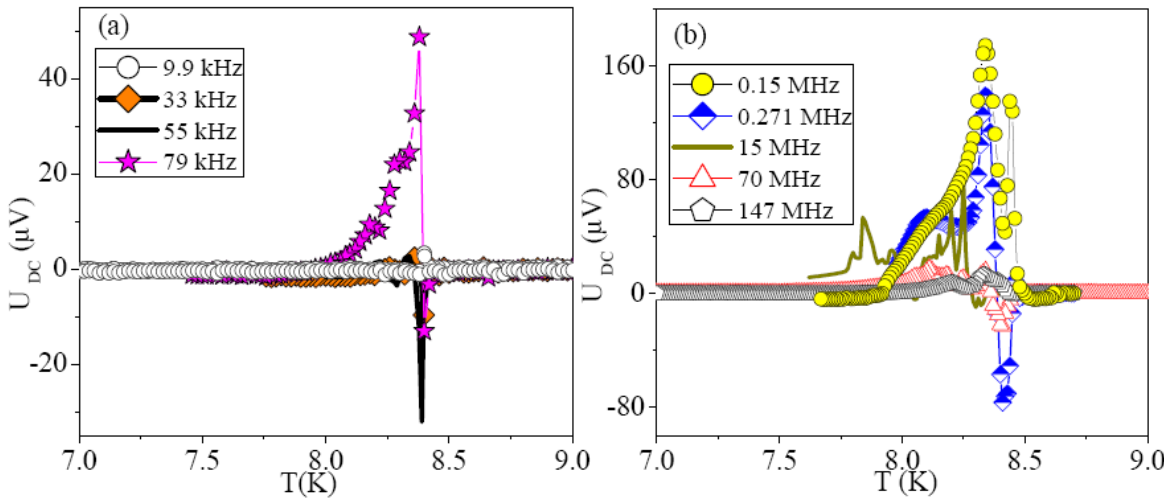

Figure 3.9: Dependence of the rectified longitudinal (U_{1-2}) DC voltage on the frequency of the AC current and on temperature.(a) Measured frequencies in the kHz regime from 9.9 kHz to 79 kHz. (b) Measured frequencies in the MHz regime from 0.15 MHz to 147 MHz. In both regimes $I_{AC} = 1.2\,\mathrm{mA}$ and $H = 100\,\mathrm{G}$. Note the different vertical scales.

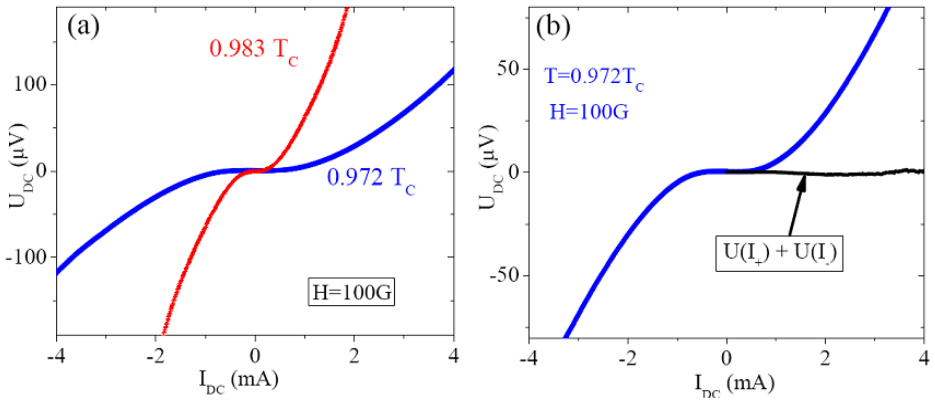

Figure 3.10: (a) I-V curves measured in a Nb plain film in cross configuration with H = 100 G, at two different temperatures close to T_C. (b) Analysis of the asymmetry of the I-V characteristic for one of the curves from panel (a) (for T/ T_C = 0.972): the solid line plots the sum of the left and right branches U(I+)+U(I-) of the I-V characteristic, and shows that the asymmetry is nearly negligible, below 3%.

DC voltage appears only close to the critical temperature, and does not exceed a few μV. On the other hand, for AC drives close to and in the MHz range, we observe a dramatic enhancement of the measured DC voltage, accompanied by a very non-monotonous dependence on temperature with a noticeable effect quite far below the critical temperature.

One could think that the rectification effects are caused by an asymmetry of the critical current magnitudes when the polarity of the current is changed, as was reported to be the cause of other rectification phenomena by *Swartz* et al. [116]. Indeed, the superconducting films under study are almost perfectly symmetric and present no substantial difference between their DC critical currents with a change of their polarity, within an error of less than 3%. Figure 3.10a shows the electron transport characteristics of the Nb cross shaped film measured in the DC regime near T_C.

The data show clearly that the I-V curves are almost perfectly symmetric, and that the rectified voltage due to the DC current asymmetry for currents up to 2 mA is below some few μV. This demonstrated by the horizontal curve in Fig. 3.10b, which presents the sum of the left and right branches of the I-V curve for a selected temperature, namely for $T/T_C = 0.972$. In a magnified scale (not shown) it could be observed that the values of the voltage registered by this curve are always within a few μV, being between one or two orders of magnitude smaller than the rectified voltages which we have reported above near and within MHz frequencies, and with similar current intensities.

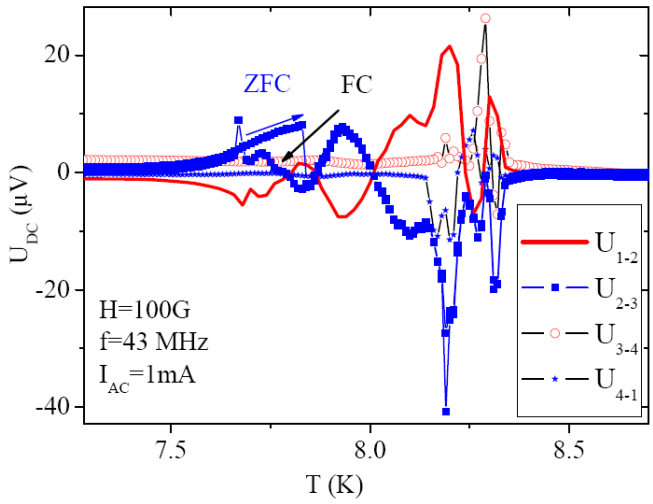

Figure 3.11: Temperature dependence of the longitudinal (U_{1-2} and U_{3-4}) and transverse (U_{2-3} and U_{4-1}) DC voltage generated in a long Nb strip (40*320 μm^2) with an applied magnetic field of 100 G, a drive AC current of frequency 43 MHz and intensity of 1 mA. The transverse voltage U_{2-3} data corresponds to two measurements carried out with different magnetic history and marked by arrows: field cooled (FC) and zero field cooled (ZFC) conditions.

Strip shape

In order to reveal the dependence of the observed rectification effect on the film shape, we also performed experiments on a similar plain Nb film patterned to a strip.

Figure 3.11 shows the rectified DC voltage as a function of temperature, both in transverse and in longitudinal directions, in a 40 μm wide Nb strip, with a distance between longitudinal contacts of 320 μm. The geometry of the voltage contacts is shown in Fig. 3.1b.

Some features of the phenomenon are similar in the cross shape films and in the strip ones. The voltages between the pairs of contacts on opposite longitudinal sides of the film (U_{1-2} and U_{3-4}) and on opposite transverse probes (U_{4-1} and U_{2-3}) have opposite signs just close to the transition and comparable magnitudes. However, at lower temperatures (for example at 7.8 K) there is a strong asymmetry between the opposite borders: $U_{1-2} << U_{3-4}$ and $U_{4-1} << U_{2-3}$.

An important new information can be seen in Fig. 3.12, where I show the temperature dependence of the rectified voltages between pairs of nearby (U_5, U_1; l = 40 μm) and distant (U_1, U_2; l = 320 μm) contacts at the same border of the strip is shown. Close to the phase transition $U_{5-1} \approx U_{1-2}$. This is already significant:

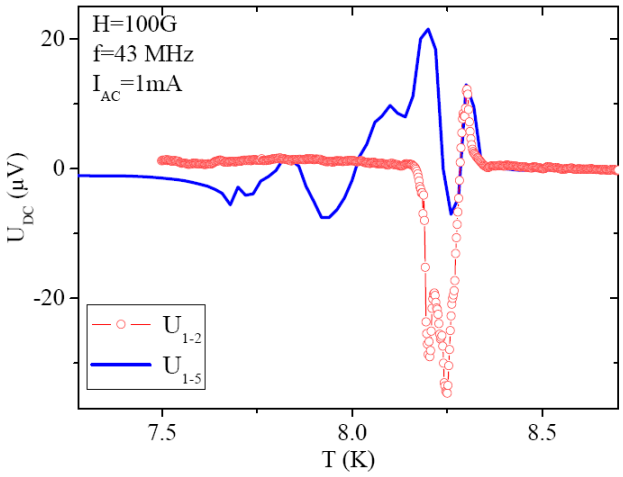

Figure 3.12: Dependence of the longitudinal rectified DC voltage of the Nb strip on the distance between contacts and on temperature. U_{1-5} (l= 40 μm) and U_{1-2} (8l) measured in the same border of the strip with an applied magnetic field of 100 G, an AC current intensity of 1 mA and drive frequency of 43 MHz.

the distance between the contacts U_1 and U_2 is 8 times the distance between the contacts U_5 and U_1, i.e. the permanent electric field is strongly inhomogeneous along the border. At lower temperatures U_{5-1} and U_{1-2} have opposite signs, what implies that the electric field is not only inhomogeneous but even can change its sign. I shall return to this observation when discussing the experimental data.One

can also examine the influence of magnetic history on these data, which has proved to be negligible, except at the lowest temperatures where rectification is observed. Indeed, the data in Fig. 3.11 corresponding to the transverse geometry consist of two curves measured in the same conditions, except that one is taken on heating after zero field cooling (ZFC), and then applying the external magnetic field, and the other one with the temperature decreasing under field cooled conditions (FC). The difference between both curves is very small, except in the low temperature region highlighted by the arrows.

In the whole frequency range studied, both the longitudinal and transverse DC voltages are nearly antisymmetric in values with respect to the polarity of the magnetic field. As an example, Fig. 3.13 shows the rectified voltage measured in longitudinal configuration (U_{1-2}) for both polarities of a magnetic field value of 17 G. It was also found that the generated DC voltage depends nonlinearly on the amplitude of the AC drive.

Above (see Fig. 3.10), in the case of cross shaped samples, the critical current anisotropy was negligible to explain the rectifying effect. Here it is shown another

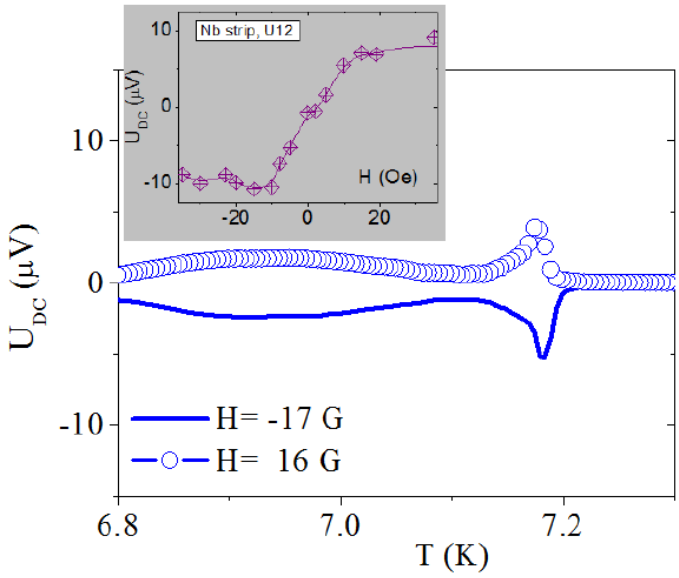

Figure 3.13: Longitudinal dc voltage measured with f =147 MHz, I_{AC}=0.46 mA for two nearly opposite magnetic fields. The upper inset shows dependence rectification voltage U_{1-2} vs. magnetic field for Nb strip when measured with I_{AC}=1.3 mA, and f =43 MHz and T/T_C=0.99.

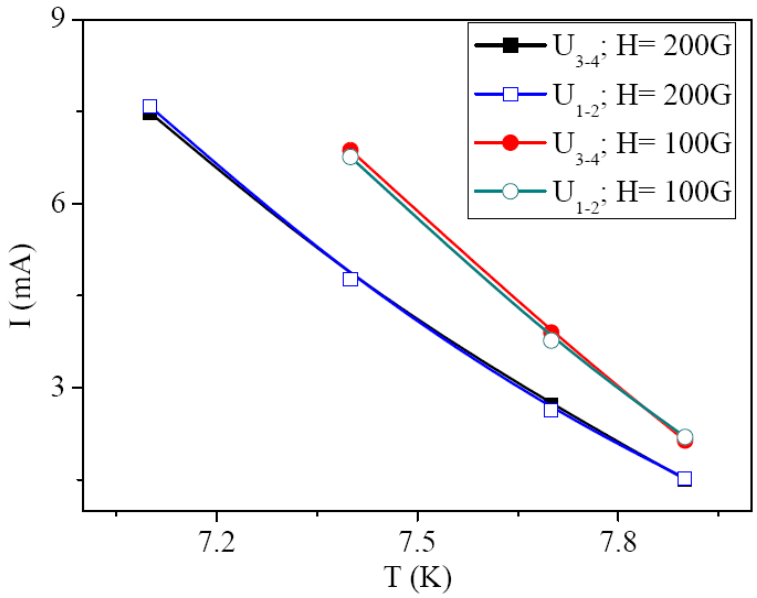

Figure 3.14: Critical current vs. temperature measured at opposite longitudinal sides of the superconducting Nb strip, with the criterion of a critical voltage of 10 μV. The measurements have been performed with applied magnetic fields of 100 G and 200 G. It may be seen that for each applied field the critical currents measured at opposite sides of the strip are practically equal.

method to evaluate the possible anisotropy of the critical current, by comparing the critical currents measured at opposite sides of the strip. It may be seen in Fig. 3.14 that the measured currents practically coincide, for applied fields of 100 G and 200 G.

3.4 Vortex rectification effects in nanostructured Pb and Nb films

3.4.1 Nanostructured Pb film

We have also looked for high frequency rectification in artificially nanostructured Pb films with a square periodic pinning array of circular holes (antidots) with diameter of 0.6 nm and period 1.5 μm. The idea is to study how the enhanced vortex pinning can influence the effect studied in plain films.

The stronger vortex pinning increases the critical current [69] J_C and lowers the rectified DC voltage in about an order of magnitude. Moreover, and most

interesting, at temperatures far below T_C the rectified DC voltage changes polarity not only when changing the direction of the magnetic field as in plain films, but also when the intensity of the magnetic field crosses the so-called matching fields. In nanostructured superconducting films one defines the matching field H_1 as the applied magnetic field which produces a total flux through the sample equal to the flux of one flux quantum Φ_0 in each pinning centre. It is assumed that when the applied field is equal to the matching field there is a single vortex pinned in each artificial pinning centre. The integer multiples of H_1 are called second, third matching fields, and so on.

In Fig. 3.15 data for the nanostructured Pb film under four applied fields in the proximity of H_1 (9.2 G in this sample [115]) are shown. The drive frequency is 147 MHz. It may be seen that only the DC voltage sharp peak near 5.5 K is found to invert its sign when the magnetic field intensity crosses the first matching field.

In the inset of Fig. 3.15, the magnitude of this peak as a function of the applied field for H = - $H_{1/2}$ to above H_3 is plotted. It may be seen that the low temperature contribution to the rectified voltage is clearly non-monotonous above H_1 and shows an oscillating behavior at least up to n=3. For the smallest fields the DC voltage is an antisymmetric function of the magnetic field for the whole temperature range (see behavior near H = 0 G in the inset). It seems interesting to note that the permanent voltage inverts sign not only when crossing the integer matching fields but also near the rational field $H_{1/2}$ (i.e. near the magnetic field corresponding to an average half of flux quantum per antidot). In this latter case we conclude that the permanent voltage changes sign when moving from a regime with a dominating "excess of unpinned vortices" for $H < H_{1/2}$, to the regime with a dominating "deficit of unpinned vortices".

3.4.2 Nanostructured Nb film

High frequency rectification effects were also investigated in an artificially nanostructured Nb film with symmetric periodic pinning centres (PPCs), made up of Ni dots.

As we mentioned above, it is well known that in nanostructured films the pinning force is stronger and obviously better controlled than in plain films [132] [69]. The value of the matching field may be calculated by knowing the surface density of pinning centres in the sample. In the case of nanostructured Nb film $H_1 = \Phi_0 /(p \times q) = 103$ G, being p and q the sides of the rectangular unit cell of the Ni dots. This value is in good agreement with the measured value $H_1 = 105$ G [133]. The critical temperature of the sample is $T_C = 8.73$ K.

The nanostructured Nb samples were patterned to the same cross shape as the plain films previously described. As in the case of nanostructured Pb films, the measurements of AC current rectification in nanostructured Nb films reveal at least

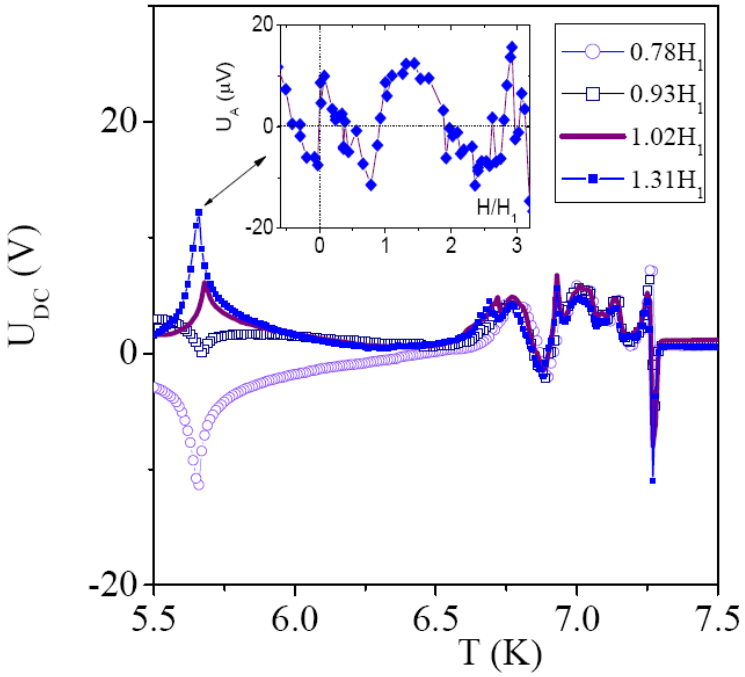

Figure 3.15: Rectified DC voltage U_{2-3} as a function of temperature in a Pb film with an array of holes. The data have been obtained with magnetic fields close to the first matching field $H_1 = 9.2\,G$, with $f = 147\,MHz$ and $I_{AC} = 0.94\,mA$. The inset shows the dependence of the amplitude of the low temperature sharp peak near 5.5 K, signalled by an arrow, on the magnetic field normalized by the first matching field H_1, when is measured with the same frequency and drive current intensity. The asymmetry of this low temperature anomaly respective to H_n gradually smears out for n >3 (not shown).

two main differences in comparison with plain films. First of all, the magnitude of the rectified DC voltage is lower for the same AC current intensity and frequency, magnitude of the applied magnetic field and temperature. Second, at temperatures far below T_C, the rectified DC voltage changes polarity not only when the magnetic field changes its sign, as in plain films, but also when the magnetic field intensity changes and crosses the matching fields.

As an example, Fig. 3.16a shows the values of high frequency (147 MHz) transverse rectified voltage as a function of temperature for three applied magnetic fields close to H_1.

It may be noted that the form of the curve is very well reproduced for different values of the field, but the rectified voltages change sign when crossing the first matching field. We also find that the maximum magnitude of rectified voltage (around 20 μV) is nearly an order of magnitude smaller than in a plain Nb film with similar geometry and external parameters (Fig. 3.9) showing up to 150 μV of rectified signal. Panel (b) shows similar data as in panel (a), but in this case crossing the second matching field H_2. The influence of crossing the matching field can be identified, but it is weaker than when crossing H_1. In panel (c) the results for fields near and above H_3 are shown. The influence of crossing this third matching field is completely smeared out. However, we note that at high fields the rectification peak is visibly shifted to lower temperatures with increasing field, while the magnitude of the peak does not show a monotonous variation, reaching a maximum in the region of 1000 G.

We have also performed a detailed experimental study, sweeping the field at small intervals with an AC current intensity of 0.94 mA and a drive frequency of 147 MHz. The data have been represented in Fig. 3.17, as 3D contour plots. One clearly observes the vertical lines without DC rectified signal which correspond to zero magnetic field and to the first matching field.

3.5 Discussion

In order to explain the results I will discuss two different models. The first one is based in the microscopic Bean-Livingston (BL) surface barrier for flux penetration. But even in absence of this surface barrier and pinning centers for vortices, superconductors with a non-ellipsoidal shape can exhibit a barrier for flux penetration [138].

3.5.1 The Bean-Livingston barrier model

I start with a discussion of vortex behavior close to the edge of superconducting films which is determined by the BL surface barrier. This is important to help readers to understand the observed rectification effects in restricted geometries.

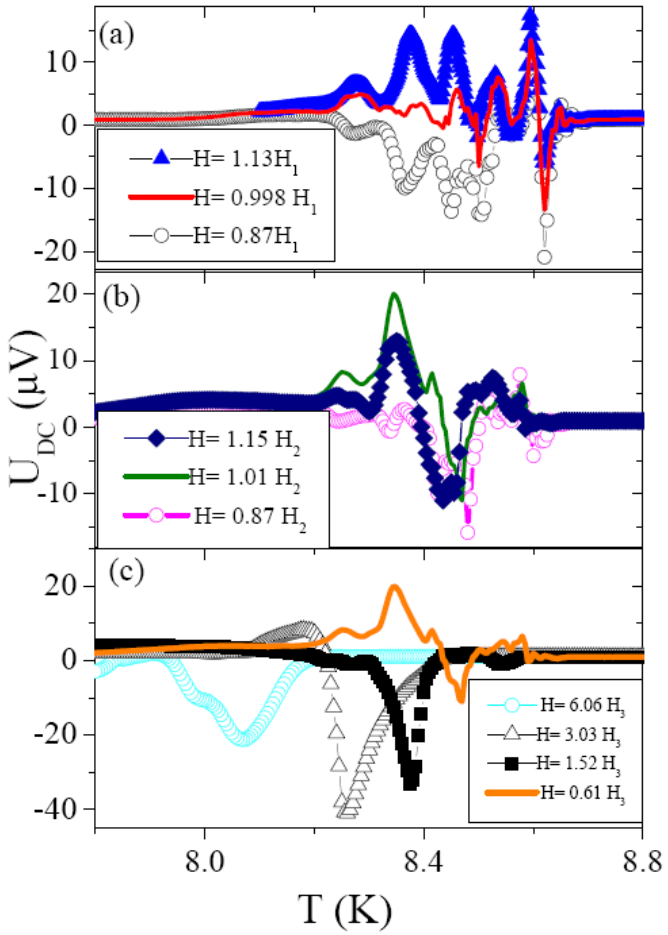

Figure 3.16: Transverse rectified DC voltage U_{2-3} in a nanostructured sample as a function of temperature for several magnetic fields. The data have been obtained with magnetic fields (a) close to the first matching field $H_1 = 105\,G$; (c) to the second matching field $2H_1$; and (d) to the third matching field $3H_1$, in all cases with $f = 147\,MHz$ and $I_{AC} = 0.94\,mA$.

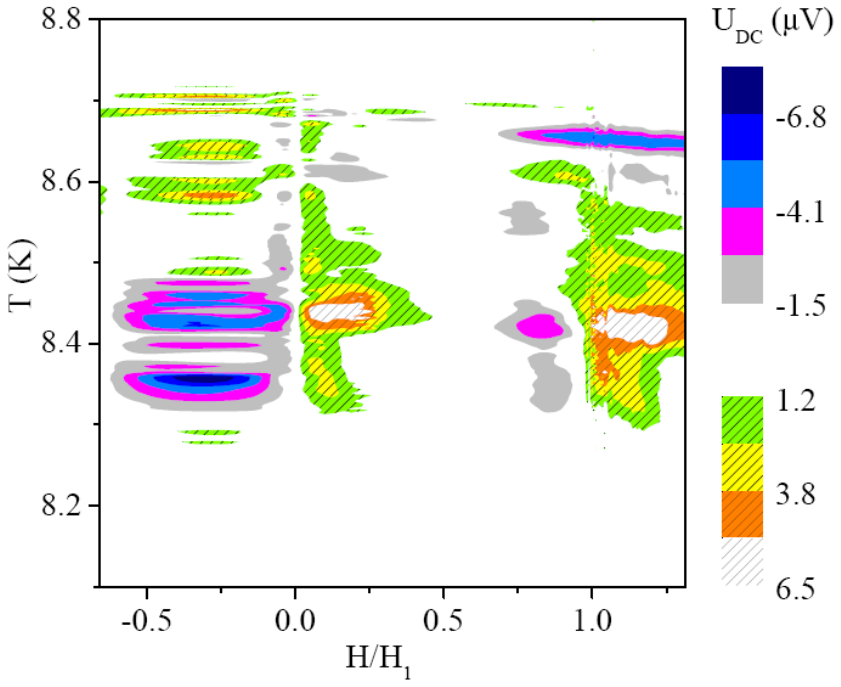

Figure 3.17: 3D contour plot of the transverse rectified DC voltage U_{2-3} in a nanostructured sample as a function of temperature and applied magnetic field, measured with $I_{AC} = 0.94\,\mathrm{mA}$ and $f = 147\,\mathrm{MHz}$. The matching field H_1 is 105 G. It may be seen that the rectification effects are quite similar, when crossing zero field from negative to positive fields, to the effects observed when crossing the matching field.

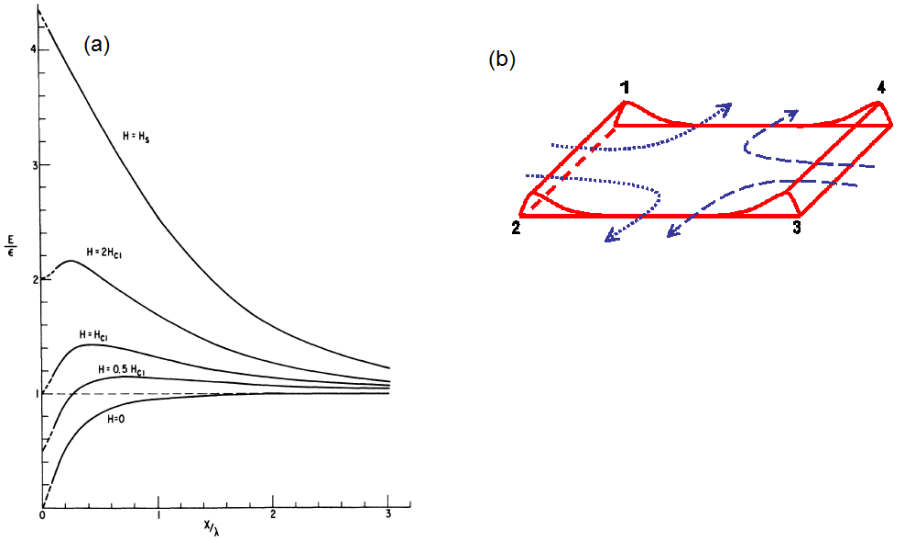

Figure 3.18: (a) Energy of the flux quanta E vs. distance from the surface x. at various applied magnetic fields. ϵ corresponds to the energy per unit of length of a single vortex, H_{C1} is the first critical field and λ is the penetration depth. Figure taken form [139]. (b) The two oppositely directed asymmetric BL barriers. Arrows indicate the vortex flow in the sample.

In the 1960s, Bean and Livingston studied the energy profile near the edge barrier in a type-II superconducting sample [139]. They studied the forces which the vortices in a semi-infinite type-II superconductor feel near the surface. The line energy of the flux quanta near the surface is as Fig. 3.18 shows.

This energy barrier against flux motion into or out the sample must exist at low fields.

In order to explain our experimental results, we can suppose that the superconducting films have two oppositely directed BL barriers, as Fig. 3.18b shows. At low drive frequencies (f $\leq$ 10 kHz), when the vortex travel distance $L = v \cdot 1/f \sim 500\,\mu$m is much larger than the transverse dimensions of the strip (d), during each half-period the vortex motion "feels" negligible bulk pinning anisotropy, as well as some small unavoidable difference in the symmetrically reflected shape of the two left and right BL barrier profiles. Such periodic vortex motion with large amplitude provides the 1D rectification, as indeed experimentally observed (see Fig. 3.3). At higher frequencies ($f \approx 100$ kHz), the vortex travel distance is reduced and becomes comparable to the width of the strip, that is $L \approx d$. Here, the vortex velocity is taken as $v = 50$ m/ s, which was estimated from the measured DC voltages, H=10 G and d= 100 μm for Pb or 40 μm for Nb. If the typical BL barrier width was taken to be about $b \sim 1 - 5\,\mu$m, then at the drive frequencies of the order of $v/b \sim 10 - 50$ MHz

the two opposite transversal vortex flow patterns would be generated during each of the half-cycles of the AC drive inside the superconducting strip due to edge ratchets (see dashed and dotted arrows in Fig. 3.7 and 3.18). This would result in an excess vortex density closer to the center of the superconducting strip, thus creating two opposite longitudinal vortex flows, in accordance with the observed 2D rectification voltage profile. The earlier arguments imply that the DC voltage between the same lateral contacts should change the sign if the direction of the permanent field is changed. This case is shown in Fig. 3.13 where not far below T_C the polarity of the DC voltage is controlled by the polarity of the applied magnetic field.

Another natural conclusion is that the DC electric fields at the opposite sides of the strip are of the same value and have opposite signs. Near T_C the signs are, indeed, opposite but their absolute values are not equal. Therefore, at high AC drive frequencies rectification has a local character determined by the combined effect of the small anisotropic vortex pinning and the vortex rectification by the two non-ideal BL barriers. The multiple sign inversion of the rectified voltage can be explained qualitatively by the presence of defects and impurities in a real system. It has been shown [140] that relaxation times due to vortex entry/exit through BL barriers are not only very different, but also show qualitatively different temperature dependences. Presence of defects in the real superconducting film produces a spatial variation of the BL barrier along the strip [136] [141], naturally explaining multiple sign inversions for the longitudinal DC voltage as well as the linked to it transversal one.

3.5.2 Meissner currents induced geometric barrier model

Surface barriers which experience vortices in superconductors were introduced to explain experiments in which relatively large critical currents were observed with a very weak bulk pinning. Initially only BL surface barrier was considered. As was discussed in the previous paragraph, vortices can experience BL barrier asymmetry during their exit and entry in the superconducting structure. For relatively high frequency AC currents in the presence of magnetic field this may induced DC rectification of the opposite sign on the opposite sides of the superconductor. The BL barrier model employed has some drawback because barrier shown in Fig. 3.18 was calculated for the external magnetic field being parallel to the surface of semi-infinite superconductor. Therefore, below we discuss an alternative model which explains the observed high frequency AC current rectification in the presence of magnetic field being perpendicular to the superconducting film plane and AC current as a phenomenon produced by the influence of Meissner currents induced geometrical barrier. As we shall see, this new surface barrier, schematically shown in Fig. 3.19, which may exist in addition to the BL barrier, also explains the main experimental results.

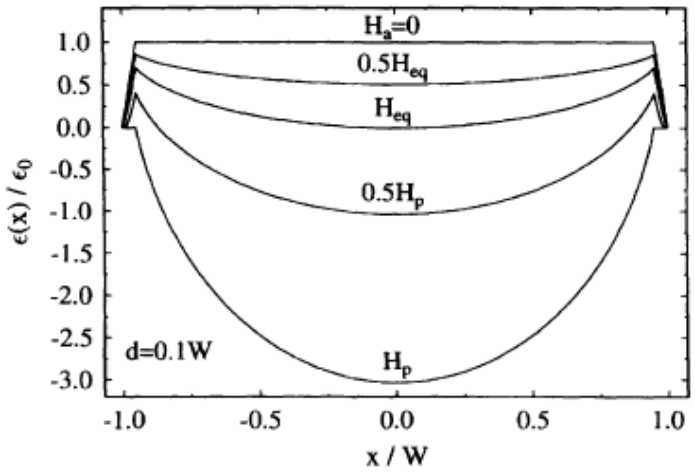

Figure 3.19: Vortex potential in a superconducting film of width 2W and thickness d at various perpendicular magnetic fields. The penetration field $Hp \sim H_{C1}\sqrt{d/W}$, being H_{C1} the first critical field.

To discuss the results within this model, one may consider first a superconducting strip in a magnetic field perpendicular to its surface, but without transport current. The equilibrium vortex lattice is known to occupy not all the sample but to leave free a region close to its borders (see upper sketch in Fig. 3.20).

This is due to the Meissner currents arising in response to an applied magnetic field and responsible of the surface barriers. This situation was discussed in the case of a semi-infinite type-II superconductor in contact with free space in the sixties and early seventies [139] [143] as has been described in previous paragraphs. More recently, it has been studied in other geometries, and in the case of thin films in a perpendicular magnetic field [137] [142] [144]. When a transport current is applied, the vortices are pushed to one side (see lower sketch in Fig. 3.20). This shrinks one of the regions free of vortices and expands the other one [145] [146]. With a sufficiently strong current, the vortices begin to leave the sample at one border while the barrier at the other border may remain hampering the entrance of the vortices through it. While the movement occurs mainly close to one border, an electric field exists close to this border and not close to the opposite one, until the vortex lattice achieves a new equilibrium or begins to move as a whole. If the direction of the current changes, the vortices leave the sample at the opposite border and an electric field of opposite sign develops close to this border. Therefore, in an alternating current an electric field in one direction arises during a first half period close to one border and of opposite sign close to the other border during the second half-period. This explains the distribution of DC electric fields which has been observed close to T_C. However,

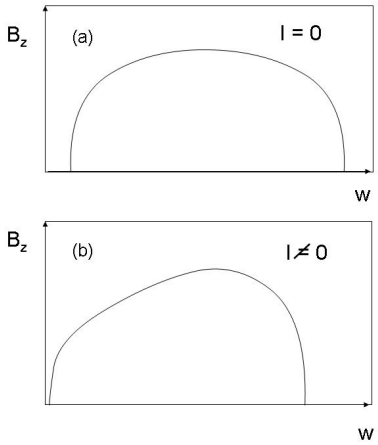

Figure 3.20: Sketch showing the equilibrium distribution of the vortex density in a superconducting film, of width w, calculated in Refs. [142] [143], , in the case (a) of borders without an applied DC electric current, and (b) with current. See text for more explanations

this description is clearly too simplified. Imagine a very long strip with electric fields of opposite signs at the opposite lateral borders of the strip. This is non-sustainable. Indeed, let for some value of the longitudinal coordinate, the potential difference between the opposite lateral borders be zero. Then moving off from this point in either direction along the strip we should observe an increase of the potential difference between the borders and this increase is non-limited if the strip is not limited in its length. This is a clear nonsense and one should admit that there should be a characteristic length for change in sign of the field at a given lateral boundary when one moves along this boundary. This seems to be confirmed by the data for the strip, as may be seen in Fig. 3.12 and in the discussion of this figure. Admitting the possibility of opposite signs of the permanent field at the same lateral border and the conclusions made from Fig. 3.17 one has to admit that a part of the vortex matter moves in phase with the external driving field and another part is moving in antiphase. This would mean that the vortex system decomposes in parts which are moving in different ways. Unfortunately, we are unable to say anything definite about the main features of this decomposition and the characteristic length of the parts which are expected, of course, to be dependent on temperature. Experiments on a long strip with many contacts along its lateral borders could be revealing in this aspect. However, such samples are unavailable for us. We hope that these reported data will stimulate further investigations in this direction. It is natural to relate the frequency dependence of the observed effect to values of characteristic times for the relaxation of the vortex and current distributions when the external

current is changing. It is known that in the presence of both external magnetic field and external current this relaxation is a fairly complicated phenomenon [147]. To have a very rough idea about possible orders of magnitude of the relaxation times we refer to *Gurevich* et al. [148] who argued that in systems with vortices the duration of the first stage of relaxation of field and current distribution is a macroscopic quantity which can be expressed via directly measured parameters. Despite they considered a different geometry (slab of width a in parallel magnetic field and relaxation after the magnetic field change), nevertheless, it makes sense to try to apply their estimations of the characteristic time, $\tau \approx \mu_0 \left(\partial j/\partial E\right) a^2$, to our case. Indeed this time has, in any case, the physical meaning of the characteristic time of diffusion of magnetic flux across the sample. If one takes $\partial j/\partial E$ as about its value in the normal phase and a^2 as about the cross area, one gets $\tau \approx 10^{-7}$ - 10^{-8} s. This is in a reasonable agreement with the frequencies for which the effect becomes clearly observable. Another rough estimation of the optimal frequencies for observation of the effect can be obtained from the estimation of the propagation time of the signal associated with the deformation of the vortex lattice. The velocity of this propagation for a vortex lattice in a thin film in perpendicular magnetic field has been calculated by *Fetter and Hohenberg* [149] as

$$v \approx \left(\frac{eB}{mc}\right) \sqrt{q\Lambda \left(\pi n\right)} \quad ,$$

where e, m are the electronic charge and mass; c is the light velocity (Gaussian units are used); Λ is the effective penetration length for films, $\Lambda = \lambda^2/d$, where λ is the penetration length for a bulk sample and d is the film thickness; q is the dominant wave vector of the perturbation, n is the vortex density, $n = B/\Phi_0$. It seems probable that the characteristic spatial extension of the "signal" is of order of Λ. This means that $q\Lambda \approx 1$, i.e., the velocity depends on the magnetic induction (vortex density) only and can be estimated approximately. Since the width of the film is approximately the retardation time, which corresponds to the optimum frequency range of observation of the effect. From this point of view, the effect should be observed at lower frequencies for wider films. We could not check this prediction but it is worthwhile mentioning that for a 4 mm wide Pb film some rectification effect (characterized as "puzzling" by the authors [150]) at 100 kHz frequency and for magnetic fields of several k G has been observed. The very general and clearly tentative ideas exposed above help to understand why we observed a much weaker signal in nanostructured films than in plain ones. The strong pinning of the vortices should hamper the above described decomposition, decreasing the movement of the vortex matter. It is remarkable that at matching fields, when this pinning is especially strong, the rectified signal is almost as weak as at zero field.

3.6 Conclusions

In conclusion, in this chapter I demonstrate the existence of a new kind of DC voltage observed in samples without non-symmetric pinning centers and under a harmonic, i.e. time-symmetric AC drive [151] [152]. In the low frequency (kHz) range the rectified DC voltage presents 1D symmetry. This rectification is most important in the MHz frequency range, where the rectification has 2D symmetry. The new characteristics of the rectification are the following: first, the DC component of the electric field is completely different close to the opposite transverse and longitudinal borders of the sample, relative to the current direction. Second, its values are much higher in plain samples than in those with artificial pinning centers for similar current densities. Third, the DC voltages exhibit very complicated temperature dependence. Fourth, the frequency dependence of the voltages is non-monotonous and there is a frequency of maximal effect at a given applied magnetic field. Fifth, the dependence of the effect on the applied magnetic field is also non-monotonous.

We discussed two simple alternative models which seems to explain the main experimental features (with exception of multiple DC voltage sign inversions) of the high frequency AC current rectification in the presence of magnetic field being perpendicular to the superconducting film plane. The first is asymmetric Bean Livingston barrier model and the second is Meissner currents induced geometrical barrier model.

Chapter 4

Magnetization dynamics in arrays of Permalloy dots

4.1 Introduction

During the last years a large amount of investigations have been performed on patterned submicrometer arrays of magnetic elements with different shapes such as arrays of squares [153], rectangles [154], ellipses [155] [156] and triangles [157]. These systems have attracted much interest from the theoretical point of view, because they present a model system to study low dimensional magnetic phenomena, as well as from the experimental point of view due to possible applications in magnetic storage devices. The study of spin waves (SWs) in these systems is a powerful method for probing the dynamic properties of magnetic media in general, and those of laterally patterned magnetic structures in particular. When the size of the element becomes comparable to the wavelength of a SW under investigation, quantization effects appear, which lead to dramatic changes in the SW spectrum and the SW density of states. Of special interest is the circular geometry, where no dipolar energy contribution from the edge may appear in the structure. Theoretical studies of circular dots with a vortex structure [44], saturated in-plane [158] and out-of-plane [159] predict multiresonance eigenmodes. From the experimental point of view it is extremely difficult to study a single magnetic element, because it challenges the sensitivity of the experimental set-up. To avoid this problem the elements under investigation are usually assembled in arrays of magnetic elements which permit the investigation of interdot interactions [160] and collective excitations [161]. Although different experimental techniques have been used to probe high frequency magnetization dynamics including Brillouin light scattering (BLS) [162] and conventional ferromagnetic resonance (FMR) [163], techniques based on the frequency domain, where the frequency of an external bias field is swept, are very convenient for systems with a non-uniform magnetic configuration. The vector

network analyzer (VNA) technique is a promising tool for magnetization dynamics detection in these nanostructures. *Novosad* et al. [48] have reported the study of the magnetic vortex resonance in Permalloy dots patterned on a coplanar wave guide, and observing the vortex translational mode. More recently, *Neudecker* et al. [164] [165] have reported multiresonance modes in Permalloy dots by using the VNA technique, observing vortex state resonances modes (radial and azimuthal modes), edge resonance modes and saturated in-plane resonance modes.

This chapter is devoted to the investigation of magnetization dynamics, possible dipolar interaction between dots and possible sources of magnetic anisotropies in arrays of circular Permalloy dots of 50 nm thickness and 500 nm radius with different interdot distances at room temperature in two different regimes: in-plane saturated state and vortex state. As will be described in the following paragraphs, azimuthal modes with a large splitting have been observed when the vortices are present in the dots close to the dot center. On the other hand, the uniform resonance mode (Kittel mode) and a second mode, that has been interpreted as magnetostatic backward volume SW mode, have been observed for in-plane saturated state [166].

4.2 Characterization of arrays of magnetic dots

4.2.1 Sample growth

The technology for the fabrication of high-quality patterned magnetic structures with lateral extensions on the micrometer, submicrometer, and nanometer scale has been improved during the past years. Lateral magnetic structures are fabricated using lithographic patterning procedures. The patterning processes more commonly used are electron beam lithography (EBL) [167], X-ray lithography (XRL) [168] and laser interference lithography (LBL) [169]. The studied samples were grown by using the EBL technique. The main fabrication steps of EBL are the film deposition, the electron beam exposure, etching, and then the sample growth. The arrays of polycrystalline Permalloy dots have been fabricated on silicon substrates using lift-off techniques. Fig. 4.1 shows the fabrication steps carried out. A double layered resist spin coating on top of a silicon substrate was exposed to a focused electron beam (a). The bottom layer is more sensitive to the electron beam than the top layer, therefore, the bottom layer forms an undercut profile when developed (b). After this step, the magnetic film can be deposited on a water-cooled substrate from a Permalloy target with a growth ratio of $1\,\text{Å}/\,\text{s}$ (c). Although EBL is a relatively slow process, the technique is very convenient in order to fabricate arrays of dots with different diameters and interdot distances within a limited area of substrate. Identical properties of magnetic material, grain sizes, distribution and film thickness may be obtained over the whole sample. Finally a lift-off process of the double spin coating layers was carried out.

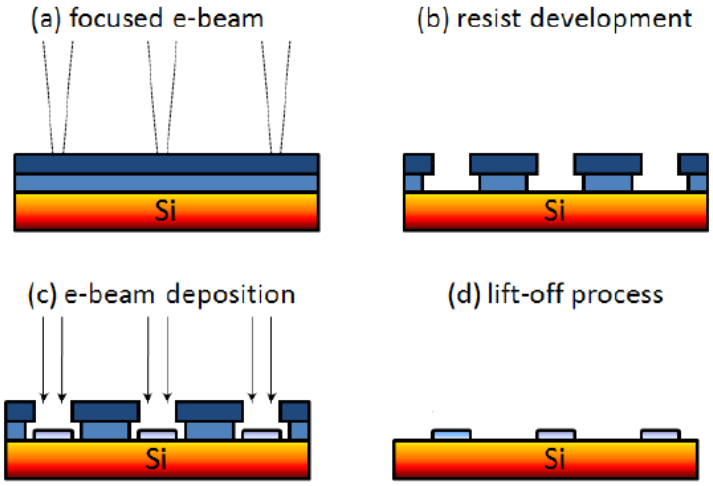

Figure 4.1: Successive steps in the EBL technique: (a) The focused electron beam is applied on the double layered photoresist spin coating layers. (b) After that, a photoresist development is done. (c) With the fabrication of the pattern, the process continues with a magnetic film deposition with a growth ratio of 1 Å/ s. (c) A lift-off process of the double layered resist.

After the sample growth, samples were cut in small pieces and covered by a very fine (few micron) layer of photoresists material to prevent the direct contact with the coplanar wave guide in the set-up. Following this procedure, three different periodic square arrays of 50 nm thick circular magnetic dots of 500 nm radius were fabricated with interdot distances of $1.2, 1.5$ and $2.5\,\mu$m. In order to check the size and shape of the dots, images of the samples have been obtained by using scanning electron microscopy (SEM) technique. Figure 4.2 illustrates the images of the three different arrays of dots where the edge of the dots show a good quality.

As was described in Chapter 1, depending on the aspect ratio $\beta = L/R$, where L is the dot thickness and R is the dot radius, the circular element could have in-plane or out-of-plane magnetization. Reduction of the dot radius to micrometer or submicrometer length scales induces therefore the appearance of a curling spin configuration in the dot and the corresponding vortex state formation where spins are aligned out-of-plane close to the vortex core. This vortex core has an extension of the order of the exchange length L_{ex} which depends on the exchange stiffness $\mathcal{A}$ and the saturation magnetization M_S as $L_{ex} = \sqrt{(2\mathcal{A}/M_S^2)}$. The dots investigated have a thickness of about $3L_{ex}$ and aspect ratio of about 0.1. These parameters ensure vortex configuration in the ground state, i.e. at zero external bias field, and uniform magnetization along the dot thickness (i.e. vertical direction) in the saturated state.

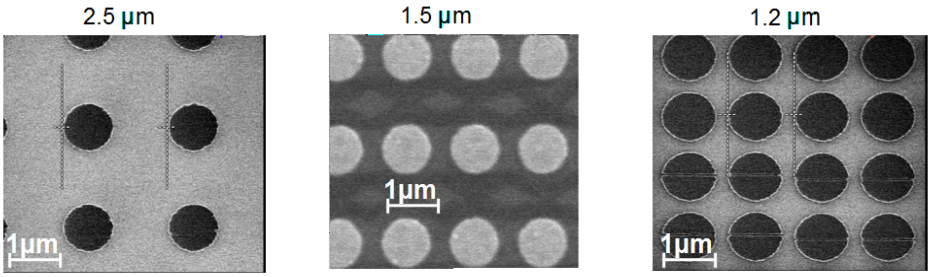

Figure 4.2: Scanning electron micrographs of the arrays of magnetic dots with interdot distance of 2.5, 1.2 and 1.5 μm respectively. We include the length scale of 1 μm.

4.2.2 Magnetic characterization

To ensure presence of the vortex configuration in the ground state the magnetization curves of the samples were measured. *Cowburn* et al. [38] reported the magnetic characterization of arrays of circular nanomagnets with two different ground states: vortex and single-domain configuration by studying experimentally the magnetic phase diagram as a function of diameter and thickness of circular Permalloy elements. As shown in Fig. 4.3, they distinguished two types of magnetization curves.

In the case of vortex ground state (Fig. 4.3a) when the magnetic field is increased from negative saturation to positive saturation field, the nanomagnets retain the magnetic moments up to a critical magnetic field, named nucleation field H_n. After crossing H_n, the nanomagnet completely loses the magnetization close to zero field, which is characteristic of a vortex state configuration. Increasing the magnetic field, the vortex is shifted towards the edge of the disk. After reaching a second critical field, called the annihilation field H_{an}, the vortex is annihilated from the dot, resulting in a nearly uniform structure with most of the magnetic moments aligned in-plane.

In the case of a single-domain configuration (Fig. 4.3b), the magnetization curves present a different behavior. The magnetization inside each dot of the array retains all their magnetization to form an array of giant spins. Magnetization reversal occurs by each giant spin rotating coherently and appears at very low magnetic fields (around $2 - 5$ Oe).

Taking into account the early work of *Cowburn* et al. we have measured the magnetization curves for the three samples using a vibrating sample magnetometer. The samples show the typical magnetization curves with a vortex state configuration. As an example, Fig. 4.4 shows the magnetization curve for the sample with an interdot distance of 1.2 μm.

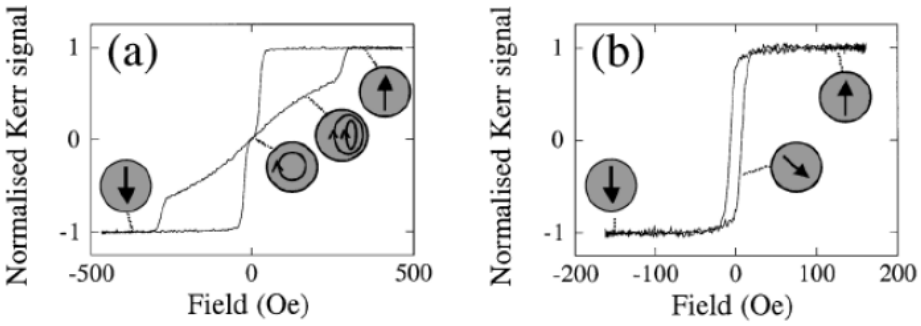

Figure 4.3: Magnetization curves reported by *Cowburn* et al. [38]. (a) Typical hysteresis loop with a vortex state formation in the ground state. In this case a nanodot has thickness (t) of 10 nm and radius (r) of 150 nm. (b) Magnetization loop for a single domain structure ($t = 10\,\text{nm}$; $r = 50\,\text{nm}$). The hysteresis loop shows a low coercive field and a high remanence.

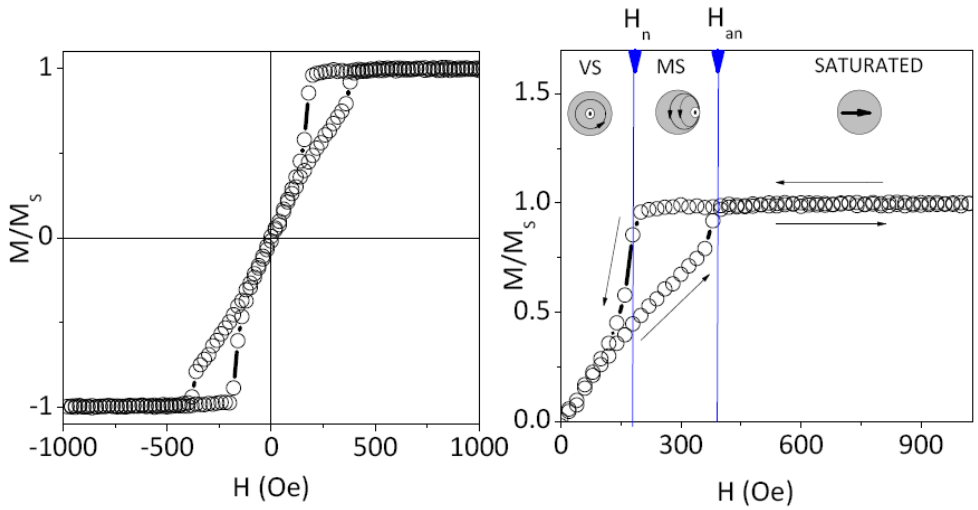

Figure 4.4: Magnetization vs magnetic field measured at room temperature in the array of magnetic dots (described in the text) with an interdot distance of 1.2 μm. The right panel zooms the image of the positive branch of the magnetization curve, where the annihilation and nucleation fields are marked.

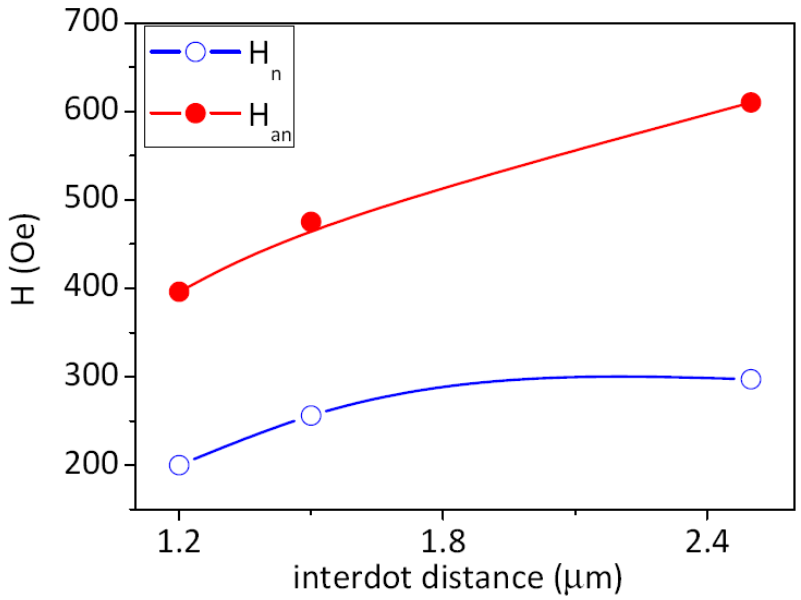

Figure 4.5: Dependence of the nucleation and annihilation fields with the interdot distance for a square array of magnetic dots.

On the right panel a zoom image of the positive branch of the magnetization curve is shown, where the magnetic field direction are indicated. The curve can be divided in three zones. The first one corresponds to magnetic fields greater than the annihilation field H_{an}, i.e $H>H_{an}$, where magnetic dots present a single domain state with an in-plane magnetization. The second one corresponds to magnetic fields between nucleation (H_n) and annihilation fields (H_{an}), i.e $H_n<H<H_{an}$. In this case one can distinguish between positive (from 1000 to -1000 Oe) and negative going branch (from -1000 to 1000 Oe). For positive going branch, the single domain, with in-plane magnetization, is present up to reach H_n, whereas a vortex state (VS) is present for the negative going branch, with the vortex near to the dot edge. We identify this zone as a metastable state (MS). The third one corresponds to magnetic fields $H<H_n$, where VS is stable and is centered on the dot.

Summarizing magnetic characterization, the values of nucleation and annihilation fields versus interdot distance on the samples investigated can be seen in Fig. 4.5 .One observes that in the limit of weak dipolar interactions between dots nucleation and annihilations fields approach to 300 Oe and $600-700$ Oe respectively.

4.3 Ferromagnetic resonance experiments

4.3.1 Details of data acquisition

As was described in Chapter 2, the evaluation method to obtain the ferromagnetic resonance (FMR) spectra in arrays of magnetic dots is based on the technique developed by *Kuanr* et al. [111] (see Eq. 2.1).

Before the measurements, a detailed calibration of the RF-coaxial cables was done. This step in the experimental procedure removes possible contributions to the magnitude and to the phase of the coaxial lines. The evaluated magnetic response of the samples is based on transmission mode detection (analysis of the magnitude of the S_{21} parameter, neglecting reflections). Applying an external bias field one measures the magnitude of S_{21} sweeping the frequency from 300 kHz to 8.5 GHz. The reference spectrum was measured at an external bias field of 1200 Oe, where resonant magnetization dynamics is out of the frequency range of the experimental set-up. In the case of the uniform resonance mode, i.e. Kittel resonance mode, the resonance peak is fitted to a lorentzian curve in order to obtain the resonance frequency and its linewidth (see Appendix B for more details on fitting routines). Typically, the external bias field was changed from 1100 Oe down to 0 Oe with field steps of 20 Oe.

4.3.2 Magnetization dynamics of in-plane saturated magnetized dots approaching the vortex state

The VNA-FMR experiments have been first performed with the external bias field along the <**xyz**>= <**100**> direction, i.e along the dot axis. As an example, a typical normalized response at a fixed magnetic field of 750 Oe for a sample with an interdot distance of 1.5 μm is shown in Fig. 4.6. One can clearly distinguish two separated peaks with different intensities. The high intensity peak corresponds to the uniform resonance mode (A-mode) and the weak peak (B-mode) corresponds to a SW generated in the system.

In order to show the rich variety of the excited SWs in all the frequency and magnetic fields investigated, a careful analysis of the three dimensional (3D) images is plotted for each sample. Figure 4.7 shows the 3D images for the arrays of dots with interdot distances of 2.5 μm, 1.5 μm and 1.2 μm respectively.

One can clearly distinguish in the figures three different excited SWs. One of them is excited in the Vortex State (VS) region. The resonant response called AM (from azimuthal mode) is split in two different branches and will be discussed in the next section. Two other modes are clearly present when the dots are in the in-plane magnetized state. In addition to the main FMR uniform mode (A-mode) a much weaker resonance mode (B-mode) is detected. This resonance with characteristic

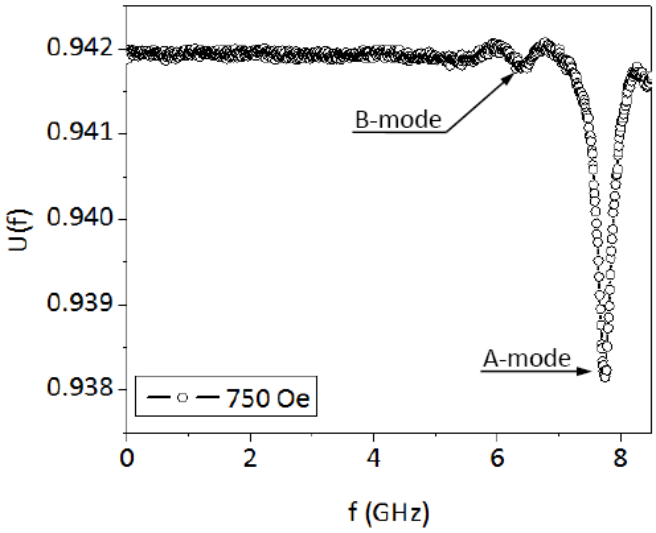

Figure 4.6: A typical FMR spectrum measured with fixed external bias field for the samples studied. The picture shows the spectrum measured in the sample with 1.5 μm of interdot distance when the external bias field is applied along the <100> direction. Two separated peaks can be distinguished at high frequency, corresponding to an uniform resonance mode (A-mode) and a weaker intensity SW generated in the system (B-mode).

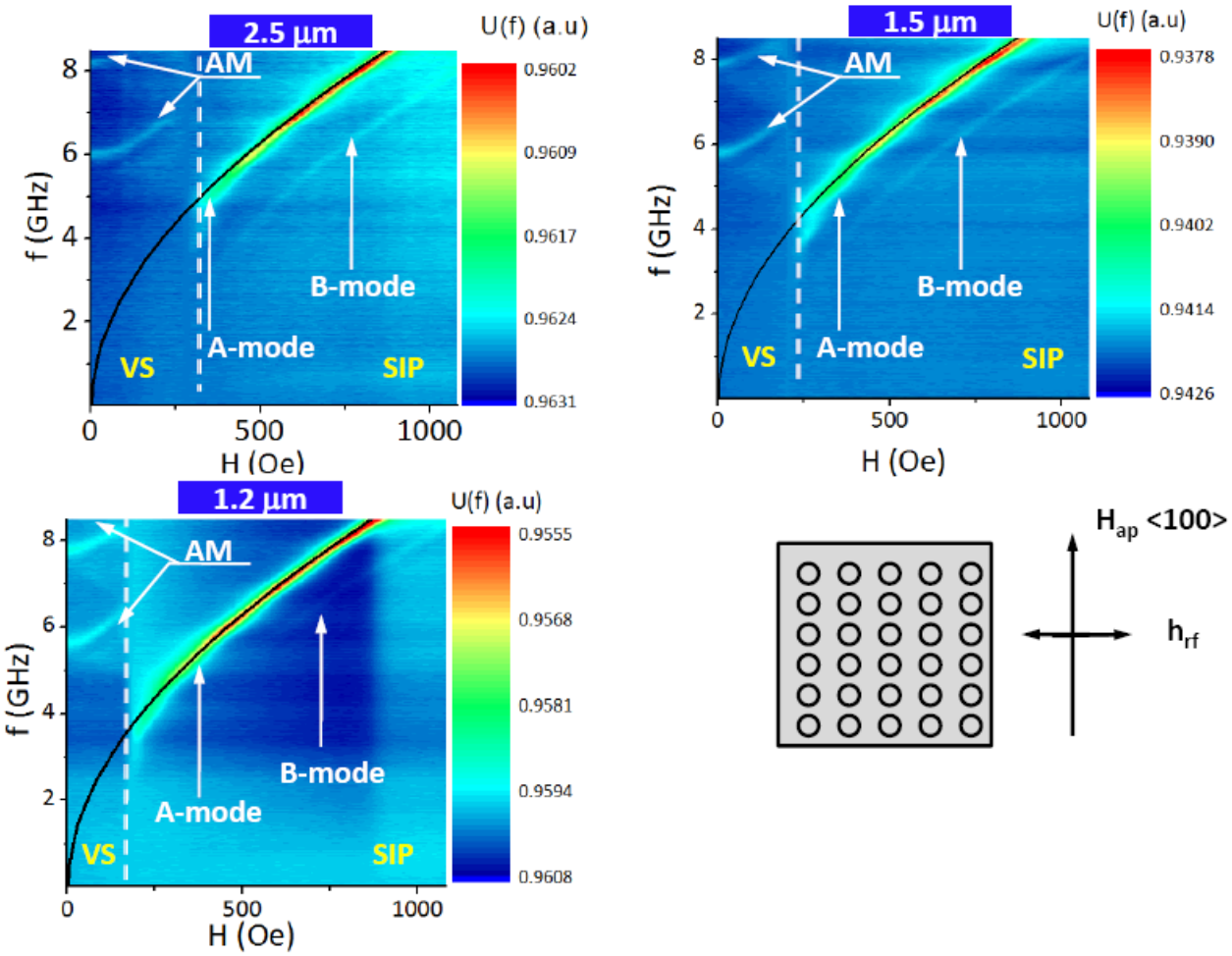

Figure 4.7: 3D images of the FMR spectra (in arbitrary units) measured in the square array of dots with 2.5, 1.5 and 1.2 μm interdot distance. The external bias field is directed along <100>. The dashed lines indicate the annihilation field and divide the ground state in two different regimes: vortex state (VS) and saturated in-plane magnetization (SIP) state. Arrows indicate different excited spin waves. A-mode is the uniform or Kittel resonance mode while B-mode is a magnetostatic backward volume spin wave only observable in SIP regime. In VS regime two azimuthal modes (AM) are detected. The black lines represent theoretical calculations of the uniform mode.

frequencies situated below the Kittel resonance mode has been observed previously by *Gubbiotti* et al. [58] by using BLS technique. The B-mode is interpreted as a magnetostatic backward volume SW mode appearing due to the quantization of the wave vector **q** along two directions: the direction of the external bias field and the direction perpendicular to the surface. In addition to the experimental data, the solid black curves show theoretical calculations of the uniform mode that take into account both the demagnetizing factor of an individual dot and the interdot distance. The local FMR field $\mathrm{H}_r(\mathbf{r})$ is defined by the equation [170]

$$H_r(\mathbf{r}) = \sqrt{H_0^2 + \frac{M_S^2\left[N_z(\mathbf{r}) - N_y(\mathbf{r})\right]^2}{4}} - \frac{M_S^2\left[N_z(\mathbf{r}) - N_y(\mathbf{r}) - 2N_x(\mathbf{r})\right]}{2}\ , \qquad (4.1)$$

where M_S is the saturation magnetization, H_0 is the external bias field and $N_z(\mathbf{r})$, $N_y(\mathbf{r})$ and $N_x(\mathbf{r})$ the local demagnetizing factors, whose values are in the case of an individual dot with $\beta = 0.1$: $N_z(\mathbf{r}) \approx 11.01$, $N_x(\mathbf{r}) = N_y(\mathbf{r}) \approx 0.776$. In the above theoretical calculations the following parameters have been used: dot radius = 500 nm, dot thickness = 50 nm, $\mathrm{M}_S = 830$ Oe and $(\gamma/2\pi) = 2.96$ MHz/Oe (data measured experimentally in [159]). For the magnetic fields below the vortex nucleation field H_n, the uniform mode is not observable anymore. An interesting effect can be observed when the interdot distance changes: a shift of both A and B-modes to higher frequencies and a reduction of the B-mode intensity when the interdot distance is reduced. Figure 4.8 presents the resonance fields H_r for both the A-mode and the B-mode at 6.5 GHz.

In the case of the A-mode one can observe a shift to a lower resonance field of around 10Oe when the interdot distance is reduced. In the case of the B-mode the corresponding shift to a lower resonance field is stronger ($\sim$ 70 Oe) due to the enhanced influence of the dipolar coupling between the dots in this mode, in agreement with similar observations reported earlier [171]. *Kakazei* et al. [170] have reported by means of theoretical studies, supported by conventional FMR experiments, the appearance of a small angular dependence of the resonance fields due to a fourfold magnetic anisotropy in square arrays of circular dots when the interdot distance becomes comparable to the dot diameter. In order to investigate the possible effects of a magnetic anisotropy in the system, FMR experiments were done changing the direction of the external bias field to the <**110**> direction, i.e along the diagonal of the square array of dots. Figure 4.9 shows the evaluated FMR signal in the new direction of the external bias field.

Experimental results in the new configuration of external bias field direction show that while for the sample with an interdot distance of 2.5 μm the spectrum is practically independent of the field direction, the samples with interdot distances of 1.5 μm and 1.2 μm show significant increase of the intensity for the B-mode compared

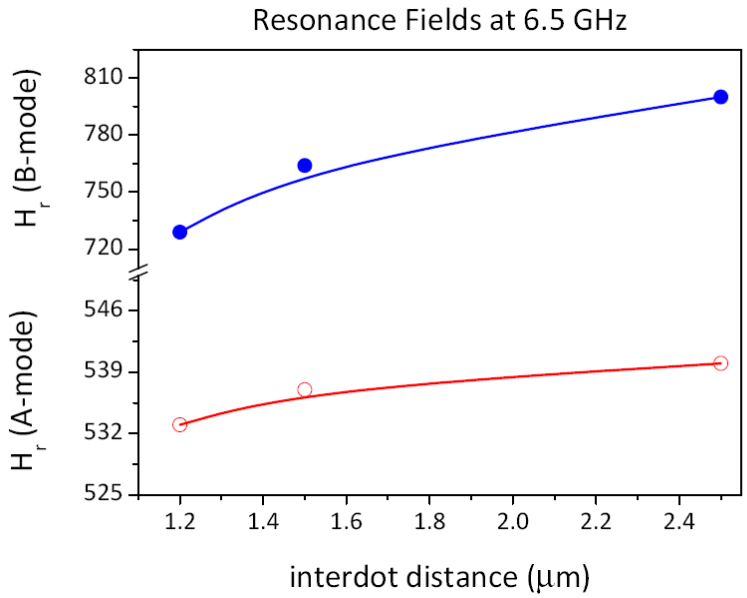

Figure 4.8: FMR resonance fields vs. interdot distance of the uniform mode (A-mode) and the magnetostatic backward volume SW mode (B-mode) at a frequency of 6.5 GHz. The external bias field was applied along the <100> direction.

with the <**100**> direction and the resonance fields shift to lower values, providing further support for the previously reported small fourfold anisotropy in the sample with 1.2 μm of interdot distance. This angular dependence of the in-plane resonance fields for these samples confirms the presence of a weak (<6%) magnetic anisotropy in the system when the interdot distance becomes less or comparable to the dot diameter.

4.3.3 FMR linewidth analysis

From the resonance peak one can evaluate the resonance linewidth obtained by using the VNA-FMR technique. Figure 4.10 shows the relation between linewidth and the external bias field applied along <**100**> from 1200 Oe down to 0 Oe for two of the sampled investigated. It is clearly seen that close to the vortex nucleation field H_n, where the magnetization inhomogeneties in the dots start to grow up, the VNA-FMR linewidth strongly increases. This increase could be explained by the proximity to a vortex metastable state with magnetic inhomogeneities appearing in the dot. At the same time, at high in-plane magnetic fields the FMR for the three samples studied shows a nearly constant linewidth with values close to 280 MHz.

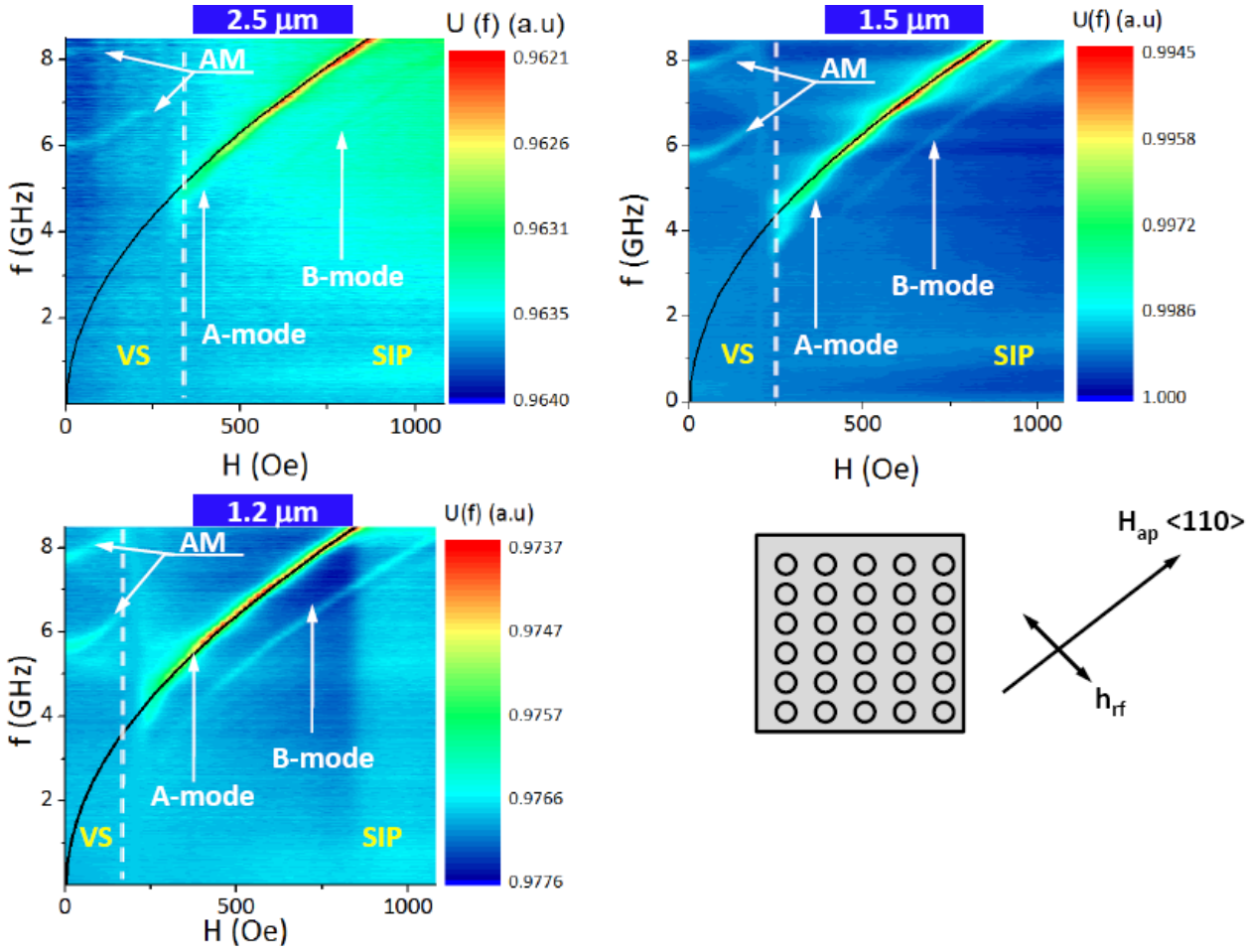

Figure 4.9: 3D images of the FMR spectra measured in the samples when the external bias field was applied in the <110> direction. The dash lines indicate the annihilation field and divide the spectrum in two regimes: vortex state (VS) and saturated in-plane magnetization (SIP). The arrows indicate different excited SWs. The A-mode is the uniform or Kittel resonance mode while the B-mode is a magnetostatic backward volume SW only observable in the SIP regime. In the VS regime two azimuthal modes (AM) are detected. The black lines represent theoretical calculations of the uniform mode.

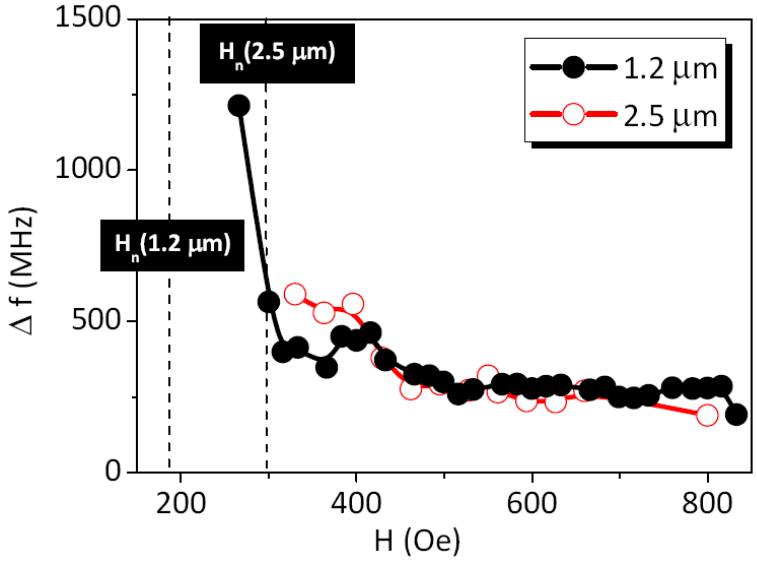

Figure 4.10: VNA-FMR linewidth vs. magnetic field applied along the <100> direction for two of the samples studied. Magnetic field decreased from the saturated state. The vertical dash lines indicate the corresponding vortex nucleation fields.

4.3.4 Vector network analyzer and conventional FMR methods

In addition to the VNA-FMR data, the FMR was also measured by using the conventional cavity method in collaboration with Dr. G. Kakazei (University of Oporto, Portugal). Figure 4.11 compares the derivative of the microwave absorption at 10 GHz (X-band) for the samples with 2.5 μm and 1.2 μm interdot distances, when the external bias field was applied along the <**100**> direction.

The high amplitude peak corresponds to the Kittel resonance (A-mode) and the second smaller peak with much smaller amplitude and marked with arrows, is the SW resonance (B-mode) detected at higher fields. Additionally, a third peak at low fields in the spectra could be related to the vortex resonance excitations. The separation between A and B modes is 270 Oe when interdot distance is 2.5 μm and 330 Oe when the interdot distance is 1.2 μm. An extrapolation of the VNA-FMR data from 8.5 GHz to 10 GHz made for both samples shows separations between the A-mode and the B-mode of about 280 Oe for 2.5 μm interdot distance, and 315 Oe for 1.2 μm interdot distance, demonstrating reasonably good agreement between both techniques.

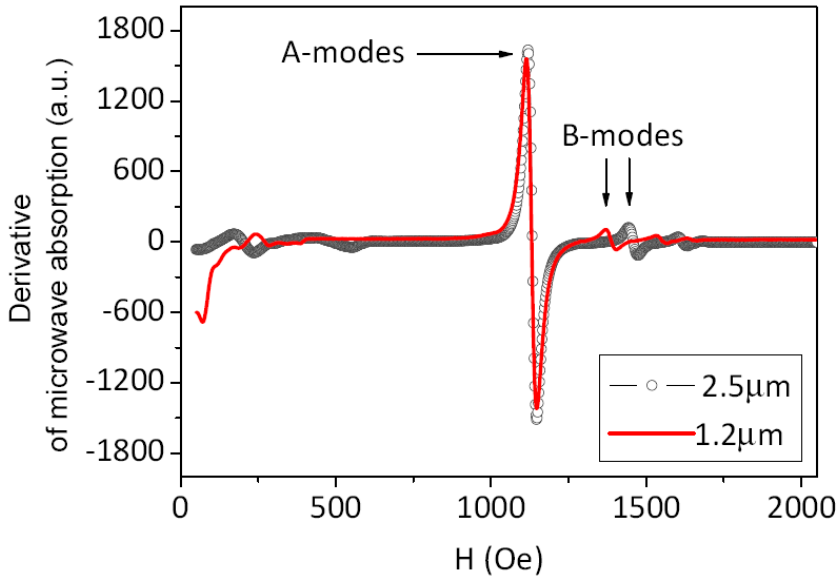

Figure 4.11: Derivative of the microwave absorption of the samples with 2.5 μm and 1.2 μm of interdot distance. The spectra were taken with the conventional FMR cavity method. At a fixed frequency of 10 GHz the external bias field was swept from 0 to 2000Oe. From the spectra, one can clearly distinguish two different peaks in the saturated state, marked with arrows and identified as B-modes and A-modes for each sample. At low external bias field, the spectra show a weak signal that could be related to a vortex resonance excitation (measurements done by G. Kakazei).

4.3.5 Magnetization dynamics in the vortex state

As was discussed in the Introduction Chapter and was briefly demonstrated above (see Figs. 4.7 and 4.9) the magnetic vortex state (VS) is characterized by three main spin excitation modes named gyrotropic, radial and azimuthal modes (AM) and therefore has qualitative differences from the saturated state magnetization dynamics**.** This paragraph investigates in more detail the magnetization dynamics when the vortices are present in the magnetic nanodots.

Actually, due to the reduced magnetization, the experimentally measured magnetization dynamics response in the VS is considerably reduced in comparison to the one observed in the magnetically saturated state. Due to this and some other reasons related to the experimental geometry employed (pumping field parallel to the dots plane with relatively small amplitude not exceeding 0.2 Oe), we could clearly detect the magnetization dynamics corresponding to only one of the above mentioned three main modes. In addition, the presence of very weak signals in the VS forced us to develop a new "differential" detection scheme with multiple averaging.

The experimental measurements were performed with the following procedure: we started to measure the VNA spectra close to the negative field value equal to the annihilation field H_a. The field was swept up in steps of 10 Oe, crossing the zero value and was increased to the region just before the H_a. After that, we decreased field with the same field history (down in field). We have adopted the "cage effect" notation for the results obtained using this experimental procedure following the analogy between a cage (dots) and a bird (magnetic vortex), both captured in the "cage" and with their response investigated via "inclination of the cage" from side to side. In order to analyze the results numerically (which basically provide a differential SW response analog of the typically employed in conventional FMR measurements) we used as a reference spectrum the one measured just with the previous field, i.e:

$$U(f)[H_i] = \frac{S_{21}(H_i)}{S_{21}(H_{i-1})} \quad , \tag{4.2}$$

We have employed this procedure to investigate the room temperature magnetization dynamics in the VS of three arrays of Permalloy dots with different interdot distance and same aspect ratio.

As an example, Fig. 4.12 shows the 3D SW spectrum (top panel), the magnetization curve (middle panel) and the derivative curve of the magnetization (bottom panel) measured in the field region $-H_a<H<H_a$ in the sample with an interdot distance of 1.2 μm , with the external bias field applied along the <**100**> direction and the pumping field h_{rf} being perpendicular to it. The blue color in the top panel represents maxima while the red color represents minima in the differential spectra.

The blue color in the top panel represents maxima while the red color represents minima in the differential spectra.

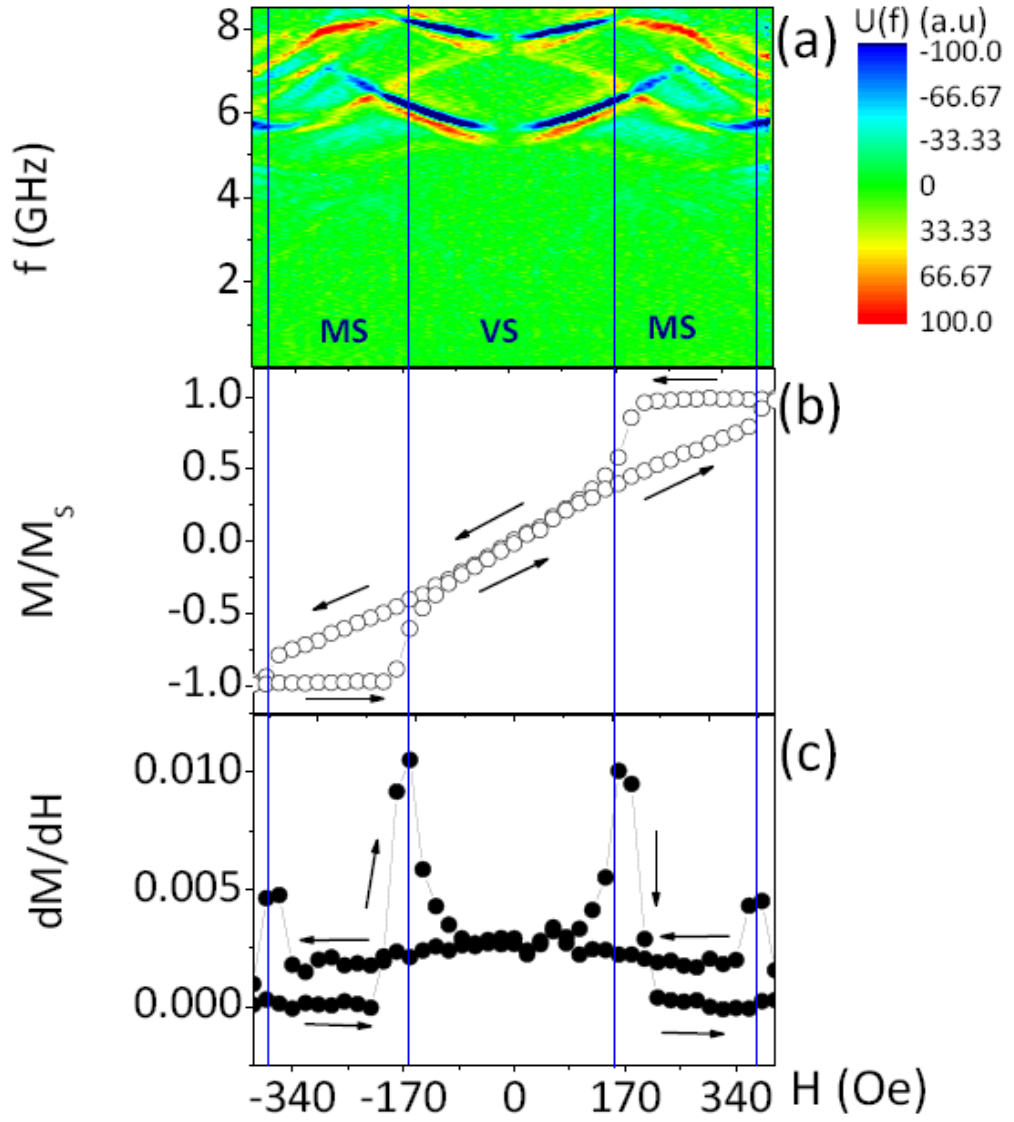

Figure 4.12: (Top panel). 3D image of the spectra measured using the so-called "cage effect" being the external bias field along the <100> direction and h_{rf} perpendicular to it. (Middle panel). Normalized magnetization curve of the sample. (Bottom panel). Derivative curve of the magnetization, with arrows indicating the magnetic field sweeping direction. The vertical lines divide the magnetic field region in the vortex metastable state (MS) and the vortex state (VS).

Looking into the field regions marked as MS, we see that the 3D SW spectrum shows different SWs excitations with crossing regions between blue and red lines. As can be seen in the bottom panel of Fig. 4.12, these crossing regions coincide with those where positive and negative going magnetization branches coincide. It is interesting to notice that with the "cage effect" experiments we are not reaching the annihilation field. This allows us to create periodically the metastable state (MS) when the bias field is decreased and to study different SW excitations either in metastable (H_n <H<H_a) and the stable vortex (VS) (H<H_n) states.

In the MS state we observed rather complicated SW spectrum.

As was shown in Chapter 1, the high frequency spin wave modes in the vortex state can be labelled by the number of nodes n and m along the radial ρ and the azimuthal ϕ directions respectively (see Eq. 1.20)

Looking at the region marked as VS, the magnetization response is not so complicated, with an evident splitting (doublet) of a resonance mode (blue lines), which seems to correspond to the first splitting azimuthal mode (AM) ($n = 0; m = \pm 1$) [52]. We identify these AMs due to the scheme of excitation: whereas an out-of-plane pumping field does not affect the initial position of the vortex core and produces the same initial torque in the magnetization out of the core exciting only radial modes, an in-plane pumping field produces a torque in the vortex core and in the nonhomogeneous magnetization out of the core, moving the vortex core away from its equilibrium position (center) and producing an excitation of modes with rotational symmetry, i.e. both radial and azimuthal modes. Furthermore, our results are in good agreement with theoretical [51] and numerical [172] predictions for the values and the splitting of the AM lowest in energy.

We note that in those cases where parallel to the blue lines there are red lines also present, this actually does not represent any additional excitation mode but appears due to the differentiation method used. For the same reason, the dynamic response is absent close to H=0. Finally, one can observe a weak mode (yellow line) that is present in both, VS and MS states.

We have observed a clear correlation between the magnetization curve and the measured differential SW mode spectrum (Fig. 4.12). Around H=0, the positive and negative going magnetization branches coincide and make that AMs will be clearly detectable. On the other hand, for H_a<H<H_n, both the positive and the negative going magnetization branches do not coincide. This indicates the presence of two different energy states for vortices (stable and metastable) at the same magnetic field, creating a qualitatively different and rather complicated SW modes in the MS field interval.

In order to verify the influence of the dipolar interaction between dots on AMs, the SW modes were measured for the three samples with the interdot distance varying from 1.2 μm to 2.5 μm. Figure 4.13 plots the characteristic frequencies (split doublet) for the first AM ($n = 0; m = +1$ and $n = 0; m = -1$) vs. interdot distance.

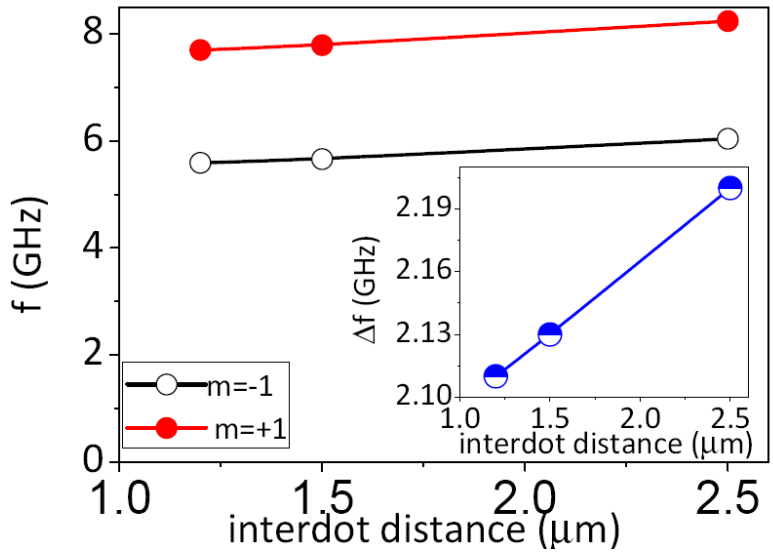

Figure 4.13: Resonance frequency of the first azimuthal mode at zero bias field vs dots aspect ratio. Open symbols correspond to $n = 0; m = -1$ and full symbols correspond to $n = 0; m = +1$. The inset shows the splitting value Δf of the doublet $n = 0; m = \pm 1$.

From the data, one concludes that decreasing the interdot distance slightly (in about 10%) reduces the resonance frequency of the first AM.

As shows the inset of the Fig. 4.13, one observes that the splitting of the doublet $n = 0; m = \pm 1$ also decreases with interdot distance approximately to about 2 GHz, i.e. the inter-dot dipolar coupling reduces the first AM splitting.

We have also carried out similar "cage effect" experiments when both, pumping and bias field, were applied parallel to the <**100**> direction. We note, however, that in the new field geometry the intensity of the resonance modes is somewhat smaller than in the previous experiments, where the pumping field was perpendicular to the bias field. Figure 4.14 shows the corresponding 3D differential SW spectrum.

Interestingly we found that a "soft" resonance mode appears in the MS regime (H_a<H<H_n) with parallel pumping. The difference in the SW response between parallel and perpendicular pumping in the MS regime could be a consequence of the proximity of the vortex core to the dot edge. A pronounced splitting mode, identified as the first AM, with a splitting $\Delta f \approx 2$ GHz, is again detected in the VS.

The splitting of the AMs in circular nanomagnets has been intensively studied both theoretically and experimentally**.** *Ivanov* et al. [173] studied theoretically the high frequency splitting of the first ($n = 0; m = \pm 1$) and second ($n = 0; m = \pm 2$) AM for an individual dot as well as the variation of their frequencies and the splitting with the magnetic field, showing a parabolic dependence of the AM-SW resonance

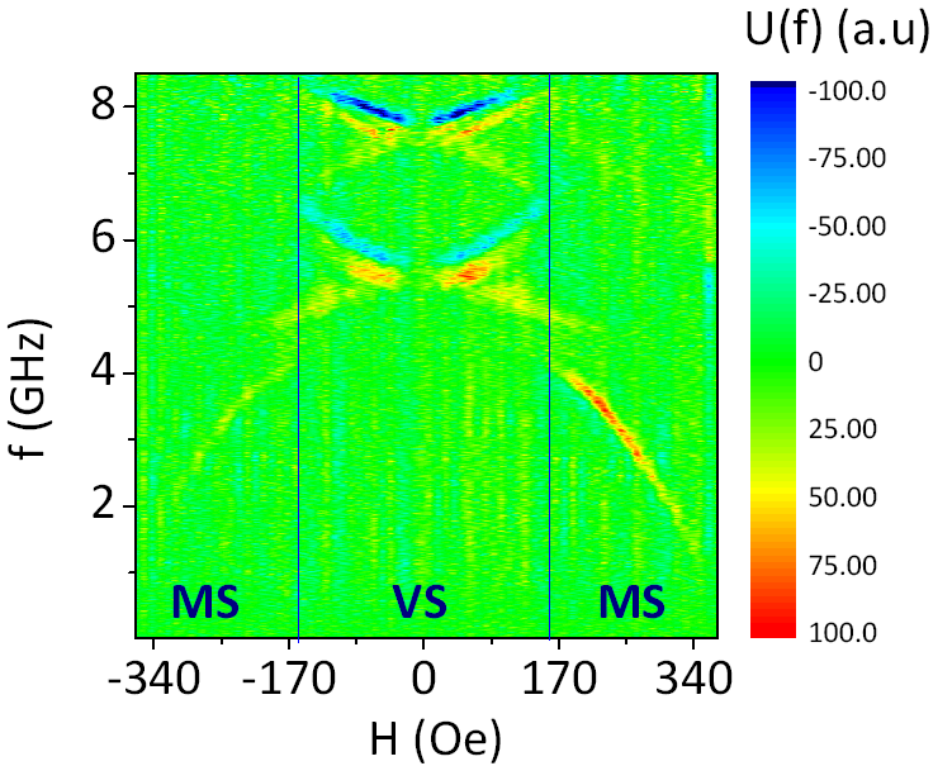

Figure 4.14: 3D spin wave spectrum on the array of magnetic dots with an interdot distance of 1.2 μm when the pumping and the external bias field are parallel to the <100> direction measured using "cage effect" .

on the magnetic field. According to the authors, the origin of the AM splitting is the inter-mode coupling between the low frequency gyrotropic motion of the vortex core and high frequency SWs in the VS. The perpendicular magnetization of the vortex core breaks the otherwise perfect symmetry for left and right handed rotations. The zero magnetic field frequency splitting arises from the fact that the magnons scattered by the vortex core are different for the clockwise and anti-clockwise modes [50]. For the first AM they evaluated a splitting (Δf) of about 0.2 GHz when $\beta(L/R) = 0.1$, providing a value which is approximately one half of the low frequency gyrotropic mode ($f_G = 0.44\,\text{GHz}$).

On the other hand, numerical simulations [172] and experimental detection [52] have reported splitting of 2 GHz and 1.25 GHz respectively for the first AM when $\beta(L/R) = 0.1$.

More recently, *Guslienko* et al. **[51]** also have investigated theoretically the first AM splitting obtaining a value of $\Delta f = 1.54\,\text{GHz}$. According to the authors, the frequency splitting of the first azimuthal SW modes is interpreted as a hybridization of these with the gyrotropic mode. The AM may propagate (rotate) either clockwise or anti-clockwise and therefore is degenerate if does not interact with other SWs. However, the rotation of the AM in the direction of the gyrotropic mode decreases the SW frequency ($m = -1$), whereas the rotation in the opposite direction increases the SW frequency ($m = +1$). Although the splitting due to the coupling between low frequency gyrotropic mode and the high frequency SWs reported by *Ivanov* et al. [173] also exists, is one order of magnitude smaller than the splitting factor obtained with this new alternative (still unpublished) theoretical approach **[51]**.

We conclude that our splitting value of $\Delta f = 2\,\text{GHz}$ is consistent with the previous experimental works [172] [52] and with the new theoretical approach reported in Ref.**[51].** Figure 4.15 summarizes the SW dynamics in the vortex state by introducing sketches which explain the difference in the observed two azimuthal modes (with opposite spin wave propagation) and position of the vortex in the metastable state. Additionally, the figure demonstrates a clear parabolic fitting of the AM resonance frequency vs. magnetic field dependence in the stable vortex state (white line in the VS regime). Qualitatively similar parabolic dependence for the AM frequencies vs field was also observed for the parallel RF pumping scheme. This is agreement with unpublished theoretical prediction of *Guslienko* **[174]**

Figure 4.16 shows the theoretical prediction and the experimental values of the first AM resonance vs. aspect ratio for samples with 1.2 μm (full circles) and 2.5 μm (open circles) interdot distances showing the good correspondence between theory and experiments.

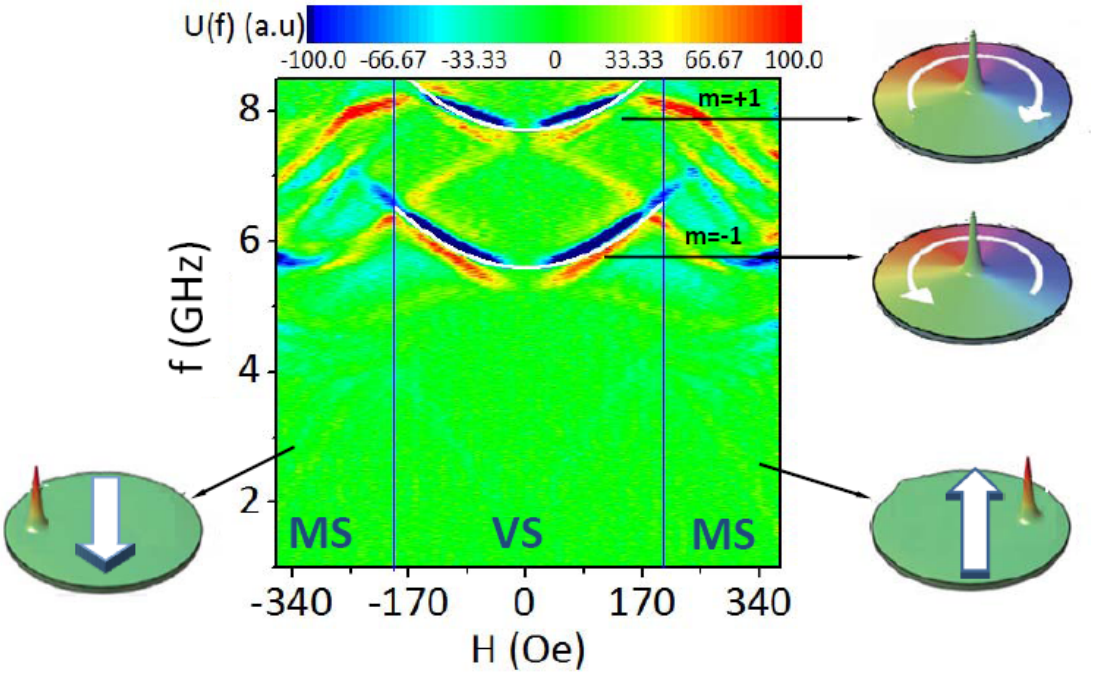

Figure 4.15: 3D spin wave spectrum in the vortex state as a function of the applied magnetic field measured with "cage effect" procedure. The splitting in the first azimuthal mode correspond to the hybridization of $m = +1$ (clockwise rotation) and $m = -1$ (anti-clockwise) with the vortex translational mode (clockwise). In the dot the spike represents the vortex core and the in-plane curling magnetization distribution is marked by different colors. In metastable state (MS) regions, the vortex core shifts to the right (increasing field) and to the left (decreasing field) of the dot edge. White arrows correspond to the applied field direction. White color lines show fitting of the split azimuthal mode to a parabolic function.

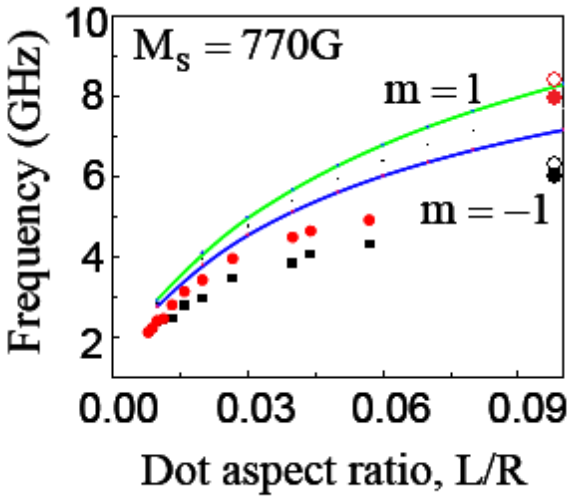

Figure 4.16: The frequency splitting for the first azimuthal mode as a function of aspect ration: theoretical prediction and experimental data. The solid lines represent the analytical theoretical results. The obtained here experimental results for L/R=0.1 are shown for samples with aspect ratio of L/R=0.1 and interdot distance of 1.2 μm (full circles) and 2.5 μm (open circles). The smaller symbols correspond to the experimental data reported in [52] and [53]

4.4 Conclusions

We conclude that by using the vector network analyzer technique we have investigated the dynamic response of Permalloy dots:

We were able to observe qualitatively different types of spin excitations in arrays of Permalloy dots, including the uniform Kittel mode, SWs in confined geometries and VS related SWs. These measurements have been supported by conventional FMR experiments.

The VNA-FMR-linewidth in the saturated state has been found to increase notably when approaching to the vortex nucleation regime.

In the saturated state, a qualitative difference in the dynamic response between Permalloy dot arrays with different interdot distances has been observed, indicating that the magnetization dynamics of individual dots is affected by a dipolar coupling between dots when the interdot distance is reduced. The investigation of a possible angular dependence of the in-plane resonance fields confirms the presence of a weak ($<6\%$) magnetic anisotropy in the samples where the interdot distance becomes less or comparable to the dot diameter.

Finally, the high frequency modes in the VS has been studied by measuring multiple SW resonances in the metastable state and near zero field. The investigation has been done using different excitation schemes with relative orientation of the RF pumping and the applied magnetic field, both being in the dot plane: parallel (pumping and applied field along the same direction) and transverse (pumping and applied field in perpendicular directions) excitation schemes. Both with the parallel and the transverse (perpendicular) schemes the first AM ($n = 0; m = \pm 1$) and its splitting have been detected and their frequencies (in the VS) were found to vary quadratically with the bias field value. We show that the large splitting of the low lying azimuthal mode could be a consequence of the hybridization of these modes with the gyrotropic mode.

Chapter 5

Magnetization dynamics in magnetic tunnel junctions

5.1 Introduction

This Chapter presents the investigation of the magnetization dynamics of the magnetically soft Permalloy thin films grown in magnetic tunnel junctions. The measurements have been carried out in a wide frequency (up to 20 GHz) and temperature (down to 2 K) range.

As was previously described in Chapter 1, the basic structure of a magnetic tunnel junction (MTJ) consists of two ferromagnetic (FM) electrodes separated by an insulating barrier. It was in 1975 when *Jullière* reported the first evidence of a tunneling magnetoresistive effect in junctions with FM electrodes of iron and cobalt sandwiching an insulating barrier of germanium [26]. The effect was observable only at low temperatures (T= 4.2 K) reaching a value of 14% tunnel magnetoresistance (TMR). The practical realization with high values of TMR had to wait till 1995 when two independent groups [24] [25] reported a significant and reproducible values of the TMR at room temperature. This was done thanks to the considerable progress in the deposition and patterning techniques. From the 10.6% room temperature TMR value reported in 1995, the improvement of the growth techniques and the quality of the structures led to more than 472% room temperature TMR observed by *Hayakawa* et al. [175] in 2006 in junctions with an crystalline MgO barrier structure and CoFeB electrodes. In the case of amorphous alumina barriers, *Wang* et al. [176] obtained in 2004 values exceeding 70% room temperatures TMR in CoFeB/Al_2O_3/CoFeB MTJs. Advances in the development of both types, crystalline and amorphous MTJs, together with the advances in the design of low noise and fast responding to external magnetic field devices, stimulated the implementation of MTJs in technology such as magnetic recording [177], low-field magnetic sensors [178], magnetic random access memory (MRAM) [179], high-frequency spintronics

[180] and logic devices [181], both at room and low temperatures. The quality of the junctions depends critically on the type of insulating barrier, the FM electrodes composition and on the interfacial characteristics [182]. These properties include interfacial roughness, intermixing, oxygen content, which in turn depend on materials used in the stack, deposition and annealing conditions.

This chapter describes a systematic study of GHz magnetization dynamics in MTJs with Al_2O_3 amorphous insulating barriers in a wide temperature range. We employ ferromagnetic resonance (FMR) studies which, as was explained in the Chapter 1 and 2, has been an effective tool during the last decades to get insight into both the magnetization dynamics and the quality of different magnetic structures such as single ferromagnetic layers [183], multilayers [184], exchange biased layers [185], and MTJs [186]. The resonance linewidth is dependent on the intrinsic magnetic damping and on extrinsic factors. The extrinsic factors include the quality of the FM electrodes, i.e. the presence of local moments or antiferromagnetic phases produced by a non ideal oxygen distribution near the tunnel barrier, leakage spin currents, thermally agitated spin diffusion and presence of undesirable magnetic coupling such as Néel or "orange-peel" coupling. Both the intrinsic and the extrinsic damping, are important in determining switching times [187], oscillator linewidth [188], and detector bandwidths in MTJ devices [180]. The extrinsic damping may also be correlated with other important device properties such as switching distributions in MRAM devices and low frequency noise in magnetic field sensors.

The Chapter is divided in three different sections:

- The study of the influence of annealing conditions on the quality of MTJs measured via FMR.
- The influence of different oxidation processes on the quality of MTJs determined via FMR, and finally
- The influence of temperature on the magnetization dynamics and the static magnetic properties of MTJs.

In all junctions under study the magnetization dynamics of Permalloy free layer is measured. When appropriate, also a response of the reference Permalloy film is studied.

5.2 MTJs: sample preparation and structure

Most of the MTJs investigated (except specified separately) were grown during 3+3 months scientific visits of Juan F. Sierra to the group of Dr. Stephen Russek, NIST-Boulder, Colorado, USA, by using the sputtering technique. The sputtering system is located in an ultra high vacuum (UHV) chamber with a base pressure of 10^{-9} torr. The DC-magnetron sputtering chamber has eight sputtering guns. The samples are grown in a controlled atmosphere of an inert gas of Ar. Basically, the process consist of collide a target of the material that is to be deposited, with ions.

In the collision, ions pull up atoms that are deposited on a substrate. Ions are originated and accelerate in a plasma, produced in an Ar atmosphere in the system. The difference of voltage between the target (cathode) and a metallic ring that surround it (anode) leads to electric discharge that produce the gas ionization. The particularity of the magnetron sputtering system is the use of a magnetic field to produce a plasma confinement around the target, this makes that the process will be more effective. The DC power used for the deposition varies from target to target, typically ˜100 W for 2′ targets. Furthermore**,** a pre-oxidation process well before insulating barrier deposition was introduced in some MTJs, this could be possible thanks to the different gas flow that can be applied in the sputtering chamber. Figure 5.1a shows a picture of the sputtering chamber, located in the National Institute of Standards and Technology (NIST) and a picture of the substrates used for MTJs deposition.

MTJs were deposited on insulating quartz substrates (Fig. 5.1b). Deposition pressure was of a few m torr in an Ar atmosphere and was done at room temperature in an applied DC magnetic field parallel to the substrate surface of ~ 18 mT. After deposition, the samples were annealed *in-situ* at 250 C for one hour in applied DC magnetic field of 20 mT. The basic structure of the MTJs investigated is shown in Fig. 5.1c. Two FM electrodes are separated by an insulating barrier of Al_2O_3. The magnetization is free to rotate at moderate applied magnetic fields in the free layer, formed by a $Ni_{80}Fe_{20}/Co_{60}Fe_{20}B_{20}$ or $Ni_{80}Fe_{20}/Co_{90}Fe_{10}$, while the fixed layer is formed by a $Co_{90}Fe_{10}$ layer exchange biased by a natural antiferromagnetic layer of IrMn. In order to determine the structural characteristics of the samples, a transmission electron microscopy (TEM) images were taken in CNRS-Toulousse (France) with a low magnification (LM) and high resolution TEM (HRTEM) experiments using a FEI-F20 microscope fitted with a spherical aberration (Cs) corrector (CEOS) whose point resolution is 0.12 nm. Figure 5.2 shows an example of TEM images in two of the MTJs investigated. The last section discusses in more details the TEM images in relation to the temperature dependent magnetization dynamics in Permalloy.

In the case of tunnel junctions with a $Co_{90}Fe_{10}$ /$Ni_{80}Fe_{20}$ free layer, the LM micrographs show the continuity of the stacking over large distances (few μm). The thickness of the Al_2O_3barrier is ˜1.8 nm with an amorphous texture and pretty rough. The Ru \$Ir_{20}Mn_{80}$ \$Co_{90}Fe_{10}$ stacking is found to be polycrystalline with a large grain size (˜10 nm) and textured [111] cfc while the upper $Co_{90}Fe_{10}$ /$Ni_{80}Fe_{20}$ / Ta / Ru layers are less textured with smaller grains. On the other hand, in the tunnel junctions with $Ni_{80}Fe_{20}/Co_{60}Fe_{20}B_{20}$ free layer, the LM micrographs show the continuity of the stacking over large distances. The Al_2O_3 barrier is found amorphous with a smaller roughness than junctions with $Co_{90}Fe_{10}$ /$Ni_{80}Fe_{20}$ free layer and not evidence of any pinholes was found. The crystallization of the Ru /$Ir_{20}Mn_{80}$ /$Co_{90}Fe_{10}$ stacking presents high [111] texture while the upper $Co_{60}Fe_{20}B_{20}$ layer

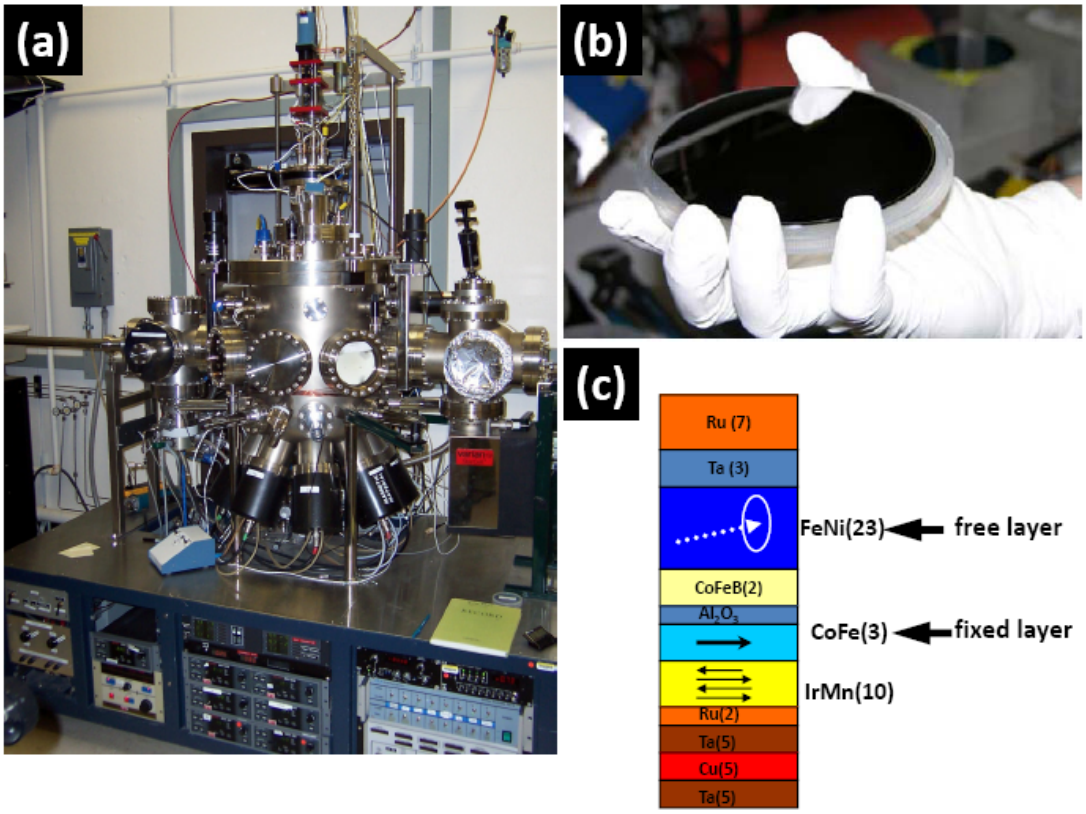

Figure 5.1: (a) DC magnetron sputtering chamber located in NIST, Boulder, USA. (b) Quartz substrates used for MTJs deposition.(c) The basic structure of the MTJs investigated. CoFe is exchange biased by IrMn and forms the fixed layer while NiFe/CoFeB forms the free layer. The thickness of the layers are in nm.

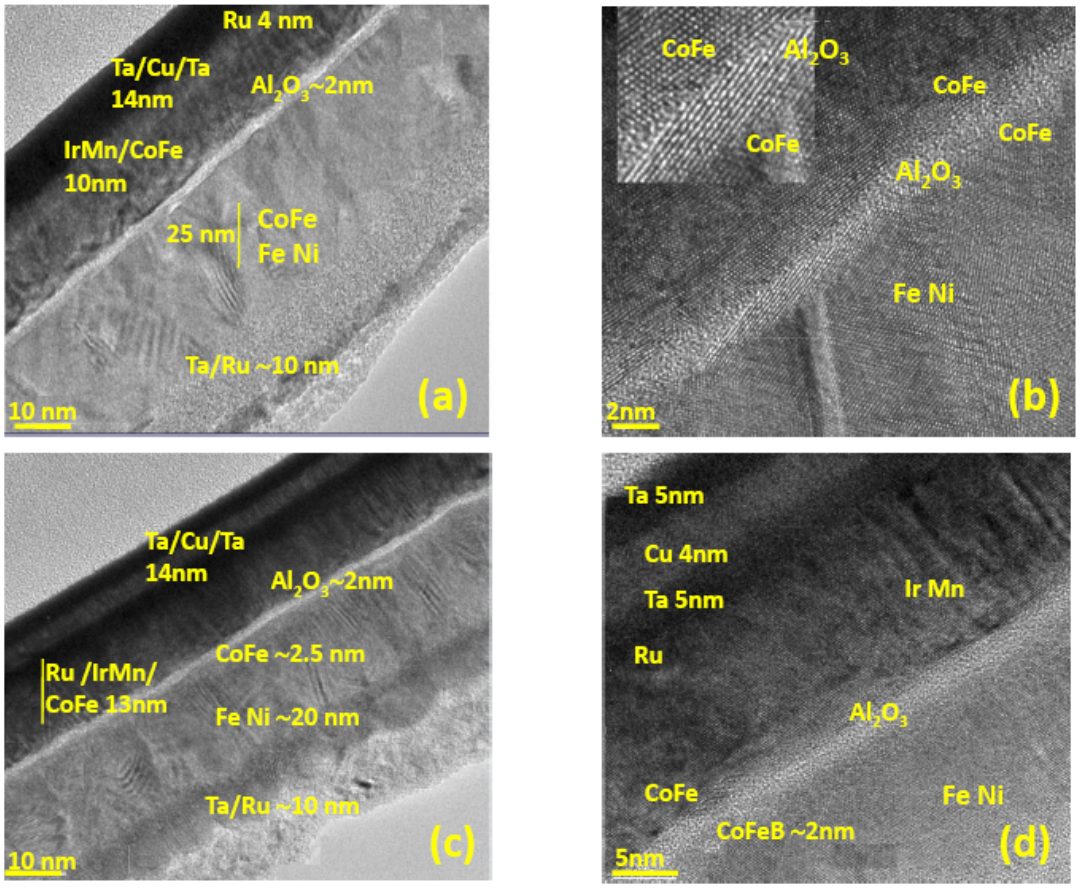

Figure 5.2: TEM images for MTJs with $Ni_{80}Fe_{20}/Co_{90}Fe_{10}$ free layer; (a) LM micrographs with showing the continuity of the stacking. (b) HREM micrograph of the stacking: Note some correlated and anticorrelated variation of the barrier thickness. TEM images for MTJs with $Ni_{80}Fe_{20}/Co_{80}Fe_{20}B_{20}$ free layer; (c) LM micrograph of the MTJ with .(d) HREM images of the stacking. Note the (111) texture of Cu, Ru, IrMn and CoFe. Ta layer appears amorphous as well as the upper CoFeB layer and the Al_2O_3 barrier.

seems to be amorphous and the $Ni_{80}Fe_{20}$ upper layer is highly [111] textured.

5.3 Influence of the annealing

This section describes and discusses the influence of annealing processes on the MTJs quality investigating the magnetization dynamics data obtained using the broadband vector network analyzer technique. The primary goal is to characterize interfacial properties of MTJs at the wafer level and correlate regions of increased linewidth with the reversal of the free and fixed layers, the appearance of magnetization ripple, and enhanced 1/f noise.

The structure of the MTJs used for FMR measurements was: [Ta(5 nm)/ Cu(5 nm)/ Ta(5 nm)/ Ru(2 nm)/ $Ir_{20}Mn_{80}$(10 nm)/ $Co_{90}Fe_{10}$(3 nm)/ Al_2O_3(1 nm)/ $Co_{60}Fe_{20}B_{20}$ (2 nm)/ $Ni_{80}Fe_{20}$(23 nm)/ Ta(3 nm)/ Ru(7 nm)], (see Fig .5.1c) where $Co_{90}Fe_{10}$(3 nm) forms the magnetically fixed layer. The samples patterned into devices had a similar stack structure except that the fixed layer was a $Co_{90}Fe_{10}$/ Ru/ $Co_{60}Fe_{20}B_{20}$ synthetic antiferromagnetic. The $Co_{60}Fe_{20}B_{20}$(2 nm)/ $Ni_{80}Fe_{20}$(23 nm) forms the magnetically soft layer which is studied here. The FMR signal shown correspond to the free layer (FMR of the fixed layer was not measured).

Additional samples with just the free layer [Al_2O_3(1 nm)/ $Co_{60}Fe_{20}B_{20}$(2 nm)/ $Ni_{80}Fe_{20}$(23 nm)/ Ta(3 nm)/ Ru(7 nm)] were fabricated for comparison. The entire wafers were annealed at 250 °C in the sputtering chamber for one hour in applied magnetic field of 20 mT. The wafers were diced into 12 nm coupons and some samples were further annealed for one hour in an applied magnetic field of 100 mT along the same direction as the deposition field. In this Chapter we present data obtained on four coupons from a single wafer: an as-deposited sample, a 250 °C annealed sample, a 275 °C annealed sample, and a 300 °C annealed sample.

The high frequency magnetization dynamics measurements were carried out at room temperature by using a commercial Agilent E8363B (PNA series) vector network analyzer (VNA) working at frequencies up to 20 GHz and located in NIST-Boulder. As was mentioned in Chapter 2, one can determine the FMR frequency and linewidth using the technique developed by *Kalarickal* et al. [112]. The transmitted signal was normalized to a spectrum taken at a field whose resonance was considerably higher than the resonances being measured. For high frequency scans the reference field was typically 0.6 T while for low field scans (< 8 GHz) the reference field was typically 0.15 T. The reference fields serve also as the initialization field which resets the magnetization to well defined state before each measurement. Both positive and negative going sweeps were obtained in which the initialization/reference fields are anti-aligned and aligned with the fixed direction respectively. The absorption peaks were fitted to a resonance model in which the real and imaginary parts were fitted simultaneously [112] (see Appendix B). The quasi-static magnetization was measured as a function of applied magnetic field at room temperature by using

a vibrating sample magnetometer (VSM) situated in NIST-Boulder.

Figure 5.3 shows the resistance of a 64-element MTJ bridge as a function of applied magnetic field along with the resistance noise measured at 10 Hz (the applied voltage was $V_s = 1\,\mathrm{V}$). These measurements were carried out in NIST. The peaks in the resistance noise are due to thermally activated magnetization fluctuations. Noise due to environmental magnetic field fluctuations has been eliminated by using a symmetric bridge, which is largely immune to environmental field noise, and by measuring in a shielded environment with low noise field sources. Peaks in the low frequency noise are seen in the regions of the free layer reversal and the fixed layer reversal (Fig. 5.3). The noise peaks are considerably larger when the field scan is initiated with the fixed layer being antiparallel to its zero field orientation than when the field cycle starts with the fixed layer oriented parallel to its pinned direction. The main source of the low frequency magnetization noise is thought to be associated with the magnetization rippled induced in the free layer by disorder in the fixed layer [189].

Figure 5.4 compares the magnetic field dependence of the quasi-static magnetization M, FMR frequency f_0, and the FMR linewidth Δf_0 for the as-deposited and 275 °C annealed MTJ samples. As seen from the $M - H_{ap}$ curves (Fig. 5.4a), the annealing procedure sharpens the fixed layer transition and pushes the switching to the higher fields. Peaks are seen in the free layer linewidth that are associated with the fixed layer reversal. After annealing, the increase in the linewidth during reversal is diminished and the peak in the linewidth tracks the increase in switching field. A peak is also observed near the free layer reversal at zero field. There is a small reduction in this peak amplitude and a shift towards zero field after annealing.

Differences in the magnetization curves and in the curvature of the FMR frequency vs. magnetic field curves are seen after annealing in Fig. 5.4a and 5.4b due to changes in saturation magnetization M_S and in anisotropy field H_k. Figure 5.5 plots the measured M_S and H_k values as a function of annealing temperature. These parameters were obtained by fitting the resonance frequency versus magnetic field (Fig. 5.4a) to the Kittel equation

$$f_0 = \frac{\gamma\mu_0}{2\pi}\sqrt{(H_k + M_S + H_{ap}) \cdot (H_k + H_{ap})} \quad , \tag{5.1}$$

where γ is the gyromagnetic ratio. One clearly observes that annealing decreases the anisotropy field and increases saturation magnetization.

The anisotropy arises from the coupling of the fixed and free layer and reduction on annealing indicates a reduction in this coupling. The increase in magnetization may be due to the gettering of oxygen by the barrier and a subsequent increase in the moment of the adjacent magnetic layers. There is a significant change between the as-deposited sample, which undergoes a 250 °C *in-situ* anneal, and the same sample after the *ex-situ* 250 °C anneal. This may be due to the increased anneal time, a small error in the *in-situ* temperature measurement, or to the larger field

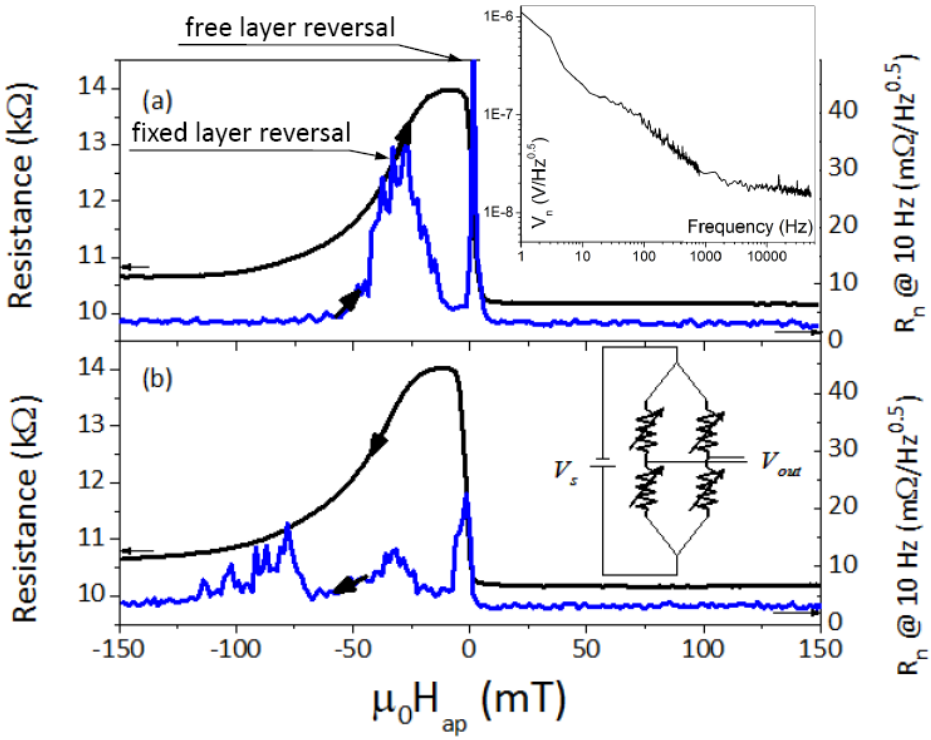

Figure 5.3: Resistance of a symmetric MTJ bridge which consists of 64 (16 MTJs per bridge leg) 10×20 μm MTJs verses applied magnetic field: (a) positive and (b) negative going branch. Also plotted is the resistance noise measure at 10 Hz of the MTJ bridge for both positive and negative going branches. The insets show the measurement geometry and the noise spectra V_n obtained by taking the average of the Fourier transform magnitude of $V_{out}(t)$ at zero applied field.

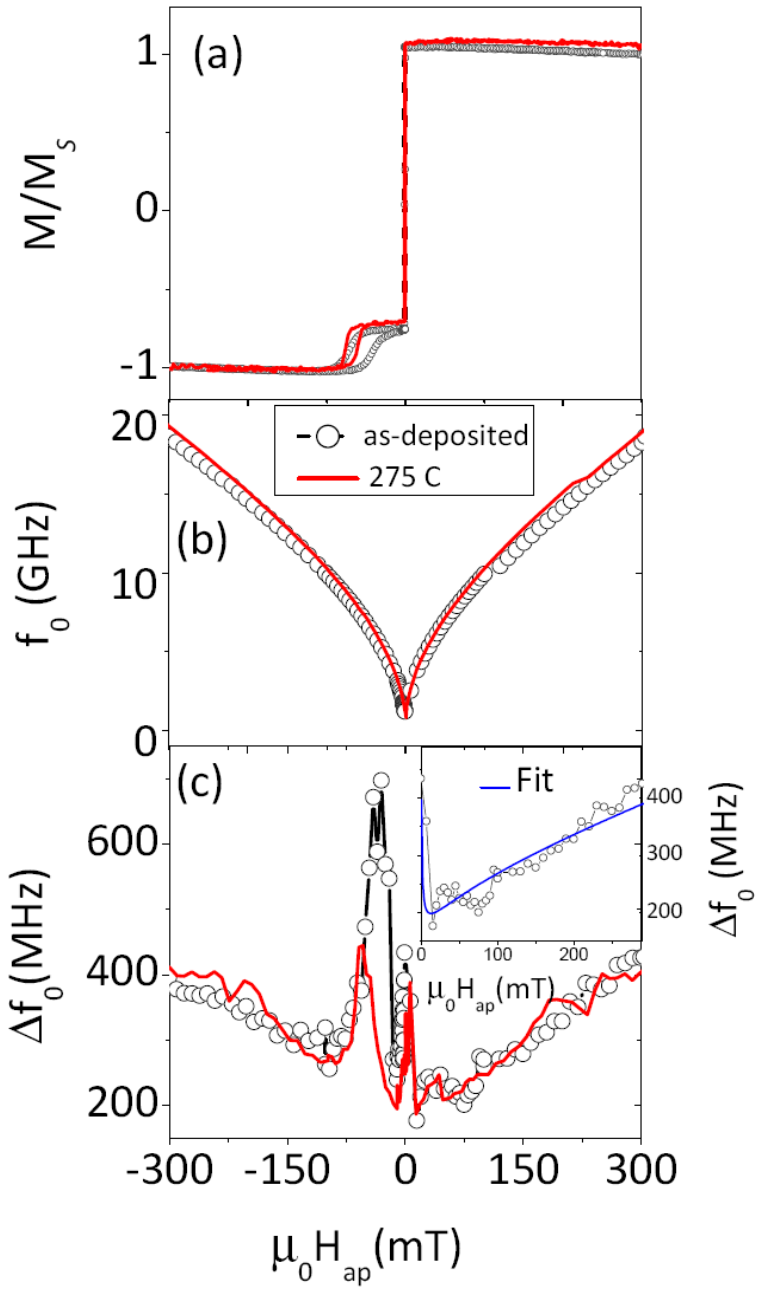

Figure 5.4: Magnetic field dependence of FMR frequency (a), magnetization (b) and FMR linewidth (c) for the as deposited and 275 °C annealed MTJs. The inset to (c) shows the fit to the linewidth data for the as deposited MTJ as discussed in the text.

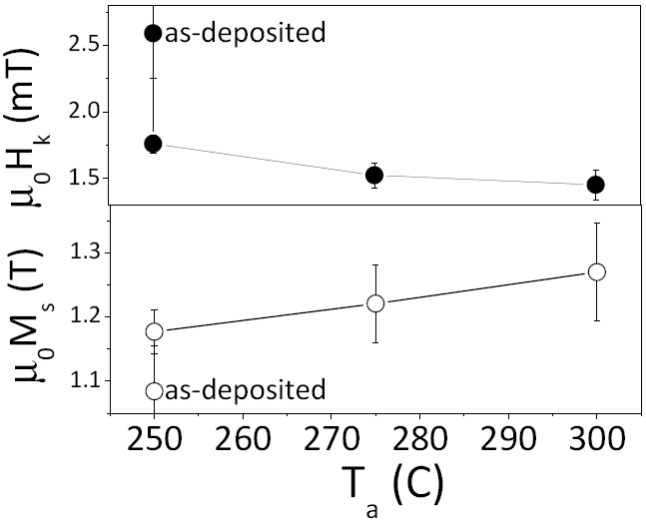

Figure 5.5: Anisotropy field H_k and saturation magnetization M_S as a function of annealing temperature determined from fits of the FMR frequency versus magnetic field data. The as-deposited MTJs, which are heated to 250 °C in the vacuum chamber, are also plotted

used in the *ex-situ* anneals. The positive field region of the linewidth can be fit, as shown in the inset of Fig. 5.4c, using a model that assumes that the linewidth is due to a combination of extrinsic broadening and intrinsic damping which is described in [112] as

$$\Delta f = \left(\mu_0 H_0 + \frac{4\pi\alpha f_0}{\gamma}\right)\frac{\gamma}{2\pi}\sqrt{1+\left(\frac{\gamma\mu_0 M_S}{4\pi f_0}\right)^2} \quad , \tag{5.2}$$

where α is the Gilbert damping parameter and H_0 is a measure of the variation in the local anisotropy field. This formula cannot fit the observed peak in linewidth near zero field. This is expected for several reasons:

1) this model assumes that the regions with different anisotropy are weakly interacting, and that the disorder is static (not a function of applied magnetic field), which is not true in this case,

2) fitting the FMR peaks is problematic when the resonance frequency gets sufficiently low that is becomes comparable to the linewidth and

3) the amplitudes of the magnetization oscillation can become quite large when the resonant frequency goes to zero.

However, fitting the data above 10 mT and using the parameters taken from Fig. 5.4 one can obtain an evaluation of $\alpha = 0.008$ and $\mu_0 H_0 = 3$ mT for the as-deposited MTJ and $\alpha = 0.008$ and $\mu_0 H_0 = 2.5$ mT for the free layer alone. We see that the

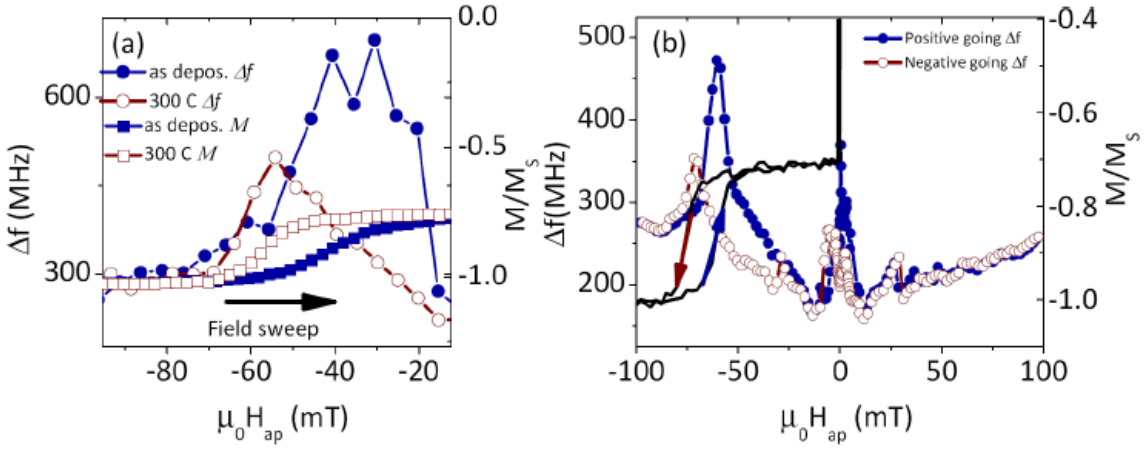

Figure 5.6: (a) Comparison of magnetization loops and free-layer linewidths in the region corresponding to the switching of the fixed layer for as-deposited and 300 C annealed MTJs. The solid arrow indicates the direction of the magnetic field sweep for all of the curves. (b) Correlation between the quasi-static magnetization loop and the FMR linewidth for the 275 °C annealed sample. Both positive going and negative going curves are shown. The horizontal thin and thick arrows represent the directions of the free and fixed layer respectively.

value of the Gilbert damping constant is consistent with what is typically measured in similar isolated Permalloy films, however, H_0 values are considerably larger than the values of 0.5 mT reported for isolated Permalloy films [112]. The H_0 values for the full MTJ are larger than those for an isolated free layer indicating that there is an additional disorder in the MTJ presumably due to the magnetostatic interactions (Néel coupling) between the fixed and free layers.

A detailed comparison between the magnetic field dependent magnetization and the FMR linewidth reveals a strong correlation between these quasi-static and dynamic characteristics. In Fig. 5.6a one can observe the behavior of the as-deposited and 300 °C annealed MTJs near the region of the fixed layer reversal for the positive going field sweep only. The increase in the sharpness of the fixed layer reversal and the decrease in the amplitude of the linewidth peak upon annealing can clearly be seen. This behavior is expected since the exchange-biased fixed layer, during reversal, provides a strong inhomogeneous magnetostatic field acting on the free layer, which gives rise to a large extrinsic linewidth as seen in other disordered systems [190].

The reduction in the linewidth indicates that the anneal has been effective in

reducing the disorder during the fixed layer reversal. Figure 5.6b shows in more details the correlation between the free layer linewidth and the quasi-static magnetization for the 275 °C annealed sample. Here both positive and negative going field branches are shown. The increase in the free layer linewidth is larger during the positive going field sweep, which corresponds to starting field scan with the fixed layer in its unfavorable orientation. This is similar to what is observed in the low frequency noise spectra and indicates that when the fixed layer starts out oriented in a direct opposite to the unidirectional bias field more disorder occurs during the reversal process. In addition, the increase in linewidth occurs well before the onset of the free or fixed layer reversals. The coercive field for free layer switching is typically 0.5 mT whereas the increase in the linewidth begins to occur at ±5 mT. This correlates with Lorentz microscopy studies reported on similar samples by *Shaw* et al. [189] that show the appearance of magnetization ripple in the free layer well before reversal occurs.

Summarizing, we found a strong correlation between the regions of increased FMR free-layer linewidth and the reversal regions of the free and fixed layer, the regions of excess 1/f noise, and the regions of large magnetization ripple in magnetic tunnel junctions.

5.4 Influence of the oxidation process

The next section describes the influence on magnetization dynamics of the interfacial properties of MTJs when a pre-oxidation process well before the insulating barrier deposition is done. With a MTJ structure similar to one described in the previous paragraph, the main difference is that a pre-oxidation on the $Co_{90}Fe_{10}$ layer (the fixed layer) was introduced during the sample grown by using two different processes:

- pre-oxidation in a O_2 atmosphere and
- pre-oxidation in an Ar plasma atmosphere.

By definition, in this section notation (OP) will denote MTJs with pre-oxidation in a O_2 atmosphere while (PP) - the MTJs pre-oxidized with plasma, and finally (ST) will denote the standard MTJs. For each type of MTJs the same *ex-situ* annealing conditions were applied : 250 °C, 275 °C and 300 °C. The experimental procedure was similar than the previous one.

Figure 5.7 compares magnetic field dependence of the quasi-static magnetization M, FMR frequency f_0, and FMR linewidth Δf_0 for the three as-deposited OP, PP and ST MTJs.

Magnetization vs. field ($M - H$) curves (Fig. 5.7a) indicate that PP-MTJs changes the fixed layer switching to the higher fields while in OP and ST MTJs the transition is more abrupt and occurs at lower fields. This is correlated with the FMR-linewidth picture (Fig. 5.7c). In the case of PP-MTJ the increase of linewidth occurs at higher fields and is smooth compared with the OP and the ST-MTJ where

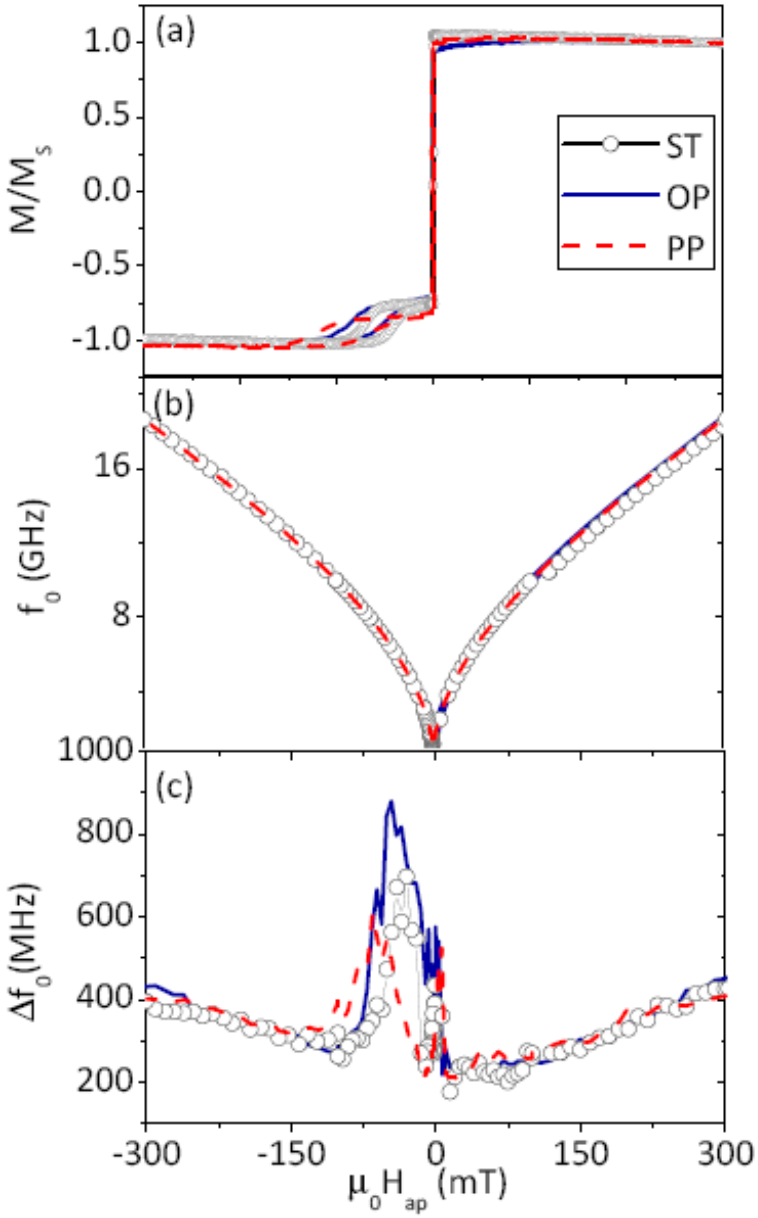

Figure 5.7: Magnetic field dependence of FMR frequency (a), magnetization (b) and FMR linewidth (c) for the as deposited ST, OP and PP MTJs.

the increase is very sharp. These effects were observed for each annealing condition except for 275 °C, where the increase of the linewidth in the regions of the free and the fixed layer reversal in OP and PP-MTJs were smoother and shown reduced values in comparison with those observed for MTJs with other annealing conditions.

Using the Eq. 5.1 one can evaluate the saturation magnetization M_S and the magnetic anisotropy H_k from the FMR data. While M_S shows similar values for all the samples studied, H_k decreases in oxidized MTJs. As was discussed in the previous section, it is most probably that the anisotropy arises from the coupling of the fixed and the free layer and therefore its reduction with pre-oxidation process could indicate a reduction in this coupling. By using the expression 5.2, the magnetic damping α and the local anisotropy field $\mu_0 H_0$ are evaluated. For an annealing condition, one can observe that while the magnetic damping has a value $\alpha = 0.008$, $\mu_0 \mathrm{H}_0$ has approximately a value similar to the isolated free layer $\mu_0 H_0 = 2.5\,\mathrm{mT}$ for PP-MTJs and is enhanced for the OP- MTJ ($\mu_0 H_0 = 3.7\,\mathrm{mT}$). This effect indicates that the additional disorder in the MTJ, presumably due to the magnetostatic interactions (Néel coupling) between the fixed and free layers, can be reduced by using a PP process, while OP looks like that induces more local defects, producing a strong Néel coupling**.** Figure 5.8 shows the FMR-linewidth for the studied annealing conditions. As an example, in panel (a) we plot the linewidth for the isolated free layer, where a lower values compared with the free layer on MTJs are observed in all the field region.

From the figures, we observe three characteristics for each annealing conditions investigated:

1) a strong enhancement in Δf_0 when the free or the fixed layer switching,

2) a shift to higher fields of the fixed layer reversal for PP process and

2) in regions near the free and the fixed switching, Δf_0 presents the greatest values for OP and the lowest for PP process.

On the other hand, observing the OP processes, an unexpected behavior is evident, as shown panels (b) and (c), where the positive field branch presents a high deviation of Δf_0 and a strong enhancement between 0 and 150 mT. This effect is an evidence of the presence of multiple impurities in the samples that have suffered this type of pre-oxidation. On the other hand, it is interesting to observe the linewidth at $T_a = 275\,^{\circ}\mathrm{C}$. We found a considerable reduction of Δf_0 in all the samples compare with other annealing conditions. Furthermore, for higher annealing temperatures ($T_a = 300\,^{\circ}\mathrm{C}$) Δf_0 suffers a strong enhancement in the reversal regions. This effect could be due to an atomic diffusion between adjacent layers, creating impurities and defects in the layers and inducing in this way an extrinsic contribution to the linewidth.

Summarizing, we observed the influence of pre-oxidation process on the quality of MTJs. We have found that a plasma pre-oxidation process, carried out well before the barrier deposition, reduces the FMR-linewidth in the regions of the free or the

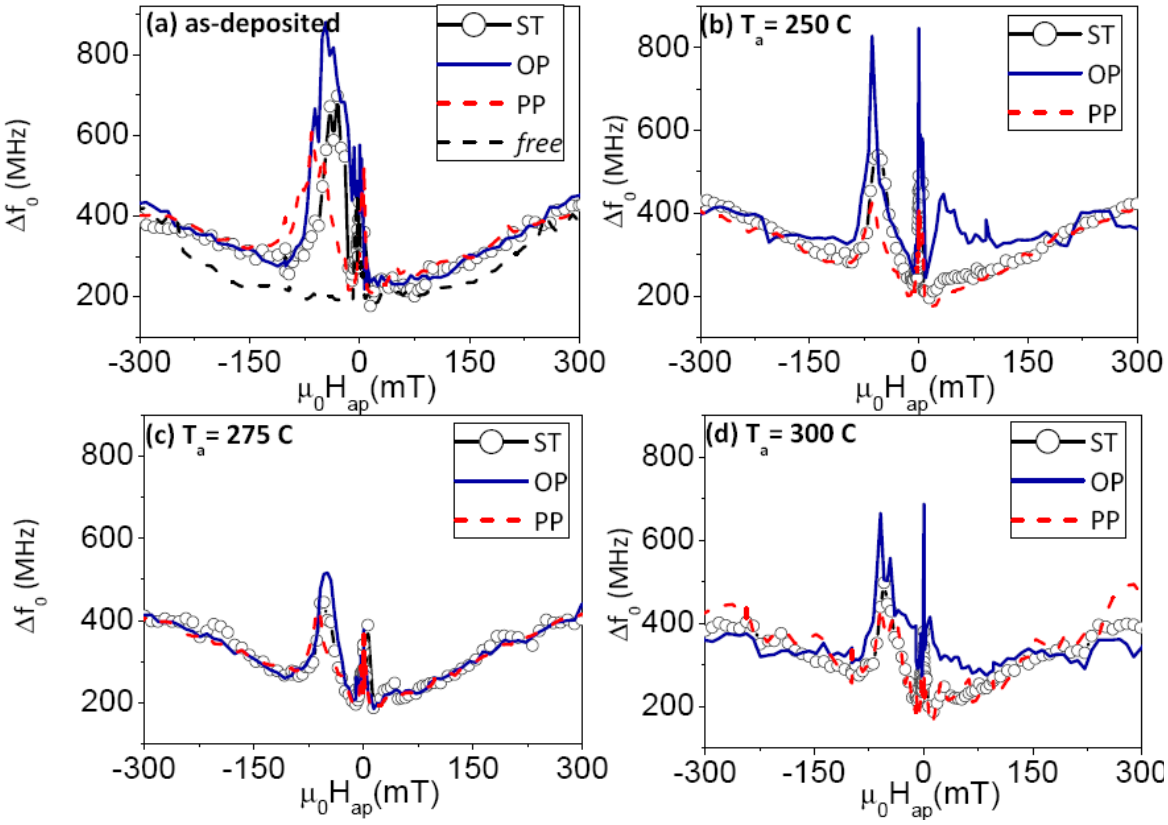

Figure 5.8: FMR linewidth on annealing condition. (a) As-deposited samples. (b) 250 °C annealed. (c) 275 °C annealed and (d) 300 °C annealed.

fixed layer reversal in comparison to standard tunnel junctions and to MTJs with O_2 pre-oxidation.

5.5 Influence of the temperature

As we mentioned in the previous sections, the MTJs under study were optimized for low field magnetic sensors applications [189]. In order to improve their low field performance, the MTJ sensors with amorphous Al_2O_3 barriers employ magnetically soft FM films typically made of Permalloy. Knowledge of the dynamic and static magnetic response of Permalloy in a wide temperature range is therefore crucial in a view of potential low temperature applications of these spintronic devices.

As was explained in Chapter 1**,** temperature dependence of the FMR measured for in-plane magnetized thin Permalloy films revealed an anomalous variation of the FMR linewidth [191] which has been attributed to spin-impurity interaction enhanced damping. More recently, enhancement of the FMR frequency in Permalloy films with decreasing temperature has been observed [192] and explained in terms of magnetization reorientation transition at the Permalloy interface with magnetization changing from in-plane to out-of-plane at temperatures below 100 K This section presents an investigation of the temperature dependence ($2\,\mathrm{K} < T < 300\,\mathrm{K}$) of dynamic and static magnetic properties of about 25 nm single Permalloy films and of Permaloy films inserted as a free layer in MTJs with Al_2O_3 tunneling barriers.

The 25 nm Permalloy film (sample A) was grown by electron-beam evaporation on standard Si(100) wafer covered by a 250 nm natural SiO_2 layer without an external magnetic field applied during deposition (for more details on sample growth and characterization see [193]). The MTJs under study were grown in the same sputtering chamber as described in the previous sections of this Chapter. The MTJs investigated had the following structure: PINNED-FM/Al_2O_3(1.8nm)/FREE-FM with PINNED-FM being exchanged biased pinned magnetic electrode composed of $Ir_{20}Mn_{80}$(10nm) /$Co_{90}Fe_{10}$(3nm). Magnetically free electrodes (FREE-FM) were $Co_{60}Fe_{20}B_{20}$(2nm)/$Ni_{80}Fe_{20}$(23nm) for sample B and $Co_{90}Fe_{10}$(3nm) /$Ni_{80}Fe_{20}$(28nm) for sample C. The entire wafers were covered with a Cu(5nm) /Ta(5nm) to prevent oxidation and were annealed at 250 C in the sputtering chamber during one hour in an applied magnetic field of 20 mT. Figure 5.9 shows an sketch of the three samples.

The low temperature FMR experiments were carried out with a commercial Agilent E5071B (ENA series) VNA working up to 8.5 GHz . For cryogenic measurements ($2\,\mathrm{K} < T < 300\,\mathrm{K}$) the variable temperature cryostat with the microwave stick developed during this thesis, situated in the Magnetrans group at the Autonomous University of Madrid[1] was used. The data analysis is based, as described

[1]For more details on the low temperature RF magnetometer see Chapter 2.

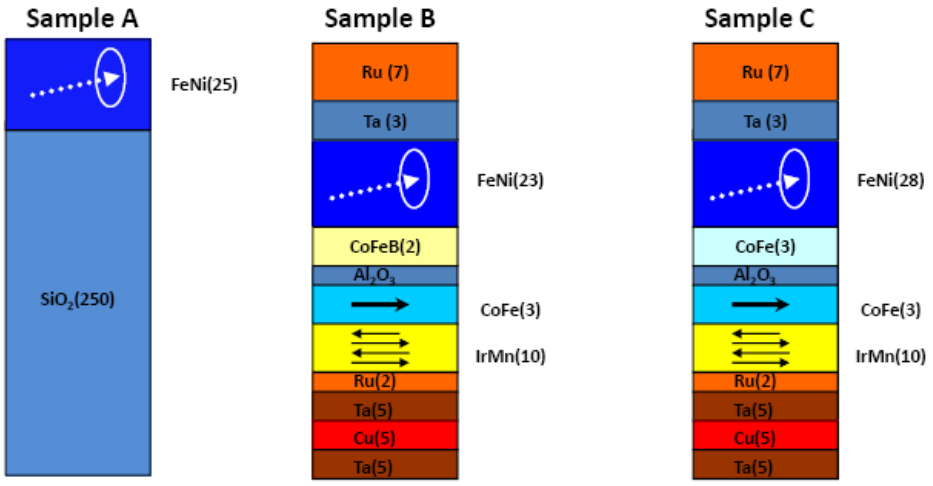

Figure 5.9: Sketch showing the structure of the 3 samples investigated. The thickness of the layers is in nm.

in the previous sections, on the method developed by *Kalarickal* et al. [112]. The resonance frequency f_0 and linewidth Δf_0 were evaluated by fitting the resonance peaks to a lorentzian curve. A reference spectrum was measured at $\mu_0 H_{ap}$= 0.2 T for all the fields scans. On the other hand, the magnetization was measured as a function of applied magnetic field up to 0.5 T using a SQUID magnetometer with a temperature range from room temperature to 5 K (in collaboration with Dr. M. Garcia, ICMM-CSIC-Cantoblanco, Madrid). In addition, in collaboration with Dr. E. Snoeck (CEMES- CNRS, Toulouse, France) structures of the different layers and interfaces were investigated at room temperature by transmission electron microscopy (TEM).

Figure 5.10 shows the loss profile, i.e. the imaginary part of microwave permeability parameter U(f) [112] and compares the magnetic field dependence of the FMR frequency measured at 150 K and 10 K for the three samples investigated. One clearly observes a strong variation of $f_0(H)$ with decreasing temperature for samples A and C.

In order to describe in greater detail the temperature dependence of the FMR, Fig. 5.11 compares the resonant frequency f_0(T) and the linewidth $\Delta f_0(T)$ for samples A-C determined with $\mu_0 H_{ap} = 20mT$. A strong temperature variation of the resonance peak and the linewidth is observed for sample A and C below about 80 K and 50 K respectively. We note that sample B presents, however, only weak (<5%) enhancement of the FMR frequency but with a relevant (about 30%) decrease of the FMR linewidth below 60 K.

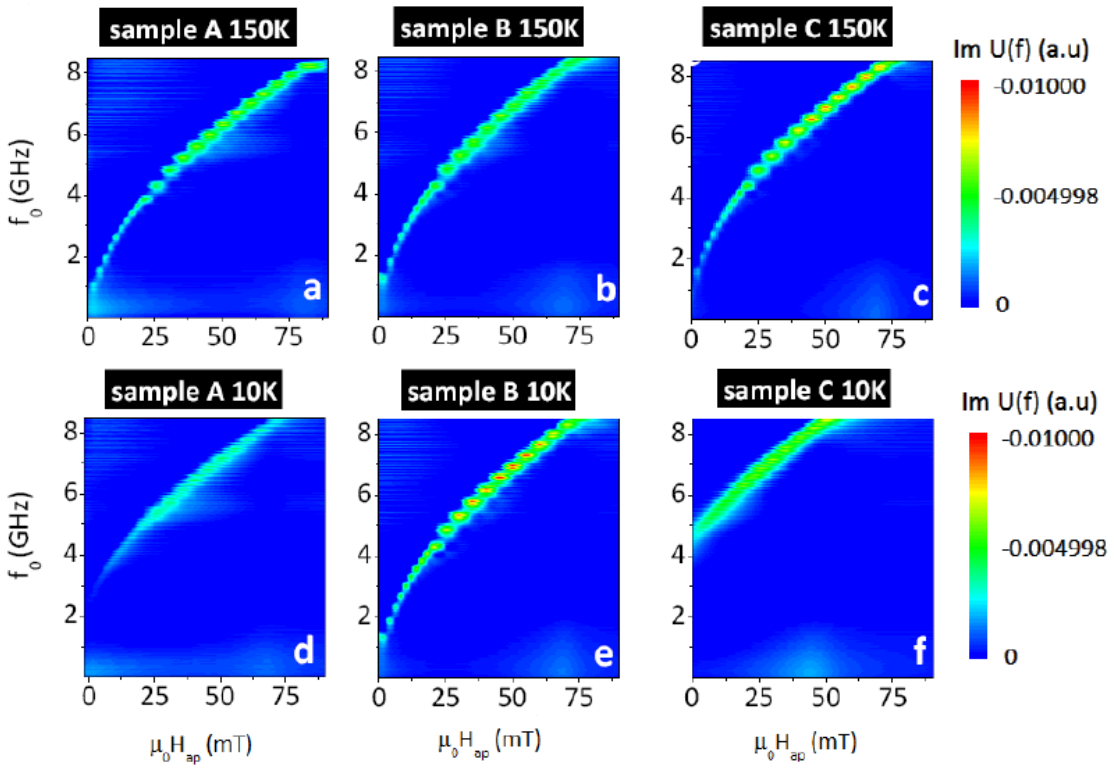

Figure 5.10: 3D contour plot of the FMR at different external bias fields. The pictures show the loss profiles. The top panel (a-c) shows resonant frequency $f_0(H)$ measured at 150 K while the bottom panels (d-f) show $f_0(H)$ at $T = 10$ K.

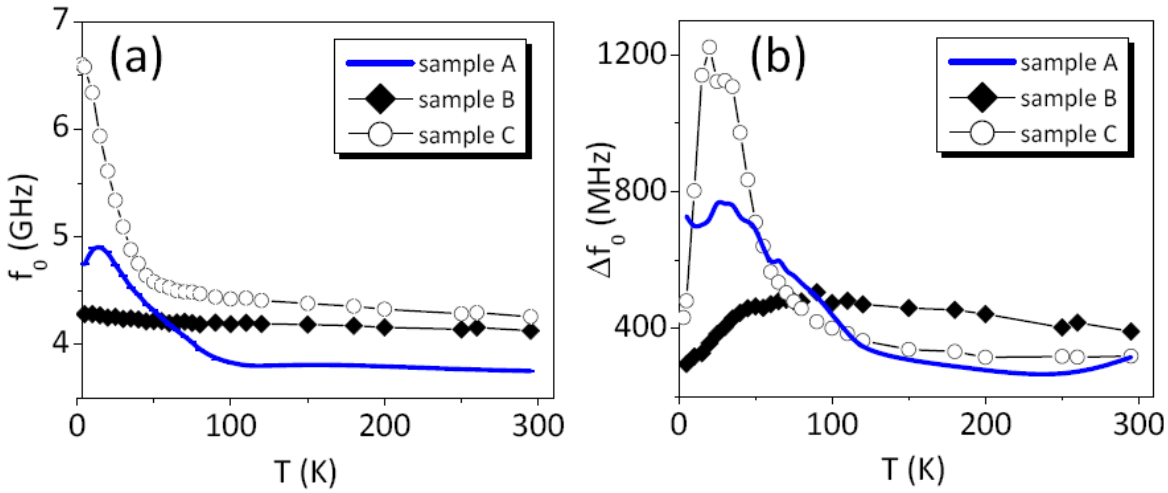

Figure 5.11: Temperature dependences of the FMR frequency (a) and the FMR linewidth (b) measured for samples A-C with an applied field of 20 mT.

One can determine the variation in the magnetic properties of Permalloy from the FMR measurements by estimating the in-plane magnetic anisotropy H_k as a function of temperature. This is done by fitting the uniform resonance mode to the Kittel equation (Eq. 5.1). It was found that the M_S obtained is practically independent of temperature and showed nearly the same value for all three samples investigated for which $M_S \sim 1$ T. The estimated anisotropy field H_k, however, shows a much stronger dependence on the temperature, especially noticeable for samples A and C at low temperatures (see Fig. 5.12a).

Figure 5.12b illustrates an example of the magnetization curve for the sample C with three different regions clearly distinguished for parallel (P) and antiparallel (AP) alignment of the FREE-FM and PINNED-FM layers. One may also analyze the hysteresis loop of the FREE-FM layer (see inset of Fig. 5.12b) in order to determine the corresponding coercive field H_c of the FREE-FM layer as a function of temperature. Besides, knowledge of $M - H$ curves allows us to evaluate the temperature dependence of the total magnetization in the applied field of 0.5 T (further called M_S^*). As to the coercive field, one clearly observes that in both types of MTJs the H_c is substantially lower than what is observed for the plane Permalloy film. This strong difference could be due to the influence of dipolar fields created by domain walls in the hard layer and which originated from the exchange-biased fixed layer on domain wall nucleation and propagation in the free Permalloy layer. As for the temperature dependence of the high field magnetization, for all samples studied the $M_S^*(T)$ normalized by the value $M_S^*(0.5\,\mathrm{T})$ is close to 1, except in proximity to the temperature interval around 50-60 K where a clear anomaly in $M_S^*/M_S^*(0.5T)$ is

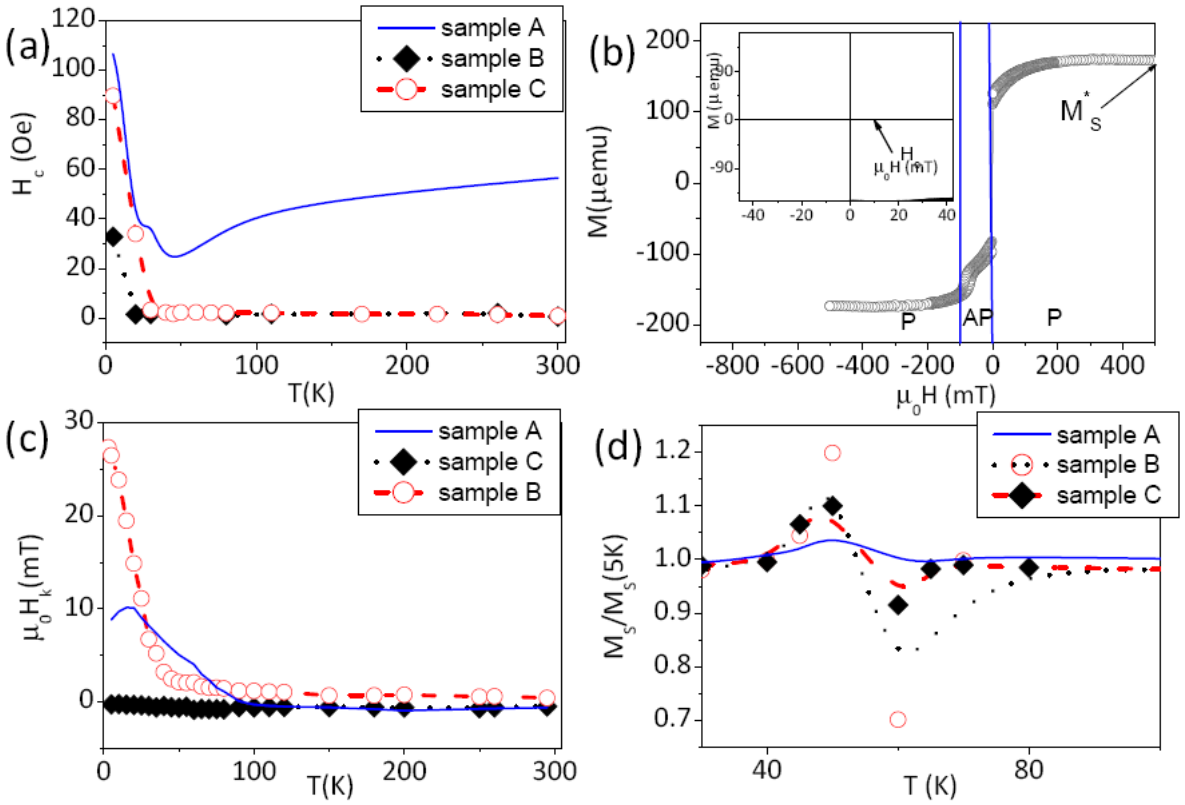

Figure 5.12: (a) Temperature dependence of the coercive field H_c for A-C samples. (b) Typical magnetization vs. magnetic field curve of the MTJs studied. The curve corresponds to sample C at $T = 170\,\mathrm{K}$. Three different regions are observed (see text). P (AP) denote parallel (antiparallel) alignment between free and fixed electrodes. The value of $M_S^*(0.5\,\mathrm{T})$ is marked in the figure. (c) Temperature dependence of the anisotropy field H_k evaluated by using the Kittel equation. (d) Temperature dependence of the$M_S^*(0.5\,\mathrm{T})$ normalized by M_S^* at 5 K. The curve is shown around the critical temperature $T_C = 60\,\mathrm{K}$.

observed (Fig. 5.12d).The differences in the form of this anomaly in $M_S^*/M_S^*(0.5T)$ between samples A-C, which evidences an orientation magnetic transition (OT), will be discussed below in contest of the OT at surface of free or coupled through barrier by dipolar fields Permalloy films.

The above experimental results show evidence for the possible magnetic orientation transition due to in Permalloy films at low temperatures. As we have already mentioned, the temperature dependent FMR in Permalloy films reported previously [192], who suggested that the main effect of temperature on the magnetic properties of Permalloy films is increasing the in-plane uniaxial anisotropy and inducing a surface anisotropy that pushes the magnetization out-of-plane. Here we not only confirm this observation (for Permalloy film) but furthermore demonstrate that the magnitude of the change in the dynamic response at low temperatures is determined by the type of the material interfacing with Permalloy.

Below we describe a simple qualitative model which seems to explain the main experimental observations. Following suggestions [192] we attribute the changes in FMR and in magnetization in both free Permalloy film and MTJs with Permalloy below 60 K to reorientation (from in-plane to perpendicular to the interface) transition of magnetic moments at the Permalloy interface (Fig. 5.13c) sketches shows only magnetizations changes in Permalloy). Under the assumption that the surface anisotropy energy is determined by the Permalloy interface stress, our data could suggest that MTJ with the CoFeB/Permalloy interface (sample B) is more relaxed than the corresponding interface in the CoFe/Permalloy system (sample C). Indeed it has been recently reported [194] that similar MTJ FREE-FM electrodes have qualitatively different Al_2O_3/CoFe/Permalloy and Al_2O_3/CoFeB/Permalloy interfaces. While no Fe-O segregation in CoFeB layer was observed when CoFeB was deposited on Al_2O_3 barrier, the CoFe layer was found to present some Fe-O and Co segregation on the top of the barrier which could be responsible for enhanced interface stress, increasing the surface anisotropy in the CoFe/Permalloy interface and producing largest variations of the temperature dependence of dynamic properties.

We note that such a possibility is also corroborated by the TEM on MTJs. Figures 5.13a and 5.13b show TEM images of samples B and C respectively.

From these images one may conclude that the CoFeB layer has a better quality than the CoFe layer where segregation and partial intermixing with the Permalloy layer could occur. Indeed, for sample C one observes dark areas which might indicate that the Co layer is a consequence of segregation close to the Al_2O_3/CoFe/Permalloy interface (Fig. 5.13b).

Let us finally discuss possible origin of unusual upward/downward dependence of normalized magnetization $M_S^*/M_S^*(0.5T)$ observed in MTJs (samples B and C). Looking at in $M_S^*/M_S^*(0.5T)$ curves one sees a qualitative difference in the behavior for the samples B and C (MTJs) in comparison to sample A (Permalloy film). Indeed, samples B and C show a similar dependence of $M_{\mathbf{S}}^*(T)$ although magnitude

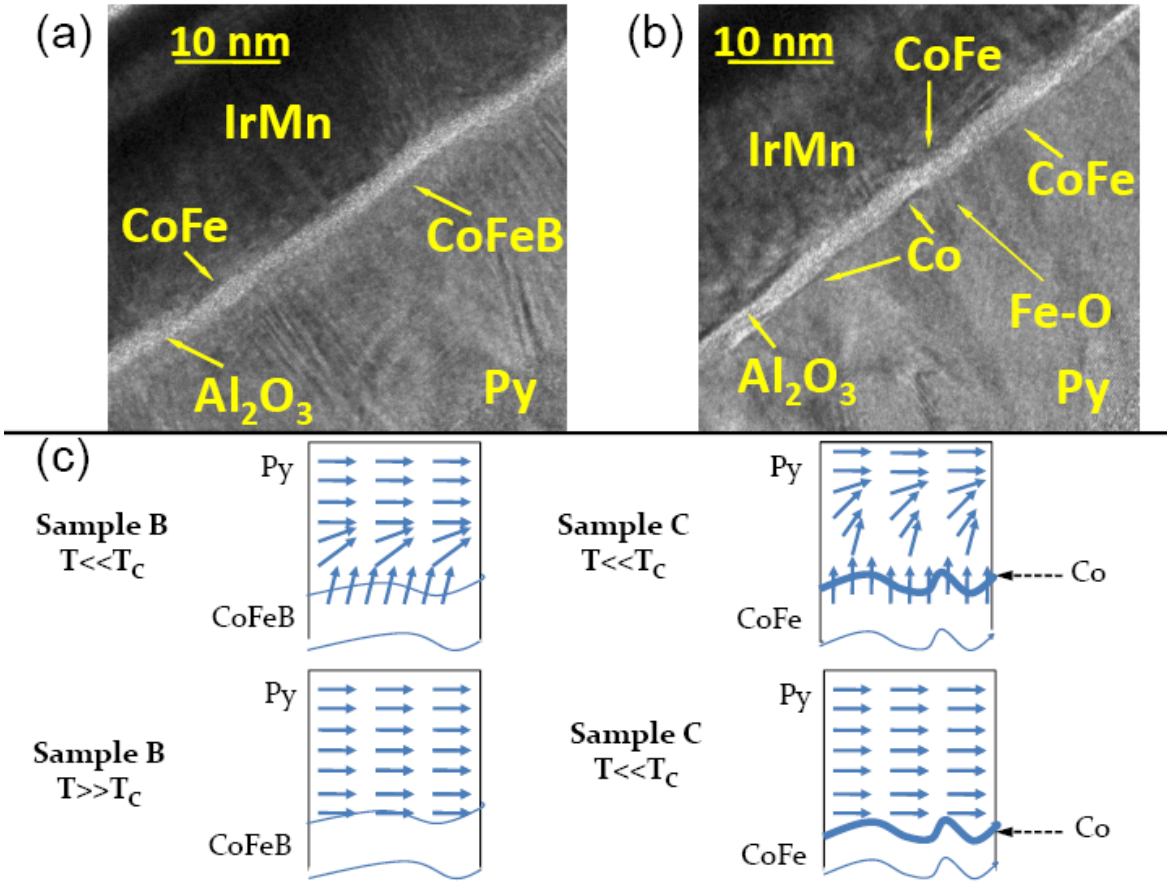

Figure 5.13: (a)TEM image of the sample B with CoFeB/Permalloy FREE-FM layer. One can clearly distinguish the CoFeB/Permalloy interface. (b) TEM image of the sample C with CoFe/Permalloy FREE-FM layer where dark and white areas are observed along the Al_2O_3/CoFe interface. Dark areas may correspond to the Co precipitation. In addition one may observe the Fe-O segregation in the FREE-FM layer. (c) Sketch explaining the model of the reorientation transition at the Permalloy interface due to the surface anisotropy.

of upward/downward peaks close to $T_{\mathbf{C}} \sim 60\,\mathrm{K}$ being rather different, which also strongly correlates with corresponding variation of FMR frequency at low temperatures. At the same time, sample A shows only a very weak upward (maximum) in $M_S^*/M_S^*(0.5T)$ close to $T_{\mathbf{C}}$ with some variation of the FMR at low temperatures.

Qualitatively different variation of $M_{\mathbf{S}}^*(T)$ in the Permalloy and MTJs could indicate some qualitative differences in their ground state magnetic configuration. In order to understand this qualitative difference of $M_{\mathbf{S}}^*(T)$ curve for MTJs and Permalloy film we suggest some modification of the previously introduced model (which seems to be appropriate only for Permalloy films) to take into account close proximity to other (hard) ferromagnetic layer to soft Permalloy layer.

In order to understand the upward/downward behavior in the $M_{\mathbf{S}}^*(T)$ curve with only 20% enhanced/de-enhanced of the in-plane magnetic moments close to $\mathrm{T}_{\mathbf{C}}$ in MTJs we suggest mutual influence of the pinned (hard) layer and the free (soft) one, induced by some antiferromagnetic coupling in some regions presenting anticorrelated roughness [195] through "orange-peel" coupling mechanism.

It is well known (see Chapter 1) that for a correlated roughness between the ferromagnetic layers interfacing the insulating barrier a parallel magnetization configuration due to the "orange-peel" coupling is preferred. However, the regions with anticorrelated roughness should be expected to favour an antiparallel coupling due to dipolar effects in MTJs [195]. Our analysis below shows presence and influence of this antiparallel coupling on $M_{\mathbf{S}}^*(T)$.

As shown in Fig. 5.14, when the total MTJ structure is saturated at low temperatures ($T << T_C$), some regions of the soft and hard layers interfacing Al_2O_3 barrier have their magnetic moments out-of-plane due to the surface anisotropy in Permalloy and dipolar coupling. This means that both magnetic moments are occupying a relative minimums of energy, corresponding to an out-of-plane magnetization. "Spring" sketches dipolar coupling between hard and soft layers (Fig. 5.14a). Close to the T_C ($T \leq T_C$) (Fig. 5.14b) the soft layer starts to suffer the orientation transition from out-to-plane to in-plane alignment, creating a time dependent component that enhance the magnetization, moving the soft ferromagnetic system (Permalloy) toward its global minimum (i.e. in-plane magnetization) and therefore enhancing $M_{\mathbf{S}}^*(T)$ value. Figure 5.14c sketches what happens at $T \geq T_C$ when the hard layer, due to its coupling to the soft layer and due to the strong difference in the metastable energy profiles, is pushed toward in-plane (trending to be antiparallel to the soft layer) magnetization configuration, reducing the total effective value of $M_{\mathbf{S}}^*(T)$. As we have already underlined above, the values of $M_{\mathbf{S}}^*(T)$ close to $T_{\mathbf{C}}$ do not correspond to equilibrium magnetization values. Finally, at $T >> T_C$ (Fig. 5.14d) both soft and hard layers have in-plane magnetization (both "balls" are occupying their absolute minimum of energy) in equilibrium conditions with an antiparallel alignment showing a total magnetization of the stack nearly the same as at $T \longrightarrow 0$.

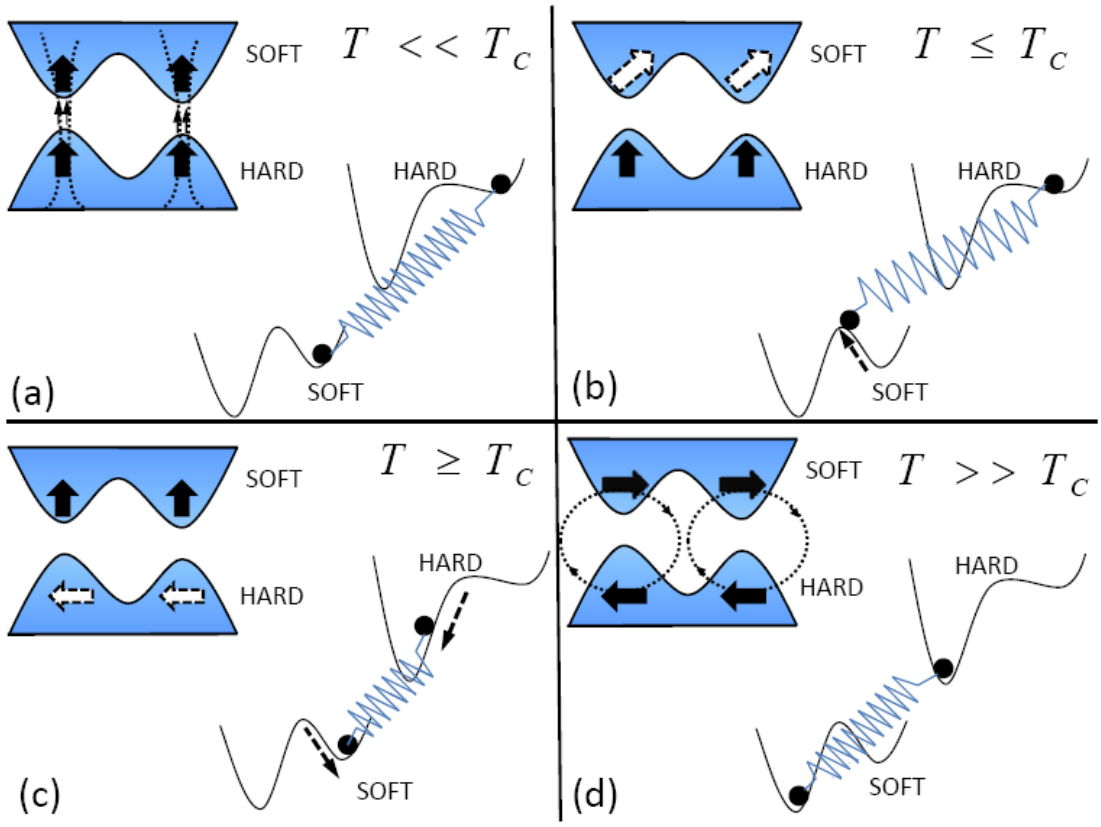

Figure 5.14: Sketch explaining proposed magnetization configuration and the energy profiles of both soft and hard layers in the regions with anticorrelated roughness. Relative and absolute minima correspond to out-of-plane and in-plane magnetizations respectively for: (a) $T << T_C$. (b) $T \leq T_C$. (c) $T \geq T_C$ and (d) $T >> T_C$ conditions. Dot lines indicate the magnetic field lines. Dashed arrows indicate non-equilibrium character of magnetization.

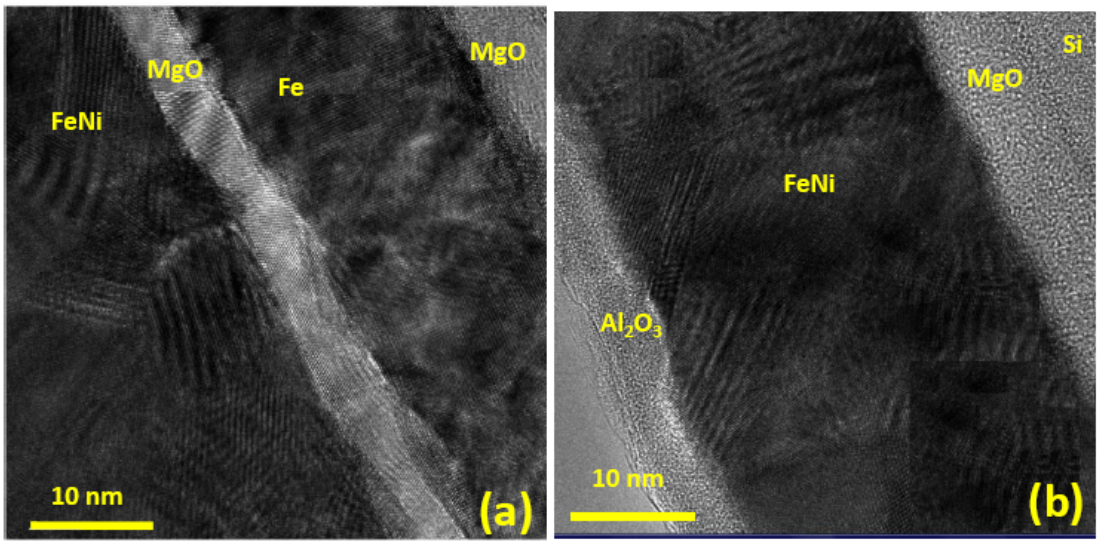

Figure 5.15: (a) TEM image of sample D. (b) TEM image of sample E. Both MTJs samples have MgO barrier.

In order to verify a possible influence of the type of the insulating material on static and dynamic characteristic of Permalloy at low temperatures we have grown, in collaboration with J. Moodera group (Francis Bitter Magnet Laboratory - MIT, USA), two additional epitaxial samples. The first one with the structure: Si(<100>) /MgO(10 nm) /Fe(20 nm) / MgO(2.5 nm) / $Fe_{20}Ni_{80}$(30 nm) / Al_2O_3(5 nm) (sample D) being $Fe_{20}Ni_{80}$(30 nm) the FREE-FM layer and Fe(20 nm) the FIXED-FM layer. The second one has the structure Si(<100>) /MgO(10 nm) /$Fe_{20}Ni_{80}$(30 nm) / Al_2O_3(5 nm) (sample E), i.e. isolated $Fe_{20}Ni_{80}$(30 nm) grown on MgO.

Both samples are covered by a Al_2O_3 insulating layer and were analyzed using TEM images shown in Fig. 5.15.

TEM images of the sample D show a highly crystalline MgO/Fe/MgO/FeNi stacking with large Fe grains of about 15 nm. The growth directions are [001] for the two MgO layers and for the Fe one, while the FeNi layer seems to be [111] textured. The MgO insulating barrier presents a roughness of about $1-2$ nm. On the other hand, the TEM images of the sample E, indicate that the MgO layer is epitaxial. The FeNi layer is polycrystalline without any evidence of a high texture.

We have investigated the magnetization dynamics properties (f_0 and Δf_0) vs. temperature and compared with results obtained for samples A-C. Fig. 5.16 shows

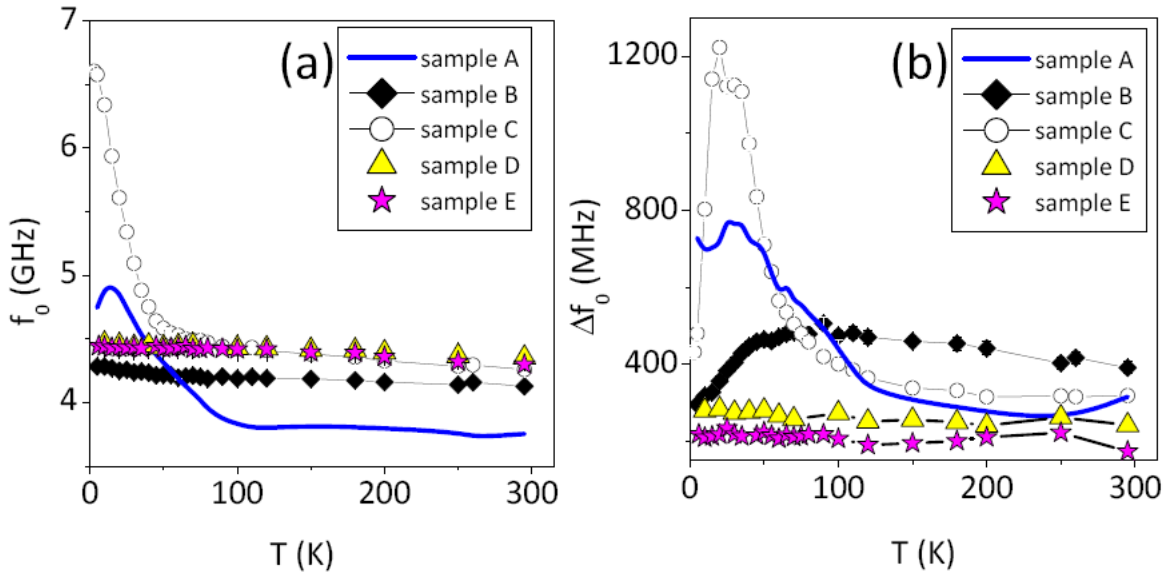

Figure 5.16: (a) Temperature dependence of the FMR for all samples studied (b) Temperature dependence of the linewidths for all the samples under study. The external bias field was 20 mT

the temperature dependence of f_0 and Δf_0 for samples D and E for an external bias field of $\mu_0 H_{ap} = 20\,\mathrm{mT}$. Within 4%, we have not found a significant temperature dependence of the FMR, but is interesting to observe the reduced value of Δf_0 in all the temperature range investigated for samples D and E. This reduced value may be due to the high quality of the samples, the reduction of the Néel coupling and a reduction of defects in Permalloy layers when are deposited epitaxially on MgO layers.

Summarizing we have investigated the influence of the temperature on the dynamic and static responses of different magnetic nanostructures with Permalloy thin layers. We detected a magnetization reorientation transition in the Permalloy interface at T about 60 K due to the enhancement of the surface anisotropy. We have observed that orientation transition may be modified in MTJs depending on the interface components. We have put forward simple qualitative model to explain main experimental observations.

5.6 Conclusions

Chapter 5 has described three main findings:

1. From magnetization dynamics studies on magnetic tunnel junctions we have

found a strong correlation between the regions of increased FMR free-layer linewidth and 1) the reversal regions of the free and fixed layer determined by quasi-static magnetization measurements, 2) the regions of excess 1/f noise, and 3) the regions of large magnetization ripple. The regions of increased linewidth, as with the regions of increased 1/f noise, are history dependent, i.e. depend on the starting state of the MTJ. The increase in linewidth occurs well before the onset of the observed transition in the magnetization and the increase in linewidth is substantially greater in the MTJ than in a corresponding isolated free layer. We have shown therefore that increase in the FMR linewidth is a simple and effective method of monitoring the disordered magnetic structure, interfacial roughness, and the improvement during the annealing process. Hence, we demonstrate that study of the FMR linewidth of the free layer of MTJs may be a useful diagnostic on the quality of the MTJs being developed for a variety of applications.

2. We have investigated the effects of pre-oxidation processes in the quality of MTJs observing that a plasma pre-oxidation process well before the barrier deposition reduces the FMR-linewidth in the regions where the free or the fixed layer reversal compare with O_2 pre-oxidation and standards tunnel junctions.

3. Finally, the temperature dependence of the static and dynamic magnetic properties of separately grown Permalloy films and Permalloy incorporated as free layer in MTJs indicate a reorientation magnetic transition at the Permalloy interface below 60-100K due to surface anisotropy of Permalloy. In order to understand qualitative difference in magnetization of MTJs and Permalloy films at low temperatures we discuss possible influence of the Néel or "orange peel" coupling of dynamic and static properties. These findings could be important for low temperature applications of devices incorporating Permalloy and especially for the MTJs with perpendicularly aligned soft and hard layers which are expected to develop maximum field sensitivity [196].

Chapter 6

General Conclusions

This thesis has presented a detailed investigation of the magnetization dynamics in magnetic and superconducting nanostructures with and without lateral nanostructuring in a wide range of frequencies and temperatures.

The novel rectification effect due to the vortex dynamics in type-II superconductor films have been presented in **Chapter 3**. Plain and nanostructured films with different shapes (strip and cross shapes) have been investigated from 9 kHz up to 147 MHz. We have observed two different regimes in the rectification: low and high frequency regimes.

The main difference between low and high frequency rectification regimes appears to be in the symmetry and value of the rectified DC voltage. In the low frequency range the rectified DC voltage shows one-dimensional symmetry while a two-dimensional character of the DC rectification voltage is observed in the high frequency range. We have verified and dismissed the critical current anisotropy a possible reason for the high frequency rectification by measuring the I-V characteristics.

In the case of plain films the rectified voltage changes polarity with changing the direction of the magnetic field. Moreover, measurements in the strip shape samples along the same borders of the strip show a permanent electric field being strongly inhomogeneous along the strip edge.

In the case of artificially nanostructured films the stronger vortex pinning increases the critical current and lowers the rectified voltage in about an order of magnitude. Far below the critical temperature we have observed changes in the polarity of the rectified voltage not only with changing the direction of the magnetic field as in the plain films, but also when the intensity of the magnetic field crosses the matching fields.

We have proposed two possible theoretical models which qualitatively explain the main experimental results. The first one is based on a surface barrier model (Bean-Livingston model) and the second one is based on Meissner currents induced

geometric barrier model. These tentative ideas explain this phenomenon, which irrespective of its explanation should be taken into account in experimental studies of rectification effects in superconductors.

Chapter 4 presents studies of the static and dynamics properties of the magnetization in arrays of Permalloy dots varying the interdot distance form 1.2 μm to 2.5 μm. From the static magnetic properties we have verified the presence of a topological magnetic anomaly, i.e a vortex configuration forming in the ground state. We have characterized the nucleation and annihilation magnetic fields. With two different excitation schemes, with RF pumping and bias fields along the dot plane and being parallel or transverse to each other and by using newly developed a vector network analyzer broadband magnetometer, we have investigated the magnetization dynamics in saturated in-plane and in the vortex states. We have detected and identified two types of the spin waves when the dots are in-plane saturated: the uniform Kittel mode and other spin wave interpreted as a magnetostatic backward volume mode appearing due to the quantization of the spin wave vector. Detailed analysis shows that the dipolar coupling between dots slightly reduces the resonance field of both modes. Moreover, the detailed analysis of the linewidth of the uniform mode in the saturated state close to the vortex state formation regime have revealed its remarkable increase when approaching to the magnetic vortex nucleation.

The investigation of a possible angular dependence of the in-plane resonance fields confirms the presence of a weak magnetic anisotropy in the samples where the interdot distance becomes less or comparable to the dot diameter.

We have detected and investigated the high frequency (GHz) modes in the vortex state regime as a function of the external bias field and with different (parallel and transverse) pumping schemes. Multiple SW resonances in the metastable state and near the zero field have been observed. With both parallel and transverse schemes the first azimuthal mode AM (n=0; m=$\pm$1) was found to be strongly split with eigenmode frequencies varying quadratically with the external bias field in the stable vortex regime. The large splitting of the low lying azimuthal mode could be a consequence of the hybridization of these modes with the gyrotropic mode.

Finally, the **Chapter 5** presents the experimental results on the influence of annealing, oxidation and temperature on the magnetization dynamics in the magnetic tunnel junction with a free ferromagnetic Permalloy electrode and with amorphous Al_2O_3 insulating barriers.

We have found a strong correlation between the regions of the increased ferromagnetic resonance free-layer linewidth and the reversal regions of the free and fixed layer determined by quasi-static magnetization measurements. Measurements of the 1/f noise presents an excess of noise in the reversal regions. We have investigated the possible influence of the magnetic field history, i.e dependence on the initial state in the MTJs and observed a substantial reduction of the linewidth depending on if the field was increased or decreased close to magnetization reversal transition.

We have investigated the effect of the oxidation just before the barrier deposition on the quality of magnetic tunnel junctions by using magnetization dynamic studies up to 20 GHz at room temperature. Two types of oxidation were done: O_2 and plasma oxidation. For the second type of the process we have observed a reduction of the linewidth in the regions where free or fixed layer are reversed. This could indicate a reduction of the layer roughness with plasma oxidation.

The temperature dependence of the static and dynamic magnetic properties of separately grown Permalloy films and Permalloy incorporated as free layer in magnetic tunnel junctions have been studied down to 5K. We have observed an anomaly in the dynamic properties in Permalloy films near 60K. In the case of magnetic tunnel junctions the anomaly in the dynamics properties depends on the free layer composition. These anomalies indicate a reorientation magnetic transition at the Permalloy interface. From the static properties we have observed qualitative differences between dynamics and static magnetic response in free Permalloy films and for Permalloy in tunnel junctions. In order to account for main observations we consider a possible influence of the hard layer coupled antiferromagnetically to the free one due to an anticorrelated roughness between the magnetic layers interfacing the insulating barrier.

Chapter 7

Conlusiones generales

Esta tesis ha presentado una investigación detallada de la dinámica de la imanación en nanoestructuras magnéticas y superconductoras con y sin nanoestructuración en un amplio rango de frecuencias y de temperaturas.

En el **Capitulo 3** se ha presentado el nuevo efecto de rectificación debido a la dinámica de los vórtices en superconductores de tipo-II. En un rango de frecuencias que comprende de los 9 kHz hasta 147 MHz se han investigado películas con diferentes formas (forma de cruz y de tira) con y sin nanoestructuración. Hemos observado dos regimenes en la rectificación: de baja y de alta frecuencia.

La principal diferencia entre ambos regimenes parece ser la simetría y el valor del voltaje DC rectificado. En el rango de baja frecuencia el volatje DC rectificado muestra una simetría unidimensional mientras que en el rango de alta frecuencia la simetría es bidimensional. Por otro lado hemos verificado y descartado que ésta rectificación proceda de la anisotropía en la corriente crítica.

En el caso de películas sin nanoestructuración, el voltaje rectificado cambia de polaridad cuando se invierte la dirección del campo magnético aplicado. Además, las medidas en las muestras con forma de tira muestran un campo eléctrico permanente sumamente inhomogéneo a lo largo del borde de la tira.

En el caso de las películas nanoestructuradas, el fuerte anclaje de los vórtices incrementa el valor de la corriente crítica y disminuye el valor del voltaje rectificado un orden de magnitud. Lejos de la temperatura crítica de las películas hemos observado cambios en la polaridad del voltaje rectificado no solo cuando se ha cambiado la dirección del campo magnético aplicado sino también cuando el campo magnético cruzaba los campos de anclaje de vórtices.

Hemos propuesto dos posibles modelos teóricos que cualitativamente expliquen los principales resultados experimentales. El primero esta basado en un modelo de barrera superficial (modelo de Bean y Livingston) y el segundo está basado en un modelo de barrera geométrica con corrientes Meissner inducidas. Estas ideas tentativas explican éste fenómeno, el cual independientemente de su explicación, debe de tenerse en cuenta en los estudios experimentales del efecto de rectificación

en superconductores.

El **Capitulo 4** ha presentado el estudio de las propiedades estáticas y dinámicas de la imanaión en redes rectangulares de puntos magnéticos de Permalloy variando la distancia entre puntos de 1.2 μm a 2.5 μm. De las propiedas estáticas de la imanación hemos verificado la presencia de una anomalía topológica magnética, i.e la formación de un vórtice magnético en el estado fundamental. Hemos caracterizado los correspondientes campos de nucleación y de aniquilación de estos vórtices en las distinatas muestras.

Con dos diferentes esquemas de excitación, con el campo de excitación rf y el campo magnético aplicado en el plano de los puntos y estando en una configuración paralela o perpendicular entre ambos, hemos investigado la dinamica de la imanación cuando los puntos presentaban su imanación saturada en el plano y en estado vórtice. Para ello hemos usado una nueva técnica basada en un magnetómetro de banda ancha detectando la señal con un analizador de redes vectorial.

Cuando los puntos tienen su imanación saturada en el plano hemos detectado dos tipos de ondas de espín: el modo uniforme de Kittel y una onda de espín que ha sido interpretada como un modo magnetostático de volumen, que aparece debido a la cuantización del vector de onda de espín. Un análisis detallado, muestra que el acoplo dipolar entre los puntos reduce levemente el campo de resonancia en ambos modos. Además, el estudio del ancho de línea del modo uniforme cuando la imanación estaba saturada en el plano muestra un incremento notable cuando el campo magnético aplicado se aproxima al valor del campo de nucleación de los vórtices.

El estudio de una posible dependencia angular de los campos de resonancia ha confirmado la presencia de una anisotropía débil en las muestras donde la distancia entre los puntos era menor o comparable al diametro del puntos.

Hemos detectado e investigado los modos de alta frecuencia en el estado de vórtice con diferentes esquemas de excitación (esquema paralelo y perpendicular de campos). Se ha observado múltiples ondas de espín resonantes en el estado metaestable y cerca de campo magnético cero. Con ambos esquemas se ha observado que el primer modo azimutal se desdobla con una variación cuadrática de la frecuencia con respecto al campo magnético cuando el vórtice es estable. Este gran desdoblamiento del primer modo azimutal puede ser una consecuencia de la hibridación de este modo con el modo girotrópico.

Finalmente, el **Capitulo 5** ha presentado los resultados experimentales de la influencia de tratamientos térmicos de recocido, oxidación y temperatura en la dinámica de la imanación en uniones túnel magnéticas con un electrodo magnéticamente blando de Permalloy y con barreras aislates amorfas de Al_2O_3.

Hemos encontrado una fuerte correlación entre las regiones donde el ancho de la línea de la resonancia ferromagnética de la capa blanda incrementa su valor y las regiones donde la capa blanda o dura invierte la dirección de su imanación. El

estudio de la posible influencia de la historia magnética, i.e la dependencia con el estado inicial de la unión túnel magnética, nos ha permitido observar una reducción en el ancho de la línea cerca de las regiones de campo magnético donde se produce la inversión de la imanción en la capa dura o blanda, dependiendo de si el campo magnético aplicado aumentaba o disminuía su valor.

Hemos estudiado el efecto de la oxidación cuando ésta se aplica justo antes de depositar la barrera túnel en la calidad de la uniones. Para ello hemos estudiado la dinámica de la imanación a temperatura ambiente hasta 20 GHz. Las oxidaciones han sido de dos tipos: oxidación con O_2 y con plasma. Para el segundo tipo de procesos hemos observado una reducción del ancho de la línea en las regiones donde la capa blanda y dura invertía la direción de su imanación. Esto podría indicar una reducción de la rugosidad de la capa sobre la que se realiza la oxidación con el plasma.

Hemos estudiado la dependencia con la temperatura hasta 5 K de las propiedades estáticas y dinámicas de la imanación en películas de Permalloy y en Permalloy incorporado como capa magnética blanda en uniones tunel. Se ha observado una anomalía en las propiedades dinámicas en las péliculas de Permalloy cerca de 60 K. En el caso de las uniones túnel magnéticas, la anomalía en las propiedades dinámicas depende de la composición de la capa magnética blanda. Esta anomalías indican una reorientación de la imanación en la intercara de Permalloy. De las propiedades estáticas hemos observado diferencias cualitativas entre las películas de Permalloy y el Permalloy icorporado en la unión túnel. Para explicar este efecto, se ha considerado una posible influencia de la capa dura acoplada antiferromagnéticamente con la capa blanda debido a una rugosidad anticorrelacionada entre las capas magnéticas que están a ambos lados de la barrera aislante.

Chapter 8

List of Publications

Published

• V. V. Pryadun, J. F. Sierra, F. G. Aliev, A. P. Levanuyk, R. Villar, L. Van Look, and V. V. Moshchalkov.:" Low frequency noise and complex AC magnetoresistance in superconducting Pb/Ge with square antidote lattice", *Physica C*, vol. **404**, p. 30 (2004).

• V.V. Pryadun, J. F. Sierra, F. G. Aliev, D. Golubovic and V. V. Moshchalkov.: "Plain superconducting films as magnetic field tunable two-dimensional rectifiers" *Appl. Phys. Lett.*, vol. **88**, p. 062517 (2006).

• R. Villar, V. V. Pryadun , J. F. Sierra, F. G. Aliev, E. González, J. L. Vicent, D. Golubovic, and V. V. Moshchalkov.: "Magnetic field induced suppression of vortex flow resistance in superconductors with periodic pinning centers", *Physica C*, vol. **437-438**, p. 345 (2006)

• J. F. Sierra, A. A. Awad, G. N. Kakazei, F. J. Palomares and F. G. Aliev.: "Broadband magnetic response of periodic arrays of FeNi dots"

IEEE Trans. Magn. (accepted for publication).

Submmited

• F. G. Aliev , A. P. Levanyuk, R. Villar, J. F. Sierra, V. V. Pryadun, and A. A. Awad, E. M. González, J. L. Vicent and V. V. Moshchalkov.: "Unusual permanent electric fields induced by a high frequency alternating current in superconducting Nb films under a perpendicular magnetic field" (submmited to *Phys. Rev. B*).

• J. F. Sierra, V.V.Pryadun and F.G.Aliev, S. E. Russek, M. Garcia-Hernández, E.Snoeck and V. V. Metlushko.: "Temperature dependent dynamic and static magnetic response of Permalloy free layers in magnetic tunnel junctions with Al_2O_3 barriers" (submmited to *Appl. Phys. Lett.*).

Bibliography

[1] L. Landau and E. Lifshitz, "On the theory of magnetic permeability in ferromagnetic bodies," *Physik. Z. Sowejtunion*, vol. **8**, p. 153, 1935.

[2] T. A. Gilbert, "A lagrangian formulation of the gyromagnetic equation of the magnetic field," *Armor Research Foundation Project No. A059*, 1955, unpublished.

[3] W. K. Hiebert, A. Stankiewicz, and M. R. Freeman, "Direct observation of magnetic relaxation in a small Permalloy disk by time-resolved scanning Kerr microscopy," *Phys. Rev. Lett.*, vol. **79**, p. 1134, 1997.

[4] M. Farle, "Ferromagnetic resonance of ultrathin metallic layers," *Rep. Prog. Phys.*, vol. **61**, p. 755, 1998.

[5] J. Pelzl and U. Netzelman, *Topics in Current Physics, Vol 47.* Berlin: Springer-Verlag, 1989.

[6] H. Suhl, "Theory of the magnetic damping constant," *IEEE Trans. Magn.*, vol. **34**, p. 1834, 1998.

[7] J. Ho, F. C. Khanna, and B. C. Choi, "Radiation-spin interaction, Gilbert damping, and spin torque," *Phys. Rev. Lett.*, vol. **92**, p. 097601, 2004.

[8] V. L. Safonov and H. N. Bertram, "Impurity relaxation mechanism for dynamic magnetization reversal in a single domain grain," *Phys. Rev. B*, vol. **61**, p. R14893, 2000.

[9] V. Korenman and R. E. Prange, "Anomalous damping of spin waves in magnetic metals," *Phys. Rev. B*, vol. **6**, p. 2769, 1972.

[10] V. Kambersky and C. E. Patton, "Spin-wave relaxation and phenomenological damping in ferromagnetic resonance," *Phys. Rev. B*, vol. **11**, p. 2668, 1975.

[11] J. M. Lock, "Eddy current damping in thin metallic ferromagnetic films," *Br. J. Appl. Phys.*, vol. **17**, p. 1645, 1966.

[12] A. M. Clogston, H. Suhl, L. R. Walker, and P. W. Anderson, "Ferromagnetic resonance linewidth in insulating materials," *J. Phys. Chem. Solids*, vol. **1**, p. 129, 1956.

[13] R. Arias and D. L. Mills, "Extrinsic contributions to the ferromagnetic resonance response of ultrathin films," *Phys. Rev. B*, vol. **60**, p. 7395, 1999.

[14] S. Chikazumi and S. H. Charap, *Physics of Magnetism*. Florida: Krieger Co., 1978.

[15] J. H. E. Griffiths, "Anomalous high-frequency resistance of ferromagnetic metals," *Nature*, vol. **158**, p. 670, 1946.

[16] C. Kittel, "On the theory of ferromagnetic resonance absorption," *Phys. Rev.*, vol. **73**, p. 155, 1948.

[17] R. Urban, G. Woltersdorf, and B. Heinrich, "Gilbert damping in single and multilayer ultrathin films: Role of interfaces in nonlocal spin dynamics," *Phys. Rev. Lett.*, vol. **87**, p. 217204, 2001.

[18] J.-A. Berteaud and H. Pascard, "Relaxation and nonlinear effects in ferromagnetic thin films," *J. Appl. Phys.*, vol. **36**, p. 970, 1965.

[19] C. E. Patton and C. H. Wilts, "Temperature dependence of the ferromagnetic resonance linewidth in thin Ni-Fe films," *J. Appl. Phys.*, vol. **38**, p. 3537, 1967.

[20] A. B. Smith, *Bubble-Domain Memory Devices*. Norwood MA: Artech House, 1974.

[21] T. H. O'Dell, *Magnetic Bubbles*. New York: Wiley, 1974.

[22] M. N. Baibich, J. M. Broto, A. Fert, F. N. Van Dau, F. Petroff, P. Eitenne, G. Creuzet, A. Friederich, and J. Chazelas, "Giant magnetoresistance of (001)Fe/(001)Cr magnetic superlattices," *Phys. Rev. Lett.*, vol. **61**, p. 2472, 1988.

[23] G. Binasch, P. Grünberg, F. Saurenbach, and W. Zinn, "Enhanced magnetoresistance in layered magnetic structures with antiferromagnetic interlayer exchange," *Phys. Rev. B.*, vol. **39**, p. 4828, 1989.

[24] J. S. Moodera, L. R. Kinder, T. M. Wong, and R. Meservey, "Large magnetoresistance at room temperature in ferromagnetic thin film tunnel junctions," *Phys. Rev. Lett.*, vol. **74**, p. 3273, Apr 1995.

[25] T. Miyazaky and N. Tezuka, "Giant magnetic tunneling effect in $Fe/Al_2O_3/Fe$ junction," *J. Magn. Magn. Mater.*, vol. **139**, p. 231, 1995.

[26] M. Jullière, "Tunneling between ferromagnetic films," *Phys. Lett. A*, vol. **54**, p. 225, 1975.

[27] W. P. Meiklejohn and C. P. Bean, "New magnetic anisotropy," *Phys. Rev.*, vol. **102**, p. 1413, 1956.

[28] B. K. Kuanr, R. E. Camley, and Z. Celinski, "Exchange bias of NiO/NiFe: Linewidth broadening and anomalous spin-wave damping," *J. Appl. Phys.*, vol. **93**, p. 7723, 2003.

[29] R. D. McMichael, C. G. Lee, M. D. Stiles, F. G. Serpa, P. J. Chen, and W. F. Egelhoff Jr, "Exchange bias relaxation in CoO-biased films," *J. Appl. Phys.*, vol. **87**, p. 6406, 2000.

[30] S. M. Rezende, A. Azevedo, M. A. Lucena, and F. M. de Aguiar, "Anomalous spin-wave damping in exchange-biased films," *Phys. Rev. B.*, vol. **63**, p. 214418, 2001.

[31] J. Dubowik, F. Stobiecki, I. Goscianska, Y. P. Lee, A. Paetzold, and K. Roll, "Enhanced spin-wave damping in exchange-biased films," *J. Kor. Phys. Soc.*, vol. **45**, p. 42, 2004.

[32] M. J. Pechan, D. Bennett, N. Teng, C. Leighton, J. Nogues, and I. K. Schuller, "Induced anisotropy and positive exchange bias: A temperature, angular, and cooling field study by ferromagnetic resonance," *Phys. Rev. B*, vol. **65**, p. 064410, 2002.

[33] R. Urban, B. Heinrich, and G. Woltersdorf, "Semiclassical theory of spin transport in magnetic multilayers," *J. Appl. Phys.*, vol. **93**, p. 8280, 2003.

[34] P. Lubitz, M. Rubinstein, J. J. Krebs, and S.-F. Cheng, "Frequency and temperature dependence of ferromagnetic linewidth in exchange biased Permalloy," *J.Appl.Phys.*, vol. **89**, p. 6901, 2001.

[35] P. Grünberg, R. Schreiber, Y. Pang, M. B. Brodsky, and H. Sowers, "Layered magnetic structures: Evidence for antiferromagnetic coupling of Fe layers across Cr interlayers," *Phys. Rev. Lett.*, vol. **57**, p. 2442, 1986.

[36] S. S. P. Parkin, N. More, and K. P. Roche, "Oscillations in exchange coupling and magnetoresistance in metallic superlattice structures: Co/Ru, Co/Cr, and Fe/Cr," *Phys. Rev. Lett.*, vol. **64**, p. 2304, 1990.

[37] J. C. Slonczewski, "Fluctuation mechanism for biquadratic exchange coupling in magnetic multilayers," *Phys. Rev. Lett.*, vol. **67**, p. 3172, 1991.

[38] R. P. Cowburn, D. K. Koltsov, A. O. Adeyeye, M. E. Welland, and D. M. Tricker, "Single-domain circular nanomagnets," *Phys. Rev. Lett.*, vol. **83**, p. 1042, 1999.

[39] A. Wachowiak, J. Wiebe, M. Bode, O. Pietzsch, M. Morgensten, and R. Wiesendanger, "Direct observation of internal spin-structure of magnetic vortex cores," *Science*, vol. **298**, p. 577, 2002.

[40] T. Shinjo, T. Okuno, R. Hassdorf, K. Shigeto, and T. Ono, "Magnetic vortex core observation in circular dots of Permalloy," *Science*, vol. **289**, p. 930, 2000.

[41] G. N. Kakazei, P. E. Wigen, K. Y. Guslienko, R. W. Chantrell, N. A. Lesnik, V. Metlushko, H. Shima, K. Fukamichi, Y. Otani, and V. Novosad, "In-plane and out-of-plane uniaxial anisotropies in rectangular arrays of circular dots studied by ferromagnetic resonance," *J. Appl. Phys.*, vol. **93**, p. 8418, 2003.

[42] G. N. Kakazei, P. E. Wigen, K. Y. Guslienko, V. Novosad, A. V. Slavin, V. O. Golub, N. A. Lesnik, and Y. Otani, "Spin-wave spectra of perpendicularly magnetized circular submicron dot arrays," *Appl. Phys. Lett.*, vol. **85**, p. 443, 2004.

[43] A. A. Thiele, "Steady-state motion of magnetic domains," *Phys. Rev. Lett.*, vol. **30**, p. 230, 1973.

[44] K. Y. Guslienko, W. Scholz, R. W. Chantrell, and V. Novosad, "Vortex-state oscillations in soft magnetic cylindrical dots," *Phys. Rev. B*, vol. **71**, p. 144407, 2005.

[45] J. P. Park, P. Eames, D. M. Engebretson, J. Berezovsky, and P. A. Crowell, "Imaging of spin dynamics in closure domain and vortex structures," *Phys. Rev. B*, vol. **67**, p. 020403, 2003.

[46] V. Novosad, M. Grimsditch, K. Y. Guslienko, P. Vavassori, Y. Otani, and S. D. Bader, "Spin excitations of magnetic vortices in ferromagnetic nanodots," *Phys. Rev. B*, vol. **66**, no. 5, p. 052407, 2002.

[47] K. Y. Guslienko, B. A. Ivanov, V. Novosad, Y. Otani, H. Shima, and K. Fukamichi, "Eigenfrequencies of vortex state excitations in magnetic submicron-size disks," *J. Appl. Phys.*, vol. **91**, p. 8037, 2002.

[48] V. Novosad, F. Y. Fradin, P. E. Roy, K. S. Buchanan, K. Y. Guslienko, and S. D. Bader, "Magnetic vortex resonance in patterned ferromagnetic dots," *Phys. Rev. B*, vol. **72**, p. 024455, 2005.

[49] M. Buess, R. Höllinger, T. Haug, K. Perzlmaier, U. Krey, D. Pescia, M. R. Scheinfein, D. Weiss, and C. H. Back, "Fourier transform imaging of spin vortex eigenmodes," *Phys. Rev. Lett.*, vol. **93**, p. 077207, 2004.

[50] B. A. Ivanov and C. E. Zaspel, "Magnon modes for thin circular vortex-state magnetic dots," *Appl. Phys. Lett.*, vol. **81**, p. 1261, 2002.

[51] K. Y. Guslienko, A. N. Slavin, V. Tiberkevich, and S. H. Kim, "Dynamic origin of azimuthal modes splitting in vortex-state magnetic dots," *Cond. Mat. ArXiv:0808.3335*, 2008.

[52] X. Zhu, Z. Liu, V. V. Metlushko, P. Grütter, and M. R. Freeman, "Broad-band spin dynamics of the magnetic vortex state: Effect of the pulsed field direction," *Phys. Rev. B*, vol. **71**, p. R180408, 2005.

[53] J. P. Park and P. A. Crowell, "Interactions of spinwaves with a magnetic vortex," *Phys. Rev. Lett.*, vol. **95**, p. 167201, 2005.

[54] L. Giovannini, F. Montoncello, F. Nizzoli, G. Gubbiotti, G. Carlotti, T. Okuno, T. Shinjo, and M. Grimsditch, "Spin excitations of nanometric cylindrical dots in vortex and saturated magnetic states," *Phys. Rev. B*, vol. **70**, p. 172404, 2004.

[55] T. S. Rahman and D. L. Mills, "Spin-wave renormalization in exchange- and dipolar-coupled ferromagnets: Bulk spin waves and the Damon-Eshbach surface spin wave," *Phys. Rev. B*, vol. **20**, p. 1173, 1979.

[56] K. Y. Guslienko and A. N. Slavin, "Spin-wave excitations in cylindrical magnetic dot arrays with in-plane magnetization," *J. Magn. Magn. Mater.*, vol. **215-216**, p. 576, 2000.

[57] J. Jorzick, S. O. Demokritov, B. Hillebrands, B. Bartenlian, C. Chappert, D. Decanini, F. Rousseaux, and E. Cmabril, "Spin-wave quantization and dynamic coupling in micron-size circular magnetic dots," *Appl. Phys. Lett.*, vol. **75**, p. 3859, Dec 1999.

[58] G. Gubbiotti, G. Carlotti, R. Ziveri, F. Nizzoli, T. Okuno, and T. Shinjo, "Spin wave modes in submicron cylindrical dots," *J. Appl. Phys.*, vol. **93**, p. 7607, 2003.

[59] I. Neudecker, K. Perzlmaier, F. Hoffmann, G. Woltersdorf, M. Buess, D. Weiss, and C. H. Back, "Modal spectrum of Permalloy disks excited by in-plane magnetic fields," *Phys. Rev. B*, vol. **73**, p. 134426, 2006.

[60] H. Kamerlingh-Onnes, "The resistance of pure mercury at helium temperatures," *Leiden comm.*, vol. **112b**, p. 124, 1911.

[61] W. Meissner and R. Ochsenfeld, "Ein neuer effekt bei eintritt der supraleitfähigkeit," *Naturwiss*, vol. **21**, p. 787, 1933.

[62] F. London and H. London, "The electromagnetic equations of the supraconductor," *Proc. Roy. Soc.*, vol. **A149**, p. 71, 1935.

[63] V. L. Ginzburg and L. D. Landau, "On the theory of superconductivity," *Zh. Eksp. Teor. Fiz.*, vol. **20**, p. 1064, 1950.

[64] A. A. Abrikosov, "On the magnetic properties of superconductors of the second group," *Zh. Eksp. Teor. Fiz.*, vol. **32**, p. 1442, 1957.

[65] J. Bardeen, L. Cooper, and J. Schrieffer, *Theory of superconductivity.* 1960: N.N. Bogolyubov, 1960.

[66] L. P. Gorkov, "Microscopic derivation of the Ginzburg-Landau equations in the theory of superconductivity," *Zh. Eksp. Teor. Fiz.*, vol. **36**, p. 1918, 1959.

[67] J. G. Bednorz and K. A. Müller, "Possible high Tc superconductivity in the Ba-La-Cu-O system," *Z. Phys. B*, vol. **64**, p. 189, 1986.

[68] M. Tinkham, *Introduction to superconductivity.* New York: Mc Graw-Hill, 1975.

[69] M. Baert, V. V. Metlushko, R. Jonckheere, V. V. Moshchalkov, and Y. Bruynseraede, "Composite flux-line lattices stabilized in superconducting films by a regular array of artificial defects," *Phys. Rev. Lett*, vol. **74**, p. 3269, 1995.

[70] M. Baert, V. V. Metlushko, C. D. Potter, E. Rosseel, R. Jonckheere, V. V. Moshchalkov, and Y. Bruynseraede, "Critical currents and flux phases in superconducting multilayers with a lattice of submicrometer holes," *Phys. C*, vol. **235**, p. 2789, 1994.

[71] M. Baert, V. V. Metlushko, R. Jonckheere, V. V. Moshchalkov, and Y. Bruynseraede, "Flux phases and quantized pinning force in superconductor with a periodic lattice of pinning centres," *Europhys. Lett.*, vol. **29**, p. 157, 1995.

[72] V. V. Moshchalkov, M. Baert, V. V. Metlushko, E. Rosseel, J. Van Bael, K. Temst, R. Jonckheere, and Y. Bruynseraede, "Magnetization of multiple-quanta vortex lattices," *Phys. Rev. B*, vol. **54**, p. 7385, 1996.

[73] ——, "Pinning by an antidot lattice: The problem of the optimum antidot size," *Phys. Rev. B*, vol. **57**, p. 3615, 1998.

[74] J. E. Villegas, S. Saveliev, F. Nori, E. M. Gonzalez, J. V. Anguita, R. Garcia, and J. L. Vicent, "A superconducting reversible rectifier that controls the motion of magnetic flux quanta," *Science*, vol. **302**, p. 1188, 2003.

[75] R. P. Feynman and R. B. Leighton, *The Feynman Lectures on Physics.* Reading, MA: Adison-Wesley, 1969.

[76] C. S. Lee, B. Jankó, I. Derényi, and A. L. Barabási, "Reducing vortex density in superconductors using the "ratchet effect"," *Nature*, vol. **400**, p. 337, 1999.

[77] B. Y. Zhu, F. Marchesoni, V. V. Moshchalkov, and F. Nori, "Controllable step motors and rectifiers of magnetic flux quanta using periodic arrays of asymmetric pinning defects," *Phys. Rev. B*, vol. **68**, p. 014514, 2003.

[78] B. Y. Zhu, F. Marchesoni, and F. Nori, "Controlling the motion of magnetic flux quanta," *Phys. Rev. Lett.*, vol. **92**, p. 180602, 2004.

[79] J. F. Wambaugh, C. Reichhardt, C. J. Olson, F. Marchesoni, and F. Nori, "Superconducting fluxon pumps and lenses," *Phys. Rev. Lett.*, vol. **83**, p. 5106, 1999.

[80] C. J. Olson, C. Reichhardt, B. Jankó, and F. Nori, "Collective interaction-driven ratchet for transporting flux quanta," *Phys. Rev. Lett.*, vol. **87**, p. 177002, 2001.

[81] A. V. Silhanek, L. Van Look, S. Raedts, R. Jonckheere, and V. V. Moshchalkov, "Guided vortex motion in superconductors with a square antidot array," *Phys. Rev. B*, vol. **68**, p. 214504, 2003.

[82] J. E. Villegas, E. M. Gonzalez, M. I. Montero, I. K. Schuller, and J. L. Vicent, "Directional vortex motion guided by artificially induced mesoscopic potentials," *Phys. Rev. B*, vol. **68**, p. 224504, 2003.

[83] R. Wördenweber, P. Dymashevski, and V. R. Misko, "Guidance of vortices and the vortex ratchet effect in high-Tc superconducting thin films obtained by arrangement of antidots," *Phys. Rev. B*, vol. **69**, p. 184504, 2004.

[84] C. C. de Souza Silva and G. Carneiro, "Simple model for dynamical melting of moving vortex lattices interacting with periodic pinning," *Phys. Rev. B*, vol. **66**, p. 054514, 2002.

[85] G. Carneiro, "Tunable interactions between vortices and a magnetic dipole," *Phys. Rev. B*, vol. **72**, p. 144514, 2005.

[86] M. Morelle, N. Schildermans, and V. V. Moshchalkov, "Rectification effects in superconducting triangles," *Appl. Phys. Lett.*, vol. **89**, p. 112512, 2006.

[87] Y. Togawa, K. Harada, T. Akashi, H. Kasai, T. Matsuda, F. Noria, A. Maeda, and A. Tonomura, "Direct observation of rectified motion of vortices in niobium superconductor," *Phys. Rev. Lett.*, vol. **95**, p. 087002, 2005.

[88] R. L. Conger and F. C. Essig, "Resonance and reversal phenomena in ferromagnetic films," *Phys. Rev.*, vol. **104**, no. 4, p. 915, 1956.

[89] C. D. Olson and A. V. Phom, "Flux reversal in thin films of 82%Ni 18%Fe," *J. Appl. Phys.*, vol. **29**, p. 274, 1958.

[90] F. B. Humphrey, "Transverse flux change in soft ferromagnetics," *J. Appl. Phys.*, vol. **29**, p. 284, 1958.

[91] W. Dietrich, W. E. Proebster, and P. Wolf, "Nanosecond switching in thin magnetic films," *IBM J. Res. Dev.*, vol. **4**, p. 189, 1960.

[92] W. Dietrich and W. E. Proebster, "Millimicrosecond magnetization reversal in thin magnetic films," *J. Appl. Phys.*, vol. **31**, p. S281, 1960.

[93] T. J. Silva, C. S. Lee, T. M. Crawford, and C. T. Rogers, "Inductive measurement of ultrafast magnetization dynamics in thin-film Permalloy," *J. Appl. Phys.*, vol. **85**, p. 7849, 1999.

[94] A. B. Kos, T. J. Silva, and P. Kabos, "Pulsed inductive microwave magnetometer," *Rev. Sci. Instrum.*, vol. **73**, p. 3563, 2002.

[95] S. Kaka and S. E. Russek, "Precessional switching of submicrometer spin valves," *Appl. Phys. Lett.*, vol. **80**, p. 2958, 2002.

[96] H. W. Schumacher, C. Chappert, P. Crozat, R. C. Sousa, P. P. Freitas, and M. Bauer, "Coherent suppression of magnetic ringing in microscopic spin valve elements," *Appl. Phys. Lett.*, vol. **80**, p. 3781, 2002.

[97] R. H. Koch, J. G. Deak, D. W. Abraham, P. L. Trouilloud, R. A. Altman, Y. Lu, W. J. Gallagher, R. E. Scheuerlein, K. P. Roche, and S. S. P. Parkin, "Magnetization reversal in micron-sized magnetic thin films," *Phys. Rev. Lett.*, vol. **81**, p. 4512, 1998.

[98] H. W. Schumacher, S. Serrano-Guisan, K. Rott, and G. Reiss, "Ultrafast magnetization dynamics probed by anisotropic magnetoresistance," *Appl. Phys. Lett.*, vol. **90**, p. 042504, 2007.

[99] M. R. Freeman and J. F. Smyth, "Picosecond time-resolved magnetization dynamics of thin-film heads," *J. Appl. Phys.*, vol. **79**, p. 5898, 1996.

[100] T. Gerrits, J. Hohlfeld, O. Gielkens, and K. J. Veenstra, "Magnetization dynamics in NiFe thin films induced by short in-plane magnetic field pulses," *J. Appl. Phys.*, vol. **89**, p. 7648, 2001.

[101] T. M. Crawford, T. J. Silva, C. W. Teplin, and C. T. Rogers, "Subnanosecond magnetization dynamics measured by the second-harmonic magneto-optic Kerr effect," *Appl. Phys. Lett.*, vol. **74**, p. 3386, 1999.

[102] T. M. Crawford and Y. K. Rogers, C. T.and Kim, "Observation of the transverse second-harmonic magneto-optic Kerr effect from $Ni_{81}Fe_{19}$ thin film structures," *Appl. Phys. Lett.*, vol. **68**, p. 1573, 1996.

[103] J. Reif, J. C. Zink, C.-M. Schneider, and J. Kirschner, "Effects of surface magnetism on optical second harmonic generation," *Phys. Rev. Lett.*, vol. **67**, p. 2878, 1991.

[104] A. Ercole, A. O. Adeyeye, J. A. C. Bland, and D. G. Hasko, "Size-dependent spin-wave frequency in ferromagnetic wire-array structures," *Phys. Rev. B*, vol. **58**, p. 345, 1998.

[105] C. Mathieu, J. Jorzick, A. Frank, S. O. Demokritov, A. N. Slavin, B. Hillebrands, B. Bartenlian, C. Chappert, D. Decanini, F. Rousseaux, and E. Cambril, "Lateral quantization of spin waves in micron size magnetic wires," *Phys. Rev. Lett.*, vol. **81**, p. 3968, 1998.

[106] V. Novosad, M. Grimsditch, K. Y. Guslienko, P. Vavassori, Y. Otani, and S. D. Bader, "Spin excitations of magnetic vortices in ferromagnetic nanodots," *Phys. Rev. B*, vol. **66**, p. 052407, 2002.

[107] G. Gubbiotti, G. Carlotti, T. Okuno, T. Shinjo, F. Nizzoli, and R. Zivieri, "Brillouin light scattering investigation of dynamic spin modes confined in cylindrical Permalloy dots," *Phys. Rev. B*, vol. **68**, p. 184409, 2003.

[108] S. O. Demokritov and B. Hillebrands, *Spinwaves in Laterally Confined Magnetic Structures: Spin Dynamics in Confined Magnetic Structures I).* Berlin, Heildelberf: Springer-Verlag, 2002.

[109] G. Counil, J. V. Kim, T. Devolder, C. Chappert, K. Shigeto, and Y. Otani, "Spin wave contributions to the high-frequency magnetic response of thin films obtained with inductive methods," *J. Appl. Phys.*, vol. **95**, p. 5646, 2004.

[110] O. Mosendz, B. Kardasz, D. Schmool, and B. Heinrich, "Spin dynamics at low microwave frequencies in crystalline fe ultrathin film double layers using co-planar transmission lines," *J. Magn. Magn. Mater.*, vol. **300**, p. 174, 2006.

[111] B. K. Kuanr, R. Camley, and Z. Celinsky, "Extrinsic contribution to Gilbert damping in sputtered NiFe films by ferromagnetic resonance," *J. Magn. Magn. Mater.*, vol. **286**, p. 276, 2005.

[112] S. S. Kalarickal, P. Krivosik, M. Wu, C. E. Patton, M. L. Schneider, P. Kabos, T. J. Silva, and J. P. Nibarger, "Ferromagnetic resonance linewidth in metallic thin films: Comparison of measurement methods," *J. Appl. Phys.*, vol. **99**, p. 093909, 2006.

[113] W. Barry, "A broad-band, automated, stripline technique for the simultaneous measurement of complex permittivity and permeability," *IEEE Trans. Microwave Theory Tech.*, vol. **34**, p. 80, 1986.

[114] C. Bilzer, T. Devolder, P. Crozat, C. Chappert, S. Cardoso, and P. P. Freitas, "Vector network analyzer ferromagnetic resonance of thin films on coplanar waveguides: Comparison of different evaluation methods," *J. Appl. Phys.*, vol. **101**, p. 074505, 2007.

[115] V. V. Pryadun, J. F. Sierra, F. G. Aliev, A. P. Levanyuk, R. Villar, L. Van Look, and V. V. Moshchalkov, "Low frequency noise and complex AC magnetoresistance in superconducting Pb/Ge with square antidot lattice," *Physica C*, vol. **404**, p. 30, 2004.

[116] P. S. Swartz and H. R. Hart Jr, "Surface effects in the mixed superconducting state," *Phys. Rev.*, vol. **137**, p. A818, 1965.

[117] D. D. Morrison and R. M. Rose, "Controlled pinning in superconducting foils by surface microgrooves," *Phys. Rev. Lett.*, vol. **25**, p. 356, 1970.

[118] R. P. Huebener, *Magnetic Flux Structures in Superconductors.* Berlin: Springer-Verlag., 1979.

[119] V. V. Adrianov, V. B. Zenkevic, V. V. Kurgozov, V. V. Sychev, and F. F. Ternokski, "Effective resistance of an imperfect Type-II superconductor in an oscillating magnetic field," *Sov. Phys. JETP*, vol. **31**, p. 815, 1969.

[120] R. P. Huebener and V. A. Rove, "Influence of oscillatory magnetic fields on the Nernst effect in superconducting lead films," *Solid State Commun.*, vol. **7**, p. 1763, 1969.

[121] A. N. Ulyanov, "Transport of alternating current and direct current by hard superconductors. Critical and resistive state," *J. Appl. Phys.*, vol. **85**, p. 3726, 1999.

[122] S. Saveliev and F. Nori, "Experimentally realizable devices for controlling the motion of magnetic flux quanta in anisotropic superconductors," *Nat. Mater.*, vol. **1**, p. 179, 2002.

[123] R. Wördenweber and P. Dymashevski, "Guided vortex motion in high-Tc superconducting thin films and devices with special arrangements of artificial defects," *Physica C*, vol. **404**, p. 421, 2004.

[124] H. Sadate-Akhavi, J. T. Chen, A. M. Kadin, J. E. Keem, and S. R. Ovshinsky, "Observation of rf-induced dc voltages in sputtered binary superconducting films," *Solid State Commun.*, vol. **50**, p. 975, 1984.

[125] R. Rinaldi, A. Biasco, G. Maruccio, V. Arima, P. Visconti, R. Cingolani, P. Facci, F. De rienzo, R. Di Felipe, E. Molinari, M. P. Verbeet, and G. W. Canters, "Electronic rectification in protein devices," *Appl. Phys. Lett.*, vol. **82**, p. 472, 2003.

[126] G. Cuniberti, J. Yi, and M. Porto, "Pure-carbon ring transistor: Role of topology and structure," *Appl. Phys. Lett.*, vol. **81**, p. 850, 2002.

[127] B. Hackens, L. Gence, C. Gustin, X. Wallart, S. Bollaert, A. Cappy, and V. Bayot, "Sign reversal and tunable rectification in a ballistic nanojunction," *Appl. Phys. Lett.*, vol. **85**, p. 4508, 2004.

[128] H. Linke, T. E. Humphrey, A. Löfgren, A. O. Sushkov, R. Newbury, R. P. Taylor, and P. Omling, "Experimental tunneling ratchets," *Science*, vol. **286**, p. 2314, 1999.

[129] K. H. Lee, "Ratchet effect in an ac-current driven josephson junction array," *Appl. Phys. Lett.*, vol. **83**, p. 117, 2003.

[130] I. Zapata, R. Bartussek, F. Sols, and P. Hänggi, "Voltage rectification by a SQUID ratchet," *Phys. Rev. Lett.*, vol. **77**, p. 2292, 1996.

[131] A. I. Gubin, K. S. Ilt̃in, S. A. Vitusevich, M. Siegel, and N. Klein, "Dependence of magnetic penetration depth on the thickness of superconducting Nb thin films," *Phys. Rev. B*, vol. **72**, p. 064503, 2005.

[132] J. I. Martin, M. Vélez, A. Hoffmann, I. K. Schuller, and J. L. Vicent, "Artificially induced reconfiguration of the vortex lattice by arrays of magnetic dots," *Phys. Rev. Lett.*, vol. **83**, p. 1022, 1999.

[133] R. Villar, V. V. Pryadun, J. F. Sierra, F. G. Aliev, E. González, J. L. Vicent, D. Gulovic, and V. V. Moshchslkov, "Magnetic field induced suppression of vortex flow resistance in superconductors with periodic pinning centers," *Physica C*, vol. **437-438**, p. 345, 2006.

[134] A. V. Silhanek, S. Raedts, M. J. Van Bael, and V. V. Moshchalkov, "Experimental determination of the number of flux lines trapped by microholes in superconducting samples," *Phys. Rev. B*, vol. **70**, p. 054515, 2004.

[135] A. V. Silhanek, L. Van Look, S. Raedts, R. Jonckheere, and V. V. Moshchalkov, "Guided vortex motion in superconductors with a square antidot array," *Phys. Rev. B*, vol. **68**, p. 214504, 2003.

[136] A. Buzdin and M. Daumens, "Electrostatic analogies in the problems of vortex-defect interactions," *Physica C*, vol. **332**, p. 108, 2000.

[137] T. Schuster, M. V. Indenbom, H. Kuhn, E. H. Brandt, and M. Konczykowski, "Flux penetration and overcritical currents in flat superconductors with irradiation-enhanced edge pinning: Theory and experiment," *Phys. Rev. Lett.*, vol. **73**, p. 1424, 1994.

[138] E. H. Brandt, "Superconductors in realistic geometries: Geometric edge barrier versus pinning," *Physica C*, vol. **332**, p. 99, 2000.

[139] C. P. Bean and J. D. Livingston, "Surface barrier in Type-II superconductors," *Phys. Rev. Lett*, vol. **12**, p. 14, 1964.

[140] Y. Paltiel, E. Zeldov, Y. N. Myasoedov, H. Shtrickman, S. Bhattacharya, M. J. Higgins, Z. L. Xiao, E. Y. Andrei, P. L. Gammel, and D. J. Bishop, "Dynamic instabilities and memory effects in vortex matter," *Nature*, vol. **403**, p. 398, 2000.

[141] D. Y. Vodolazov, "Effect of surface defects on the first field for vortex entry in type-II superconductors," *Phys. Rev. B*, vol. **62**, p. 8691, 2000.

[142] M. H. Indenbom, H. Kronmüller, T. W. Li, P. H. Kes, and A. A. Menovsky, "Equilibrium magnetic properties and meissner expulsion of magnetic flux in $Bi_2Sr_2CaCu_2O_x$ single crystals," *Physica C*, vol. **222**, p. 203, 1994.

[143] P. G. de Gennes, *Superconductivity of Metals and Alloys.* New York: Benjamin., 1966.

[144] E. Zeldov, A. I. Larkin, V. B. Geshkenbein, M. Konczykowski, D. Majer, B. Khaykovich, V. M. Vinokur, and H. Shtrikman, "Geometrical barriers in high-temperature superconductors," *Phys. Rev. Lett.*, vol. **73**, p. 1428, 1994.

[145] M. Benkraouda and J. R. Clem, "Critical current from surface barriers in type-II superconducting strips," *Phys. Rev. B*, vol. **58**, p. 15103, 1998.

[146] A. A. Elistratov, D. Y. Vodolazov, I. L. Maksimov, and J. R. Clem, "Field-dependent critical current in type-II superconducting strips: Combined effect of bulk pinning and geometrical edge barrier," *Phys. Rev. B*, vol. **66**, p. 220506, 2002.

[147] A. V. Bobyl, D. V. Shantsev, Y. M. Galperin, T. H. Johansen, M. Baziljevich, and S. F. Karmanenko, "Relaxation of transport current distribution in a YBaCuO strip studied by magneto-optical imaging," *Superconducting Sci. Technol.*, vol. **15**, p. 82, 2002.

[148] A. Gurevich, H. Küpfer, B. Runtsch, R. Meier-Hirmer, D. Lee, and K. Salama, "Transient regimes of flux creep in high-Tc superconductors," *Phys. Rev. B*, vol. **44**, no. 21, p. 12090, 1991.

[149] A. L. Fetter and P. C. Hohenberg, "The mixed state of thin superconducting films in perpendicular fields," *Phys. Rev.*, vol. **159**, p. 330, 1967.

[150] A. Gerber and G. Deutscher, "ac-to-dc conversion and Aharonov-Bohm effect in percolating superconducting films," *Phys. Rev. Lett.*, vol. **64**, no. 13, p. 1585, 1990.

[151] F. G. Aliev, "Generation of DC electric fields due to vortex rectification in superconducting films," *Physica C*, vol. **437-438**, p. 1, 2006.

[152] V. V. Pryadun, J. F. Sierra, F. G. Aliev, D. S. Gulobic, and V. V. Moshchalkov, "Plain superconducting films as magnetic field tunable two-dimensional rectifiers," *Appl. Phys. Lett.*, vol. **88**, p. 062517, 2006.

[153] V. Novosad, M. Grimsditch, J. Darrouzet, J. Pearson, S. D. Bader, V. Metlushko, K. Guslienko, Y. Otani, H. Shima, and K. Fukamichi, "Shape effect on magnetization reversal in chains of interacting ferromagnetic elements," *Appl. Phys. Lett.*, vol. **82**, p. 3716, 2003.

[154] X. F. Han, M. Grimsditch, J. Meersschaut, A. Hoffmann, Y. Ji, J. Sort, J. Nogués, R. Divan, J. E. Pearson, and D. J. Keavney, "Magnetic instability regions in patterned structures: Influence of element shape on magnetization reversal dynamics," *Phys. Rev. Lett.*, vol. **98**, p. 147202, 2007.

[155] G. Gubbiotti, G. Carlotti, T. Okuno, M. Grimsditch, L. Giovannini, F. Montoncello, and F. Nizzoli, "Spin dynamics in thin nanometric elliptical Permalloy dots: A Brillouin light scattering investigation as a function of dot eccentricity," *Phys. Rev. B*, vol. **72**, 2005.

[156] G. Gubbiotti, O. Kazakova, G. Carlotti, M. Hanson, and P. Vavarssori, "Spin-wave spectra in nanometric elliptical dots arrays," *IEE Trans. Magn.*, vol. **39**, no. 5, p. 2750, 2003.

[157] M. Jaafar, R. Yanes, A. Asenjo, O. Chubykalo-Fesenko, M. Vázquez, E. M. González, and J. L. Vicent, "Field induced vortex dynamics in magnetic Ni nanotriangles," *Nantechnology*, vol. **19**, p. 285717, 2008.

[158] K. Y. Guslienko and A. N. Slavin, "Spin waves in cylindrical magnetic dots with in-plane magnetization," *J. Appl. Phys.*, vol. **87**, p. 6337, 2000.

[159] G. Kakazei, P. Wigen, Y. Guslienko, A. N. Novosad, V. an Slavin, V. O. Golub, N. A. Lesnik, and Y. Otani, "Spin wave spectra of perpendicularly magnetized circular submicron dot arrays," *Appl. Phys. Lett.*, vol. **85**, p. 443, 2004.

[160] G. Kakazei, P. Wigen, Y. Guslienko, R. Chantrell, N. Lesnik, V. Metlushko, H. Shima, K. Fukamichi, Y. Otani, and V. Novosad, "In-plane and out-of-plane uniaxial anisotropies in rectangular arrays of circular dots studied by ferromagnetic resonance," *J. Appl. Phys.*, vol. **93**, p. 8418, 2003.

[161] M. Kostylev, P. Schrader, R. Stamps, G. Gubbiotti, G. Carlotti, A. Adeyeye, S. Goolaup, and N. Singh, "Partial frequency band gap in one-dimensional magnonic crystals," *Appl. Phys. Lett.*, vol. **92**, p. 132504, 2008.

[162] C. Mathieu, C. Hartmman, M. Bauer, O. Büttner, S. Riedling, B. Ross, S. O. Demokritov, B. Hillebrands, B. Bartenlian, C. Chappert, D. Decanini, F. Rosseaux, and E. Cambril, "Anisotropic magnetic coupling of Permalloy micron dots forming a square lattice," *Appl. Phys. Lett.*, vol. **70**, p. 2912, 1997.

[163] S. Jung, B. Watkins, L. DeLong, J. B. Ketterson, and V. Chandrasekhar, "Ferromagnetic resonance in periodic particle arrays," *Phys. Rev. B*, vol. **66**, p. 13240, 2002.

[164] I. Neudecker, K. Perzlmaier, F. Hoffmann, G. Woltersdorf, B. M., D. Weiss, and C. H. Back, "Modal spectrum of Permalloy disks excited by in-plane magnetic fields," *Phys. Rev. B*, vol. **73**, p. 134426, 2006.

[165] G. Neudecker, I. nd Woltersdorf, B. Heinrich, G. Okuno, T. Gubbiotti, and C. H. Back, "Comparison of frequency, field, and time domain ferromagnetic resonance methods," *J. Magn. Magn. Mater.*, vol. **307**, p. 148, 2006.

[166] J. F. Sierra, A. A. Awad, G. N. Kakazei, F. J. Palomares, and F. G. Aliev, "Broadband magnetic response of periodic arrays of FeNi dots," *accepted for publication in IEEE Trans. Magn.*

[167] P. Kraus and S. Chou, "Fabrication of planar quantum magnetic disk structure using electron beam lithography, reactive ion etching, and chemical mechanical polishing," *J. Vac. Sci. Technol. B*, vol. **13**, p. 2850, 1995.

[168] F. Rousseaux, D. Decanini, C. F., E. Cambril, C. Ravet, M. Chappert, N. Bardou, B. Bartenlian, and P. Veillet, "Study of large area high density magnetic dot arrays fabricated using synchrotron radiation based X-ray lithography," *J. Vac. Sci. Technol. B*, vol. **13**, p. 2787, 1995.

[169] A. Fernández, P. Bedrossian, S. Baker, S. Vermon, and D. Kania, "Magnetic force microscopy of single-domain cobalt dots patterned using interference lithography," *IEEE Trans. Magn.*, vol. 32, p. 4472, 1996.

[170] G. N. Kakazei, Y. G. Pogorelov, M. D. Costa, T. Mwes, P. E. Wigen, P. Hammel, V. O. Golub, O. T., and N. V., "Origin of fourfold anisotropy in square lattices of circular ferromagnetic dots," *Phys. Rev. B*, vol. **74**, p. R060406, 2006.

[171] G. Gubbiotti, M. Madami, S. Tacchi, G. Socino, G. Carlotti, and T. Okuno, "Effect of interdot dipolar coupling on the magnetic properties of Permalloy nano-cylinders," *Surface Science*, vol. **600**, p. 4143, 2006.

[172] J. P. Park and P. Crowell, "Interactions of spinwaves with a magnetic vortex," *Phys. Rev. Lett.*, vol. **95**, p. 167201, 2005.

[173] B. A. Ivanov and C. E. Zaspel, "High frequency modes in vortex-state nanomagnets," *Phys. Rev. Lett.*, vol. **94**, p. 027205, 2005.

[174] K. Y. Guslienko, *Private communication.*

[175] J. Hayakawa, S. Ikeda, Y. M. Lee, F. Matsukura, and H. Ohno, "Effect of high annealing temperature on giant tunnel magnetoresistance ratio of CoFeB/MgO/CoFeB magnetic tunnel junctions," *Appl. Phys. Lett.*, vol. **89**, p. 232510, 2006.

[176] D. Wang, C. Nordman, J. Daughton, Z. Qian, and J. Fink, "70% TMR at room temperature for SDT sandwich junctions with CoFeB as free and reference layers," *IEEE Trans. Magn.*, vol. **40**, p. 2269, 2004.

[177] S. Mao, J. Nowak, D. Song, P. Kolbo, L. Wang, E. Linville, D. Saunders, E. Murdock, and P. Ryan, "Spin tunneling heads above 20 Gb/in/sup 2/," *IEEE Trans. Magn.*, vol. **38**, p. 78, 2002.

[178] P. P. Freitas, R. Ferreira, S. Cardoso, and F. Cardoso, "Magnetoresistive sensors," *J. Phys.: Cond. Matter.*, vol. **19**, p. 165221, 2007.

[179] R. Dave, G. Steiner, J. Slaughter, J. Sun, B. Craigo, S. Pietambaram, K. Smith, G. Grynkewich, M. DeHerrera, J. Akerman, and S. Tehrani, "MgO-based tunnel junction material for high-speed toggle magnetic random access memory," *IEEE Trans. Magn.*, vol. **42**, p. 1935, 2006.

[180] A. A. Tulapurkar, Y. Suzuki, A. Fukushima, H. Kubota, H. Maehara, K. Tsunekawa, D. D. Djayaprawira, N. Watanabe, and S. Yuasa, "Spin-torque diode effect in magnetic tunnel junctions," *Nature*, vol. **438**, p. 339, 2005.

[181] S. Ikeda, J. Hayakawa, Y. M. Lee, F. Matsukura, Y. Ohno, T. Hanyu, and H. Ohno, "Magnetic tunnel junctions for spintronic memories and beyond," *IEEE Trans. Elec. Dev.*, vol. **54**, p. 991, 2007.

[182] E. Y. Tsymbal, O. N. Mryasov, and P. R. LeClair, "Spin-dependent tunnelling in magnetic tunnel junctions," *J. Phys.: Cond. Matt.*, vol. **15**, p. R109, Jan 2003.

[183] C. E. Patton, C. H. Wilts, and F. B. Humphrey, "Relaxation processes for ferromagnetic resonance in thin films," *J. Appl. Phys.*, vol. **38**, p. 1358, 1967.

[184] B. Heinrich, Y. Tserkovnyak, G. Woltersdorf, A. Brataas, R. Urban, and G. E. W. Bauer, "Dynamic exchange coupling in magnetic bilayers," *Phys. Rev. Lett.*, vol. **90**, p. 187601, 2003.

[185] R. D. McMichael, M. D. Stiles, P. J. Chen, and W. F. Egelhoff Jr, "Ferromagnetic resonance linewidth in thin films coupled to NiO," *J. Appl. Phys.*, vol. **83**, p. 7037, 1998.

[186] L. Lagae, R. Wirix-Speetjens, W. Eyckmans, S. Borghs, and J. De Boeck, "Increased gilbert damping in spin valves and magnetic tunnel junctions," *J. Magn. Magn. Mater.*, vol. **286**, p. 291, 2005.

[187] J. Z. Sun, "Spin-current interaction with a monodomain magnetic body: A model study," *Phys. Rev. B*, vol. **62**, p. 570, 2000.

[188] J.-V. Kim, "Stochastic theory of spin-transfer oscillator linewidths," *Phys. Rev. B*, vol. **73**, p. 174412, 2006.

[189] J. M. Shaw, R. Geiss, and S. E. Russek, "Dynamic lorentz microscopy of micromagnetic structure in magnetic tunnel junctions," *Appl. Phys. Lett.*, vol. **89**, p. 212503, 2006.

[190] R. D. McMichael, D. J. Twisselman, J. E. Bonevitch, P. J. Chen, W. F. Egelhoff, and S. E. Russek, "Ferromagnetic resonance mode interactions in periodically perturbed films," *J. Appl. Phys.*, vol. **91**, p. 8647, 2002.

[191] C. E. Patton and C. H. Wilts, "Temperature dependence of the ferromagnetic resonance linewidth in thin Ni-Fe films," *J. Appl. Phys.*, vol. **38**, p. 3537, 1967.

[192] M. Díaz de Sihues, P. J. Silva, and J. R. Fermin, "Effect of temperature on the ferromagnetic resonance of $Ni_{50}Fe_{50}$ thin films," *Physica B*, vol. **361**, p. 354, 2004.

[193] W. Xu, D. B. Watkins, L. E. DeLong, K. Rivkin, J. B. Ketterson, and V. V. Metlushko, "Ferromagnetic resonance study of nanoscale ferromagnetic ring lattices," *J. Appl. Phys.*, vol. 95, p. 6645, 2004.

[194] S. Cardoso, R. Ferreira, P. P. Freitas, M. MacKenzie, J. Chapman, J. O. Ventura, J. B. Sousa, and U. Kreisg, "Ferromagnetic coupling field reduction in CoFeB tunnel junctions deposited by ion beam," *IEEE Trans. Magn.*, vol. **40**, p. 2272, 2004.

[195] P. Vargas and D. Altbir, "Dipolar effects in multilayers with interface roughness," *Phys. Rev. B*, vol. **62**, p. 6337, 2000.

[196] S. Van Dijken and J. M. D. Coey, "Magnetoresistance sensor with an out-of-plane magnetized sensing layer," *Appl. Phys. Lett.*, vol. **87**, p. 022504, 2005.

Appendix A

Transmission lines theory

The key difference between circuit theory and transmission line theory is the electrical size. In circuit theory the dimensions of the electrical circuit (network) are much smaller that the electrical wavelength, while a transmission line may be a considerable fraction of the wavelength in size. This makes that voltages and currents will be a distributed parameter that can vary their magnitude and phase over the length of the circuit.

A transmission line is often schematically represented as a two-wire line, since transmission lines consist of two parallel conductors. A short segment Δz of the line can be modeled as a lumped element circuit, as shown Fig. A.1 , where R, L, G and C are the series resistance for both conductors, series inductance for both conductors, shunt conductances and shunt capacitance per unit of length respectively. L represents the total self-inductance of the two conductors, and the C is due to the close proximity of the two conductors. R appears due to the finite conductivity of the conductors, and G appears due to the dielectric loss in the material between the two conductors. The two parameters, R and G, represent loss.

Applying the Kirchoff voltage law and the Kirchoff current law and taking the

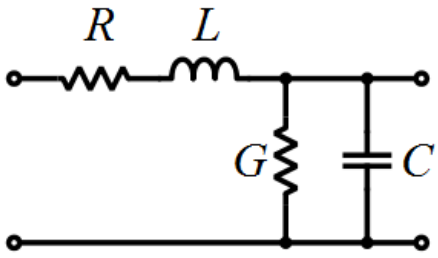

Figure A.1: Schematic representation of a transmission line.

limit $\Delta z \rightarrow 0$ one obtains the following differential equations for the voltage and current:

$$\frac{\partial v(z,t)}{\partial z} = -Ri(z,t) - L\frac{\partial i(z,t)}{\partial t} \quad , \tag{A.1}$$

$$\frac{\partial i(z,t)}{\partial z} = -Gv(z,t) - C\frac{\partial v(z,t)}{\partial t} \quad , \tag{A.2}$$

theses equations are the time domain form of the transmission lines,called telegrapher equations. For the sinusoidal steady-state condition, with cosine based phasors, these equations are simplified to

$$\frac{dV(z)}{dz} = -(R + j\omega L)I(z) \quad , \tag{A.3}$$

$$\frac{dI(z)}{dz} = -(G + j\omega C)V(z) \quad . \tag{A.4}$$

The solution to these differential equations leads to travelling voltage and current waves on the transmission line and can be written as:

$$\frac{d^2V}{dz^2} - \gamma^2 V(z) = 0 \quad , \tag{A.5}$$

$$\frac{d^2I}{dz^2} - \gamma^2 I(z) = 0 \quad , \tag{A.6}$$

where $\gamma = \alpha + j\beta = \sqrt{(R + j\omega L)G + j\omega C}$ is the complex propagation constant. The β parameter is the phase constant and α the attenuation constant. The solution to equation gives:

$$V(z) = V_0^+ \exp(-\gamma z) + V_0^- \exp(\gamma z) \quad , \tag{A.7}$$

$$I(z) = I_0^+ \exp(-\gamma z) + I_0^- \exp(\gamma z) \quad . \tag{A.8}$$

The first term on the right hand represents the wave propagation in the $+z$ direction and the second term represents the wave propagation in the $-z$ direction. Applying Eq. A.1 to the voltage Eq. A.7 gives the current on the line.

$$I(z) = \frac{\gamma}{R + j\omega L}\left(V_0^+ \exp(-\gamma z) - V_0^- \exp(\gamma z)\right) \quad ,$$

where the characteristic impedance Z_0 of the line is defined as:

$$Z_0 = \frac{R + j\omega L}{\gamma} = \sqrt{\frac{R + j\omega L}{G + j\omega C}} \quad . \tag{A.9}$$

Notice that Z_0 does not depend on the line length, only of the properties of the conductors and the dielectric material surrounding these conductors.

The wavelength of the travelling waves is defined as the distance between two successive points of equal phase on the wave at a fixed instant of time:

$$\lambda = \frac{2\pi}{\beta} \quad . \tag{A.10}$$

In the special case of a lossless transmission lines $R = G = 0$. Then $\beta = \omega\sqrt{LC}$ and $\alpha = 0$. The characteristic impedance reduces to

$$Z_0 = \sqrt{\frac{L}{C}} \quad . \tag{A.11}$$

The standard value for microwave components such as cables, connectors, etc., is 50 Ω.

The wavelength of the line is :

$$\lambda = \frac{2\pi}{\omega\sqrt{LC}} \quad . \tag{A.12}$$

In order to have a good control on the behavior of a high frequency circuit, is very important to realize transmission lines as uniform as possible along their length, so that the impedance behavior of the line does not vary and can be easily characterized. A change in transmission line properties, wanted (circuit elements) or unwanted (welding, matching connections), entails a change in the characteristic impedance, which causes a reflection Γ of the travelling wave, defined as.

$$\Gamma = \frac{V_0^-}{V_0^+} = \frac{Z_L - Z_0}{Z_L + Z_0} \quad , \tag{A.13}$$

where Z_L is the impedance in the point where the line is mismatched.

It is interesting emphasize that a perfect matching will not produce reflections on the line.

$\mathcal{S}$cattering $\mathcal{M}$atrix

When one works with a Vector Network Analyzer (VNA), one can obtain the real and the imaginary parts of the transmission and reflection parameters. The ports of the VNA are connects the microwave circuit. For a two port network one of the port is connected to the input and the other one to the output of the microwave circuit under study.

Let us define $V_n^{+(-)}$ the incident (+) voltage and the reflected voltage (-) on port n. The scattering matrix, for an 2-Port VNA is defined in relation to these incident and reflected voltage wave as:

$$\begin{pmatrix} V_1^- \\ V_2^- \end{pmatrix} = \begin{pmatrix} S_{11} & S_{12} \\ S_{21} & S_{22} \end{pmatrix} \begin{pmatrix} V_1^+ \\ V_2^+ \end{pmatrix} \quad , \tag{A.14}$$

where S parameters are defined as;

$$S_{ij} = \frac{V_i^-}{V_j^+} \tag{A.15}$$

Equation A.15 says that S_{ij} is found by driving port j with an incident wave of voltage V_j^+, and measuring the reflected wave amplitude V_i^- coming out of port i.

Appendix B

Fitting routines

The experimental ferromagnetic resonance curve is fitted to a theoretical model in order to obtain the frequency and the linewidth of the resonance.

This thesis uses two different theoretical model.

When the magnetic response U(f) of the sample is evaluated by using Kuanr method

$$U(f)_{Ku} = \frac{|S_{21-H}(f)|}{|S_{21-ref}(f)|} \ ,$$

being $|S_{21-H}(f)|$ the magnitude of S_{21} parameter for a fixed magnetic field H and $|S_{21-ref}(f)|$ the magnitude of S_{21} measured at the reference field, where the magnetic signal of the sample is out of the frequency range, the experimental data are fitted to the lorentzian curve

$$U(f) = U_0(f) + \frac{2A{\cdot}(\Delta f)}{4\pi\left(f - f_0\right)^2 + (\Delta f)^2}$$

where $U_0(f)$ is the offset of the signal, A is the area over the curve and f_0 and Δf are the frequency and the linewidth, defined as the full width at half maximum of the response, of the resonance. With $U_0(f) = 0$ and A=1 the model is based in a two fitting parameters; f_0 and Δf .

This method is used in the case of arrays of magnetic dots, where the magnetic signal is considerably less than in the case of magnetic tunnel junctions.

The second method is used when the magnetic signal of the sample is evaluated with Kalarickal method;

$$U(f)_{Ka} = \pm i\frac{\ln\left[S_{21-H}(f)/S_{21-ref}(f)\right]}{\ln\left[S_{21-ref}(f)\right]} \ ,$$

The fitting routine consists of dividing the magnetic signal into real and imagi-

nary part and fitting simultaneously both to the curves to;

$$\begin{aligned} \mathrm{Re}\,U(f) &= (1 + \mathrm{Re}[U_0(f)]) + \frac{A{\cdot}[f{\cdot}\Delta f{\cdot}\sin(\Theta) + (f_0^2 - f^2) + \cos(\Theta)]}{(f_0^2 - f^2)^2 + (f{\cdot}\Delta f)^2} \quad , \\ \mathrm{Im}\,U(f) &= (\mathrm{Im}[U_0(f)]) + \frac{A{\cdot}[-f{\cdot}\Delta f{\cdot}\cos(\Theta) + (f_0^2 - f^2) + \sin(\Theta)]}{(f_0^2 - f^2)^2 + (f{\cdot}\Delta f)^2} \quad . \end{aligned}$$

where $\mathrm{Re}[U_0(f)]$ and $\mathrm{Im}[U_0(f)]$ are the offsets of the real and imaginary parts respectively, A is the area and Θ is a phase angle. With $\mathrm{Re}[U_0(f)]$ =$\mathrm{Im}[U_0(f)] = 0$ and A=, 1, the model is based in a three fitting parameters; f_0, Δf and Θ.

Appendix C

The cryogenic system

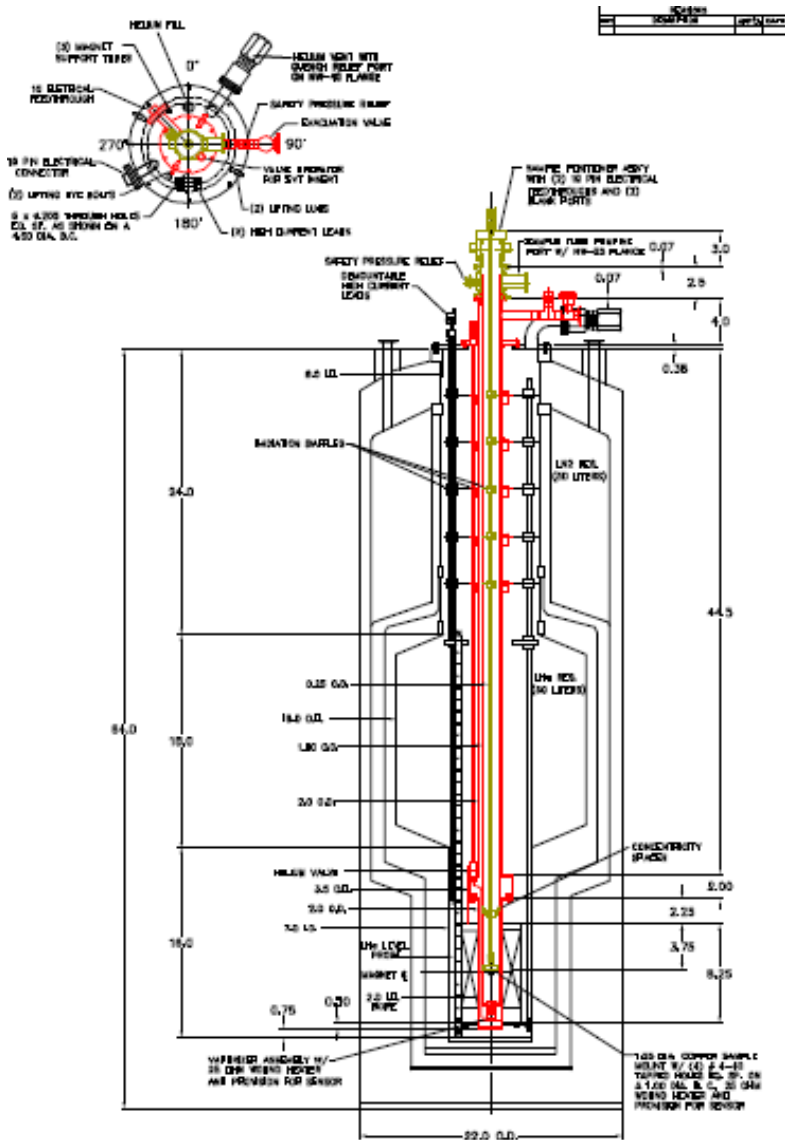

Figure C.1: A detailed scheme of the Janis cryostat used for the low temperatures measurements. All the distances are in inches.

Appendix D

Calibration curve of the commercial stick

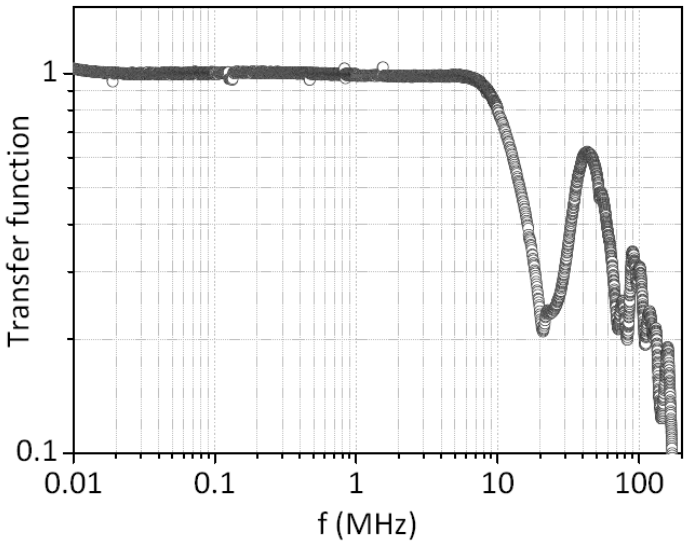

Figure D.1: Calibration curve of the cable in the commercial stick.